Title
Comprehensive Characterization of the Apoptotic Machinery in Glioblastoma Identifies New Therapeutic Strategies

Author
Mai, Wilson Xuan

Publication Date
2018

Peer reviewed|Thesis/dissertation

UNIVERSITY OF CALIFORNIA

Los Angeles

Comprehensive Characterization of the Apoptotic Machinery in Glioblastoma Identifies New Therapeutic Strategies

A dissertation submitted in partial satisfaction of the

requirements for the degree Doctor of Philosophy

in Molecular and Medical Pharmacology

by

Wilson Xuan Mai

2018

ABSTRACT OF THE DISSERTATION

Comprehensive Characterization of the Apoptotic Machinery in Glioblastoma Identifies New Therapeutic Strategies

by

Wilson Xuan Mai
Doctor of Philosophy in Molecular and Medical Pharmacology
University of California, Los Angeles, 2018
Professor David A Nathanson, Chair

Effective treatments for cancer require the engagement of the apoptotic (cell death) machinery. These pathways have been implicated in the therapeutic efficacy of almost every chemotherapy, targeted agent, and even in some forms of immunotherapy. Inability to sufficiently engage the apoptotic machinery results in tumor survival and resistance. Glioblastoma (GBM), the deadliest form of brain cancer, has poor clinical response to almost every therapy, suggesting a heightened anti-apoptotic signature. In these studies, we are the first to comprehensively characterize the apoptotic machinery in patient-derived GBM samples through genetic, molecular, and functional measures. In the first portion of this work, we demonstrate how GBM are capable of utilizing multiple apoptotic blocks and how this versatility endows them with intrinsic resistance to standard of care. By understanding the intricacies in GBM apoptotic machinery, we are able to rationally design therapeutic strategies to exploit these dependencies, as highlighted by the second portion of this work.

The dissertation of Wilson Xuan Mai is approved.

Steven J Bensinger

Thomas G Graeber

Michael Alan Teitell

David A Nathanson, Committee Chair

University of California, Los Angeles

2018

DEDICATION

This is dedicated to my family and friends who have supported me through all the difficult times.

This is especially dedicated to my mother who has shown me what perseverance truly is.

TABLE OF CONTENTS

ACKNOWLEDGEMENTS

I would like to thank my mentor Dr. David Nathanson for his patience, support, and guidance over the past years. I am very grateful for the opportunities that I have been provided with and feel confident as I move towards the future. Moreso, I am thankful for all the memories I have made in these years in the lab.

I would like to thank my committee members Dr. Steven Bensinger, Dr. Thomas Graeber, and Dr. Michael Teitell for all their support and guidance throughout graduate school.

I would like to acknowledge and thank those who have helped me on my past and current work. This includes Christopher Tsang (UCLA), Lynn Baufeld (UCLA), Danielle Morrow (UCLA), Laura Gosa (UCLA), Dr. Veerle W. Daniels (Harvard), Lisa Ta (UCLA), Jonathan E. Tsang (UCLA), Brian Higgins (Roche), W. Blake Gilmore (UCLA), Nicholas A. Bayley (UCLA), Mitra Dehghan Harati (UCLA), Dr. Jason T. Lee (UCLA), Dr. William H. Yong (UCLA), Dr. Harley I. Kornblum (UCLA), Dr. Paul S. Mischel (UCLA), Dr. P. Nagesh Rao (UCLA), Dr. Peter M. Clark (UCLA), Dr. Timothy F. Cloughesy (UCLA), Dr. Anthony Letai (Harvard), Larry Pang (UCLA), Liu Wei (UCLA). Research is such a collaborative effort and all of this has been capable because of the help I have received.

I would like to acknowledge my past mentors Dr. Huan Meng and Dr. Andre Nel for guiding me in my early stages of research. I would not be here today had it not been for those critical years of learning.

Chapter 2 is a version of Mai W.X., Gosa L., Daniels V.W., Ta L., Tsang J.E., Higgins B., Gilmore W.B., Bayley N.A., Harati M.D., Lee J.T., Yong W.H., Kornblum H.I., Bensinger S.J., Mischel P.S., Rao P.N., Clark P.M., Cloughesy T.F., Letai A., Nathanson D.A. Cytoplasmic p53 couples oncogene-driven glucose metabolism to apoptosis and is a therapeutic target in glioblastoma. *Nature Medicine.* 2017 Nov;23(11):1342-1351. doi: 10.1038/nm.4418. Epub 2017 Oct 9. PMID: 29035366

My research was supported by the National Science Foundation (NSF) Graduate Research Fellowship (GRPF) DGE-114087 and UCLA Dissertation Year Fellowship (DYF).

VITA

EDUCATION

B.S. **2009-2013**	University of California Los Angeles Major: Biochemistry Departmental Honors

AWARDS AND HONORS

2017-2018	Dissertation Year Fellowship (DYF)
2013-2017	National Research Foundation (NSF) Graduate Research Fellowship Program (GRFP)
2013-2016	Dean's Graduate Research Scholarship
2012	LAU Research Scholarship
2010-2011	UCLA Academic Competitiveness Grant

PUBLICATIONS

[1] **W.X. Mai** et. al. *Cytoplasmic p53 couples oncogene-driven metabolism to apoptosis and is a therapeutic target in glioblastoma*. Nature Medicine. October 2017.

[2] P.M. Clark, **W.X. Mai**, T.F. Cloughesy, D.A. Nathanson. *Emerging Approaches for Targeting Metabolic Vulnerabilities in Malignant Glioma.* Curr. Neurol. Neurosci. Rep. February 2016.

[3] Y.S Shin, J. Kim, D. Johnson, A.A. Dooraghi, **W.X. Mai**, L. Ta, A.F. Chatziioannou, M.E. Phelps, D.A. Nathanson, and J.R. Heath. *Quantitative assessments of glycolysis from single cells.* Technology (Singap World Sci.). June 2015.

[4] M. Xue, W. Wei, Y. Su, Y.S. Shin, **W.X. Mai**, D.A. Nathanson, and J.R. Heath. *Chemical methods for the simultaneous quantitation of metabolites and proteins from single cells.* J. Am. Chem. Soc. April 2015.

[5] H. Meng, Y. Zhao, J. Dong, M. Xue, Y.S. Lin, Z. Ji, **W.X. Mai**, H. Zhang, C.H. Chang, C.J. Brinker, J.I. Zink, A.E. Nel. *Two-wave nanotherapy to target the stroma and optimize gemcitabine delivery to a human pancreatic cancer model in mice.* ACS Nano. November 2013.

[6] H. Meng and **W.X. Mai** et. al., *Co-delivery of Optimal Drug/siRNA Combination Using Mesoporous Silica Nanoparticle to Overcome Drug Resistance in Breast Cancer in vitro and in vivo*. ACS Nano. February 2013.

[7] **W.X. Mai**, T. Xia, and H. Meng. *Development of Pharmaceutically Adapted Mesoporous Silica Nanoparticles for siRNA Delivery*. Advanced Delivery and Therapeutic Applications of RNAi, John Wiley & Sons, Inc. December 2012.

[8] **W.X. Mai** and H. Meng. *Mesoporous Silica Nanoparticles: A Multifunctional System*, Integrative Biology. October 2012.

CHAPTER 1:

Defining the Apoptotic Machinery in GBM and Overcoming Barriers to Standard of Care

INTRODUCTION

Resistance to mitochondria programmed cell death, or intrinsic apoptosis, is one of the key hallmarks of cancer[1]. Cancers have been shown to enhance their apoptotic block(s) by increasing the expression of anti-apoptotic proteins, namely the BCL-2 family (Bcl-2, Bcl-xL, Mcl-1), whose function is to bind and sequester pro-apoptotic BH3-only proteins (Bim, Puma, Bid) and effector proteins (Bax, Bak) to prevent cell death[2]. As a result, cancer cells can become dependent on a specific BCL-2 family member(s) for survival. Inability to inhibit these apoptotic blocks in cancers often results in tumor survival and resistance.

Although many studies in the past decade have unveiled the importance of the Bcl-2 family proteins in cancer survival, the apoptotic machinery in glioblastoma (GBM), the deadliest form of brain cancer, remains poorly understood. GBM tumors have displayed poor clinical response to almost every therapy, suggesting a refractory apoptotic state. In addition, adult brain tissue has been shown to be resistant to apoptosis compared to most organ systems in the human body, suggesting a potentially inherited trait in GBM tumors that promote intrinsic resistance to therapeutic agents[3].

As such, we reasoned that understanding which apoptotic block(s) GBM utilized would provide insight into underlying resistant mechanisms against current therapies and thereby uncover new therapeutic strategies. Towards this end, we have comprehensively characterized the apoptotic blocks in a panel of patient-derived GBM samples. Our results indicate that GBM are capable of deploying multiple anti-apoptotic proteins (Bcl-xL and Mcl-1) and that standard of care (irradiation and temozolomide) fails to neutralize both blocks. However, sufficient inhibition of these blocks induces significant cell death in GBM cells regardless of genetic background, representing a potential approach to combat heterogeneous GBM tumors.

RESULTS

Identification of apoptotic blocks in GBM

Resistance to therapy in GBM has largely been attributed to inadequate drug accumulation within the tumor due to poor brain penetration of drugs[4]. However, GBM cells exposed to drugs in culture, where physiological barriers of the brain are not present, also displayed high levels of intrinsic resistance to a number of clinically approved drugs, suggesting potentially other modes of drug resistance (**Supplementary Fig. 1a, b**)[5]. Studies have demonstrated that the anti-apoptotic Bcl-2 family proteins can prevent cell death following cellular insult[1,2]. To thoroughly understand the apoptotic network used in GBM, BH3 profiling was carried out in a panel of patient-derived GBM cells (**Fig. 1a**). In BH3 profiling, cells are exposed to BH3 peptides and/or mimetics that are capable of sequestering specific anti-apoptotic Bcl-2 protein counterparts. Changes in mitochondrial potential, as measured by cytochrome *c* release, is then quantified as an indicator of apoptotic initiation. By gauging the mitochondrial response to a panel of BH3 peptides/mimetics, we can delineate the specific apoptotic block(s) used by GBM.

Positive control cell lines with established single dependencies - RI-1, MDA-MB-231, and H929 - all displayed significant cytochrome *c* release following exposure to single inhibitors ABT-199 (targets Bcl-2), HRK (targets Bcl-xL), and MS1 (targets Mcl-1), respectively (**Fig. 1a**)[6,7,8]. However, the majority of GBM cells tested had minimal mitochondrial response following exposure to individual peptide (**Fig. 1a**). Instead, most GBM samples required both HRK and MS1 in order to achieve significant levels of cytochrome *c* release, suggesting that GBM rarely rely on a single anti-apoptotic protein and that they depend on both Bcl-xL and Mcl-1 for survival (**Fig. 1a**). Notably, there was minimal mitochondrial response following exposure to BAD peptide, which inhibits both Bcl-2 and Bcl-xL, highlighting a strong and specific dependency on Bcl-xL and Mcl-1 (**Fig. 1a**). In support of this, genetic knockdown of Bcl-xL or Mcl-1 in GS025, a line displaying both Bcl-xL and Mcl-1 dependencies, resulted in a mitochondrial response following exposure to

single peptide MS1 or HRK, respectively (**Fig. 1b and Supplementary Fig. 2a**). Furthermore, gene expression analysis revealed that GBM tumors have heightened Bcl-xL and Mcl-1 expression but not Bcl-2, when compared to normal brain tissue, further supporting the notion that GBM specifically utilize both Bcl-xL and Mcl-1 for survival (**Supplementary Fig. 2b**).

To verify that Bcl-xL and Mcl-1 is indeed necessary for GBM survival, we treated the panel of patient-derived GBM cells with various combinations and concentrations of Bcl-2, Bcl-xL, and Mcl-1 chemical inhibitors (ABT-199, A-1155463, and S63845, respectively) and measured their therapeutic effect (**Fig. 1c and Supplementary Fig. 2c**). Synthetic lethality was most striking with the combination of Bcl-xL + Mcl-1 inhibition, whereas minimal enhanced efficacy were observed with Bcl-2 + Bcl-xL inhibition, and Bcl-2 + Mcl-1 inhibition (**Fig. 1c**)[9]. Levels of apoptosis, as measured by annexin V staining, corroborated this synergistic cell killing effect across multiple GBM cells (**Fig. 1d**). Furthermore, genetic knockdown of Bcl-xL in GS025 resulted in enhanced apoptosis in cells treated with a Mcl-1 inhibitor, and genetic knockdown of Mcl-1 resulted in enhanced apoptosis in cells treated with a Bcl-xL inhibitor (**Supplementary Fig. 2d, e**). Altogether, these data suggest that GBM cells specifically utilize Bcl-xL and Mcl-1 for survival, and that neutralization of these blocks results in significant levels of apoptosis.

It is worth noting that the levels of synergy with Bcl-xL and Mcl-1 inhibitors were heterogeneous, ranging from single Mcl-1 dependency (e.g. GS116 and GS028) and low sensitivity to all combinations (e.g. GS024 and GS102) (**Fig. 1a, c**). To this point, BH3 profiling with universal activators BIM and BID revealed that GBM cells have varying “primed” states (**Supplementary Fig. 3a**). In terms of apoptotic induction, lowly primed cells have a higher apoptotic threshold and require higher levels of pro-apoptotic activators (BIM and BID) to achieve a mitochondrial response, whereas the highly primed cells rapidly release cytochrome *c* following exposure to these peptides. Past studies have suggested these primed states are predictive of drug

response[10]. Concordantly, the basal primed state of the GBM cells correlated with the synergy to Bcl-xL + Mcl-1 inhibition, with the lowly primed cells having minimal response to the combination of inhibitors (**Supplementary Fig. 3b**). These results support that although the majority of GBM depend on Bcl-xL and Mcl-1 for survival, inhibition of these blocks may not fully induce apoptosis in cells which are lowly primed, and thus, have abnormally high apoptotic thresholds.

Irradiation and temozolomide induce minimal apoptosis

We next investigated whether or not the usage of two anti-apoptotic proteins (Bcl-xL and Mcl-1) promotes apoptotic resistance to standard of care, irradiation (IR) and alkylating agent, temozolomide (TMZ). GS025 cells treated with IR and TMZ displayed enhanced levels of pH2A.X staining compared to untreated cells, indicating induction of DNA damage (**Supplementary Fig. 4a**). Accordingly, both IR and TMZ resulted in growth inhibition (**Supplementary Fig. 4b**). However, despite having growth inhibitory effects, IR and TMZ resulted in minimal apoptosis (**Supplementary Fig. 4c**). Altogether, these data suggest that IR and TMZ may inhibit tumor growth, but have minimal cell killing effects.

Enhancing the apoptotic effects of IR/TMZ

To investigate the roles of Bcl-xL and Mcl-1 in apoptotic resistance to IR and TMZ, we examined molecular alterations in the Bcl-2 family proteins following treatment. BH3 profiling revealed enhanced mitochondrial response to single HRK peptide exposure following IR or TMZ treatment in GS025, a GBM sample dependent on both Bcl-xL and Mcl-1 (**Fig. 2a**). Enhanced inhibitory effects were observed when combining TMZ + Bcl-xL inhibitor, as compared to TMZ + Bcl-2 inhibitor or TMZ + Mcl-1 inhibitor (**Fig. 2b**). Consequently, cells treated with IR or TMZ displayed drastic apoptosis in response to pharmacological and genetic inhibition of Bcl-xL, as opposed to Bcl-2 or Mcl-1 inhibition (**Fig. 2c, d**). Altogether, these data suggest that IR inhibits Mcl-1, resulting

in a single and specific dependency on Bcl-xL. Moreover, by removing Bcl-xL, the cells readily undergo apoptosis.

Alterations in dependencies can occur in a multitude of ways. Following cellular insult, tumor cells can upregulate the expression of specific BH3-only proteins to sequester anti-apoptotic Bcl-2 proteins, decrease the expression of anti-apoptotic proteins, as well as increase the expression of compensatory anti-apoptotic proteins[11-13]. To determine how IR and TMZ switches a dually dependent GBM to being solely dependent on Bcl-xL, we first measured changes in Bcl-2 family protein expression and interactions. Immunoblots revealed no significant changes in Bcl-xL or Mcl-1 expression following IR or TMZ treatment (**Supplementary Fig. 5a**). Notably, the expression of Puma, a BH3-only pro-apoptotic protein, was significantly increased in response to IR or TMZ (**Supplementary Fig. 5a**). BH3-only proteins can bind and sequester their anti-apoptotic counterpart. Since our results indicate that IR and TMZ removes the Mcl-1 block, resulting in a dependency on Bcl-xL, we posited that this upregulation of Puma may have a role.

Indeed, genetic knockdown of Puma abrogated the mitochondrial response to HRK following IR and TMZ treatment (**Fig. 3a**). Furthermore, the enhanced efficacy of TMZ + Bcl-xL inhibition in the panel of patient-dervied GBM cells correlated strongly with increased Puma expression following TMZ exposure (**Fig. 3b**). When looking at apoptosis, as measured by annexin V staining, knockdown of PUMA diminished the synergistic cell killing effect of IR/TMZ + Bcl-xL inhibition (**Fig. 3c, d**). Lastly, immunoprecipitation of Mcl-1 revealed heightened interactions between Mcl-1 and Puma following IR or TMZ treatment, suggesting that the enhanced levels of Puma following IR or TMZ treatment promotes Mcl-1 sequestration (**Fig. 3e**). It is important to note that p53 mutational status also played an important role in the sensitizing effects of TMZ. p53 is a known regulator of Puma (p53 upregulated modulator of apoptosis). As such, we observed minimal increase in Puma levels in p53 mutant GBM compared to p53 wild-type cells following TMZ

treatment (**Supplementary Fig. 5b**). Therefore, p53 mutant lines displayed significantly lower enhanced sensitivity to the TMZ + Bcl-xL inhibitor combination (**Supplementary Fig. 5c**). Altogether, these data support that IR and TMZ enhances Puma protein levels, which then binds to and sequesters Mcl-1, thereby creating a single dependency on Bcl-xL for survival.

MGMT contributes to heterogeneous response to TMZ + Bcl-xL inhibition

Although TMZ is capable of sensitizing GBM cells to Bcl-xL inhibition, we observed a heterogeneous response to the combination (**Fig. 2b**). To understand the differences in sensitivity, we investigated the role of O-6-Methylguanine-DNA methyltransferase (MGMT), a DNA repair protein known to counter the effects of TMZ[14]. Approximately 30-40% of GBM patients have methylated MGMT promoters which confers improved responses to TMZ. When separating groups based on methylation status (methylated and unmethylated), as determined by PCR, we observed no significant difference in induced DNA damage or sensitivity to TMZ + Bcl-xL inhibition (**Fig. 4a and Supplementary Fig. 6a, b**). Although MGMT methylation status is often used as a predictive biomarker for response to TMZ in the clinic, studies have suggested PCR mechanisms may have limitations in regards to determining MGMT activity[15]. Similarly, we observed no significant difference in MGMT protein expression between methylated and unmethylated GBM cells (**Fig. 4b**). In contrast to PCR-defined methylation status, we found a strong correlation between MGMT protein expression and sensitivity to TMZ + Bcl-xL inhibition (**Fig. 4c**).

To validate the role of MGMT, we hypothesized that depletion of MGMT in an unmethylated GBM cell with high MGMT expression (GS081) should sensitize it to TMZ + Bcl-xL inhibition. To this end, we utilized O6-Benzylguanine (O6BG), a chemical inhibitor of MGMT designed to improve GBM response to standard of care[16,17]. Treatment with O6BG significantly reduced MGMT protein levels in GS081 (**Fig. 4d**). Strikingly, GS081, which displayed minimal response following TMZ + Bcl-xL inhibition, showed enhanced apoptotic induction following the combination treatment when

pre-treated with O6BG (**Fig. 4e**). Supportingly, genetic knockdown of MGMT also ameliorated the enhanced cell killing effects of TMZ + Bcl-xL inhibition in GS081 (**Fig. 4f, g**). Collectively, these results suggest that MGMT expression can limit the sensitizing effects of TMZ, and that inhibition of MGMT can enhance apoptosis in response to TMZ and Bcl-xL inhibition. Notably, methylation status as determined by PCR was insufficient in determining MGMT expression and thus sensitivity to the combination, indicating that a more sophisticated means of determining MGMT activity may be needed to stratify patients to this combination.

DISCUSSION

Here we discovered that the majority of GBM cells utilize both Bcl-xL and Mcl-1 for survival and that sufficient inhibition of both apoptotic blocks is required for initiation of the apoptotic cascade. However, mechanistic studies revealed that both standard of care treatments (IR and TMZ) only neutralize Mcl-1, allowing the cells to resist apoptosis through Bcl-xL. Although the clinical combination of TMZ to IR enhanced overall survival in patients by approximately 2.5 months, these results suggest that the combination of DNA damaging agents may not be the most efficacious strategy for achieving tumor reduction[18]. Notably, removal of the Bcl-xL block following IR or TMZ treatment resulted in significant cell death, suggesting that this new combinatorial approach may enhance current standard of care treatments for GBM patients.

The advancement of Bcl-2 family small molecule inhibitors has been revolutionary for hematological malignancies[19,20]. The combination of Venetoclax, a Bcl-2 antagonist, with other agents has resulted in astonishing levels of remissions. However, a potential limitation in translating these new agents into GBM is the lack of brain-penetrance due to the blood-brain barrier, a common challenge in GBM treatment. Future studies are required to determine if these new class of drugs are capable of accumulating in GBM tumors at a concentration sufficient to neutralize the desired block(s).

Targeting multiple anti-apoptotic proteins has also been hindered due to dose-limiting toxicities, with the most common side effect being thrombocytopenia[21]. However, the development of more specific BH3 mimetics that have high affinity to specific Bcl-2 anti-apoptotic proteins in addition to improved dosing schedules has resulted in tolerable treatment regimens that show great promise in clinical trials[19,22,23].

Another alternative to these issues include exploiting oncogenic signaling that drive dependencies on these particular Bcl-2 proteins. In the following study, we will demonstrate how oncogenic signaling intertwines with anti-apoptotic dependencies[11,24]. By understanding this molecular framework, we are able to exploit the specific apoptotic blocks using established, brain-penetrant targeted agents. This approach potentially minimizes toxicity as well as improves pharmacological activity within the tumor.

Lastly, it is worth noting that oncogenic signaling not only maintains high expression of anti-apoptotic proteins, but it also reduces the levels of pro-apoptotic BH3-only proteins capable of sequestering apoptotic blocks[11,12,25]. The predominant mechanism of targeting the apoptotic pathway is currently through inhibition of the anti-apoptotic Bcl-2 family proteins. However, several studies have shown that inhibition of these pathways can be achieved through other means. For example, Bim has been shown to be able to universally bind to all anti-apoptotic Bcl-2 family proteins, therefore its upregulation can act as a universal inhibitor of Bcl-2, Bcl-xL, and Mcl-1[2,25]. More specifically, the BH3-only protein, Noxa, is a known antagonist of Mcl-1[12,26]. Therefore, agents enhancing Noxa may be effective in tumors dependent on Mcl-1. Similarly, p53 has also been shown to be capable of binding to Bcl-xL, suggesting a potential therapeutic avenue for Bcl-xL inhibition[24,27]. As the apoptotic field continues to advance, it is imperative to consider

mechanisms of enhancing specific pro-apoptotic proteins in addition to the prevailing strategy of directly inhibiting anti-apoptotic proteins.

ONLINE METHODS

Patient-derived GBM cells. All patient tissue to derive GBM cell cultures was obtained through explicit informed consent, using the UCLA Institutional Review Board (IRB) protocol: 10-000655. Primary GBM cells were established and maintained in gliomasphere conditions consisting of DMEM/F12 (Gibco), B27 (Invitrogen), Penicillin-Streptomycin (Invitrogen), and Glutamax (Invitrogen) supplemented with Heparin (5 μg/mL, Sigma), EGF (50 ng/mL, Sigma), and FGF (20 ng/mL, Sigma). MDA-MB-231 was a kind gift from the Pajonk lab and was cultured in DMEM (Gibco), 10% FBS (Gemini), Penicillin-Streptomycin (Invitrogen), and Glutamax (Invitrogen). H929 (ATCC) and RI-1 (DSMZ) were cultured in RPMI-1640, 10% FBS (Gemini), Penicillin-Streptomycin (Invitrogen), and Glutamax (Invitrogen). All cells were grown at 37°C, 20% O_2, and 5% CO_2 and were routinely monitored and tested negative for the presence of mycoplasma using a commercially available kit (MycoAlert, Lonza). All cells were authenticated by short-tandem repeat (STR) analysis.

Reagents and antibodies. Chemical inhibitors from the following sources were dissolved in DMSO for *in vitro* studies: ABT-199 (APExBIO), A-1155463 (APExBIO), S63845 (APExBIO), Temozolomide (Selleck Chemicals), and O6-Benzylguanine (Selleck Chemicals). Antibodies used for immunoblotting were obtained from the listed sources: β-actin (8H10D10) Mouse mAb (Cell signaling, 3700), BIM (C34C5) Rabbit mAb (Cell Signaling, 2933), PUMA (D30C10) Rabbit mAb (Cell Signaling, 12450), Bcl-2 (50E3) Rabbit mAb (Cell Signaling, 2870), Bcl-xL (54H6) Rabbit mAb (Cell Signaling, 2764), Mcl-1 (D35A5) Rabbit mAb (Cell Signaling, 5453), Mcl-1 Mouse (BD Pharmagen, 559027), and PUMA (G-3) mAb (Santa Cruz Biotech., sc-374223). Antibodies used for immunoprecipitation were obtained from the listed sources: Mcl-1 (D2W9E) Rabbit mAb (Cell Signaling, 94296). Secondary antibodies were obtained from the listed sources: Anti-rabbit IgG HRP-linked (Cell Signaling, 7074) and Anti-mouse IgG HRP-linked (Cell Signaling, 7076). All immunoblotting antibodies were used at a dilution of 1:1000, except β-actin and tubulin,

which were used at 1:10,000. Immunoprecipitation antibodies were diluted according to manufacturer's instructions (1:100 for Mcl-1). Secondary antibodies were used at a dilution of 1:5000. p.H2AX antibody was obtained from Biolegend (613408).

Annexin V apoptosis assay. Cells were collected and analyzed for Annexin V and PI staining according to manufacturer's protocol (BD Biosciences). Briefly, cells were plated at 5 x 10^4 cells/ml and treated with appropriate drugs. Following indicated time points, cells were collected, trypsinized, washed with PBS, and stained with Annexin V and PI for 15 minutes. Samples were then analyzed using the BD LSRII flow cytometer.

Immunoblotting. Cells were collected and lysed in RIPA buffer (Boston BioProducts) containing Halt Protease and Phosphatase Inhibitor (Thermo Fischer Scientific). Lysates were centrifuged at 14,000xg for 15min at 4°C. Protein samples were then boiled in NuPAGE LDS Sample Buffer (Invitrogen) and NuPAGE Sample Reducing Agent (Invitrogen) and separated using SDS-PAGE on 12% Bis-Tris gels (Invitrogen) and transferred to nitrocellulose membrane (GE Healthcare). Immunoblotting was performed per antibody's manufacturer's specifications and as mentioned previously. Membranes were developed using the SuperSignal system (Thermo Fischer Scientific).

Immunoprecipitation. Cells were collected, washed once with PBS, and incubated in IP lysis buffer (25 mM Tris-HCL pH 7.4, 150 mM NaCl, 1 mM EDTA, 1% NP-40, 5% Glycerol) at 4°C for 15 minutes. 300-500 µg of each sample was then pre-cleared in Protein A/G Plus Agarose Beads (Thermo Fischer Scientific) for one hour. Following pre-clear, samples were then incubated with antibody-bead conjugates overnight according to manufacturer's specifications and as mentioned previously. The samples were then centrifuged at 1000g for 1 min, and the beads were washed with 500 µL of IP lysis buffer for five times. Proteins were eluted from the beads by boiling in 2x

LDS Sample Buffer (Invitrogen) at 95°C for 5 min. Samples analyzed by immunoblotting as previously described. Immunoprecipitation antibodies were diluted according to manufacturer's instructions (1:100 for Mcl-1).

Dynamic BH3 profiling. GBM gliomaspheres were first disassociated to single-cell suspensions with TrypLE (Gibco) and resuspended in MEB buffer (150 mM Mannitol 10 mM HEPES-KOH, 50 mM KCl, 0.02 mM EGTA, 0.02 mM EDTA, 0.1 % BSA, 5 mM Succinate). 50µl of cell suspension (3×10^4 cells/well) were plated in wells holding 50 µL MEB buffer containing 0.002% digitonin and indicated peptides in 96-well plates. Plates were then incubated at 25°C for 50 min. Cells were then fixed with 4% paraformaldehyde for 10min, followed by neutralization with N2 buffer (1.7M Tris, 1.25M Glycine pH 9.1) for 5min. Samples were stained overnight with 20 µL of staining solution (10% BSA, 2% Tween 20 in PBS) containing DAPI and anti-cytochrome *c* (BioLegend). The following day, cytochrome *c* release was quantified using BD LSRII flow cytometer. Measurements were normalized to appropriate controls that do not promote cytochrome *c* release (DMSO and inactive PUMA2A peptide). Delta priming refers to the difference in amount of cytochrome *c* release between vehicle treated cells and drug treated cells. Fold change in regards to BIM refers to the fold difference in cytochrome *c* release following exposure to indicated peptides and to that of 3 µM BIM peptide.

MGMT methylation analysis.

To generate bisulfite modified DNA, genomic DNA isolated from cells was modified using the EZ DNA Methylation-Gold Kit (ZymoResearch, Orange,CA) following the manufacturer's protocol. Samples were subjected to a two-stage nested PCR strategy using: first-stage primers (5′-GGATATGTTGGGATAGTT-3′ and 5′-CCAAAAACCCCAAACCC-3′) and second-stage primers (unmethylated reaction: 5′-TTTGTGTTTTGATGTTTGTA-GGTTTTTGT-3′ and 5′-AACTCCACACTCTTCCAAAAACAAAACA-3′; methylated reaction: 5′-

TTTCGACGTTCGTAGGTTTTCGC-3' and 5′-GCACTCTTCCGAAAACGAA-ACG-3′). PCR products were analyzed on 3% agarose gels. Positive and negative control samples for the MSP reaction were U87MG DNA treated with SssI methyltransferase (New England Biolabs, Ipswich, MA) and whole-genome amplification ofU87MGDNAusing the GenomiPhi V2 Amplification Kit (Amersham Biosciences, Piscataway, NJ), respectively.

Genetic manipulation. In general, lentivirus used for genetic manipulation were produced by transfecting 293-FT cells (Thermo) using Lipofectamine 2000 (Invitrogen). Virus was collected 48 hours after transfection. Bcl-xL (TRCN0000033499 and TRCN0000033500), Mcl-1 (TRCN0000005514), and Puma (TRCN0000033612) knockdown constructs were all obtained from Sigma.

Protein quantification. Protein quantification was done on the LI-COR Odyssey FC and Image Studio Lite software. All proteins measured are normalized to their respective actin loading control.

Synergy score calculations. GBM cells were plated in triplicate and treated with Bcl2i, BclxLi, Mcl1i, or combination at multiple concentrations using a matrix where each drug was added to the cells at six concentrations (0-1000 nM). Cellular viability was measured, via Cell Titer Glo (Promega) following 48 hours of treatment. Using the Chalice software, as described in Lehar et al., the response of the combination was compared to its single agents, and the combinatorial effects were calculated using the synergy score[9].

Gene expression analysis. RNA expression was analyzed using the Illumina HiSeq 2500 platform. Raw data were processed with the TOIL RNA-Seq pipeline. Briefly, RNA-Seq reads were aligned using STAR and quantified with RSEM software packages. Gene expression data

for normal brain samples processed through the TOIL pipeline were obtained from UCSC XenaBrowser. Upper-quartile normalized gene expression data were log2 transformed prior to downstream analysis.

Statistical analysis. Comparisons were made using two-tailed unpaired Student's *t*-tests and *p* values <0.05 were considered statistically significant. All data from multiple independent experiments were assumed to be of normal variance. For each experiment, replicates are as noted in the figure legends. Data represent mean ± s.e.m. values unless otherwise indicated. All statistical analyses were calculated using Prism 7.0 (GraphPad).

Chapter 1 - Figure 1

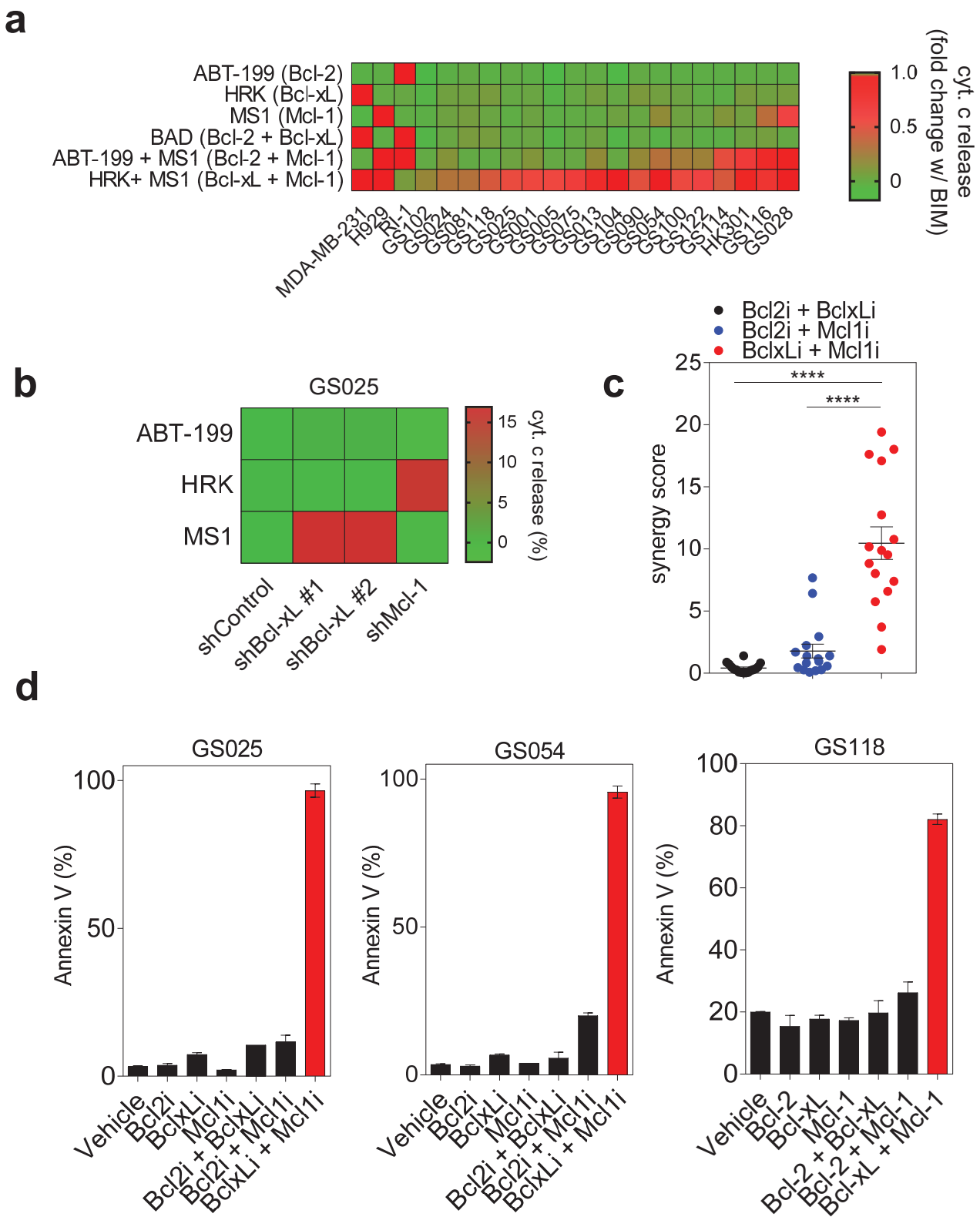

FIGURE LEGENDS

Figure 1. GBM depend on Bcl-xL and Mcl-1 for survival. (a) BH3 profiling in 18 patient-derived GBM cells and 3 positive control cell lines (MDA-MB-231, H929, and Ri-1). Data is shown as fold change in cytochrome *c* release (relative to BIM peptide response) following exposure to indicated BH3 peptides or mimetics. ABT-199 targets Bcl-2, HRK targets Bcl-xL, MS1 targets Mcl-1, and BAD targets both Bcl-2 and Bcl-xL. **(b)** Cytochrome *c* release (%) following BH3 profiling with indicated BH3 peptides or mimetics in GS025 shControl, shBcl-xL #1, shBcl-xL #2, and shMcl-1. **(c)** Dose-titration of ABT-199 (Bcl-2 inhibitor; Bcl2i), A-1155463 (Bcl-xL inhibitor, BclxLi), and S63845 (Mcl-1 inhibitor, Mcl1i) was conducted across all GBM cells and the synergy score was calculated. See **Supplementary Fig. 2c** and **Materials and Methods** for more information. **(d)** Annexin V staining of GS025, GS054, and GS118 following treatment with indicated Bcl-2 family chemical inhibitors for 48 hours. For BH3-profiling, the concentrations of ABT-199, HRK, MS1, and BAD used are 1 μM, 100 μM, 1 μM, and 10 μM, respectively. For annexin V measurements, concentration of Bcl2i, BclxLi, and Mcl1i were all 1 μM. Comparisons were made using two-tailed unpaired Student's *t*-test. ***p<0.001, ****p<0.0001.

Chapter 1 - Figure 2

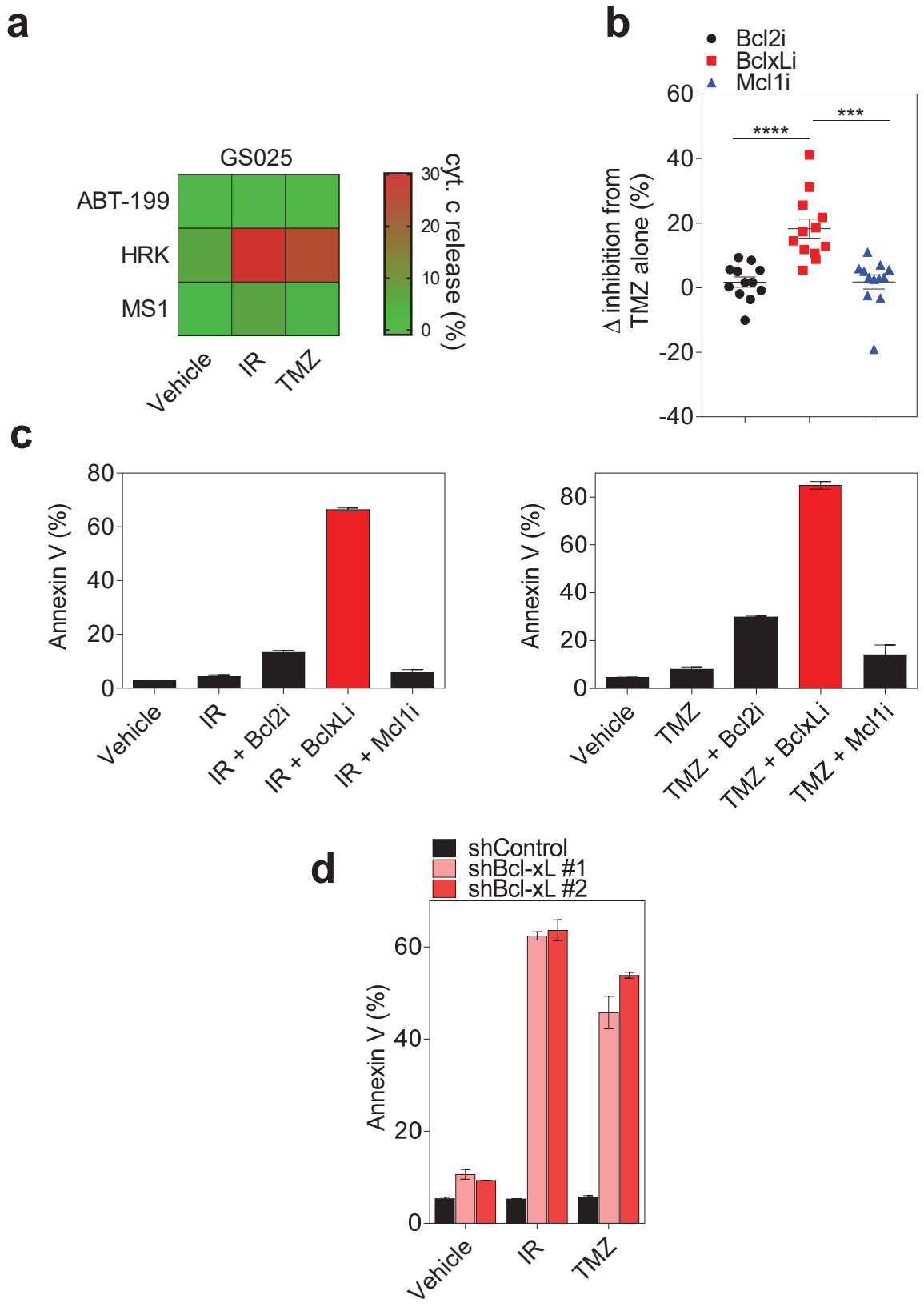

Figure 2. IR and TMZ inhibit Mcl-1 and create a dependency on Bcl-xL. (a) Cytochrome *c* release (%) following BH3 profiling with indicated peptides or mimetics in GS025 cells treated with IR or TMZ for 48 hours. **(b)** Difference in therapeutic efficacy of TMZ +/- Bcl2i, BclxLi or Mcl1i across a panel of patient-derived GBM cells. % viability is assessed by Cell Titer Glo and compared to TMZ treatment alone. **(c)** Annexin V staining of GS025 following indicated treatments for 72 hours. **(d)** Same as **(c)** but in GS025 shControl, shBcl-xL #1, and shBcl-xL #2. Dose of IR was 20 gy. Concentration of TMZ was 300 μM. Concentration of Bcl2i, BclxLi, and Mcl1i were all 1 μM. Comparisons were made using two-tailed unpaired Student's *t*-test. ***p<0.001, ****p<0.0001.

Chapter 1 - Figure 3

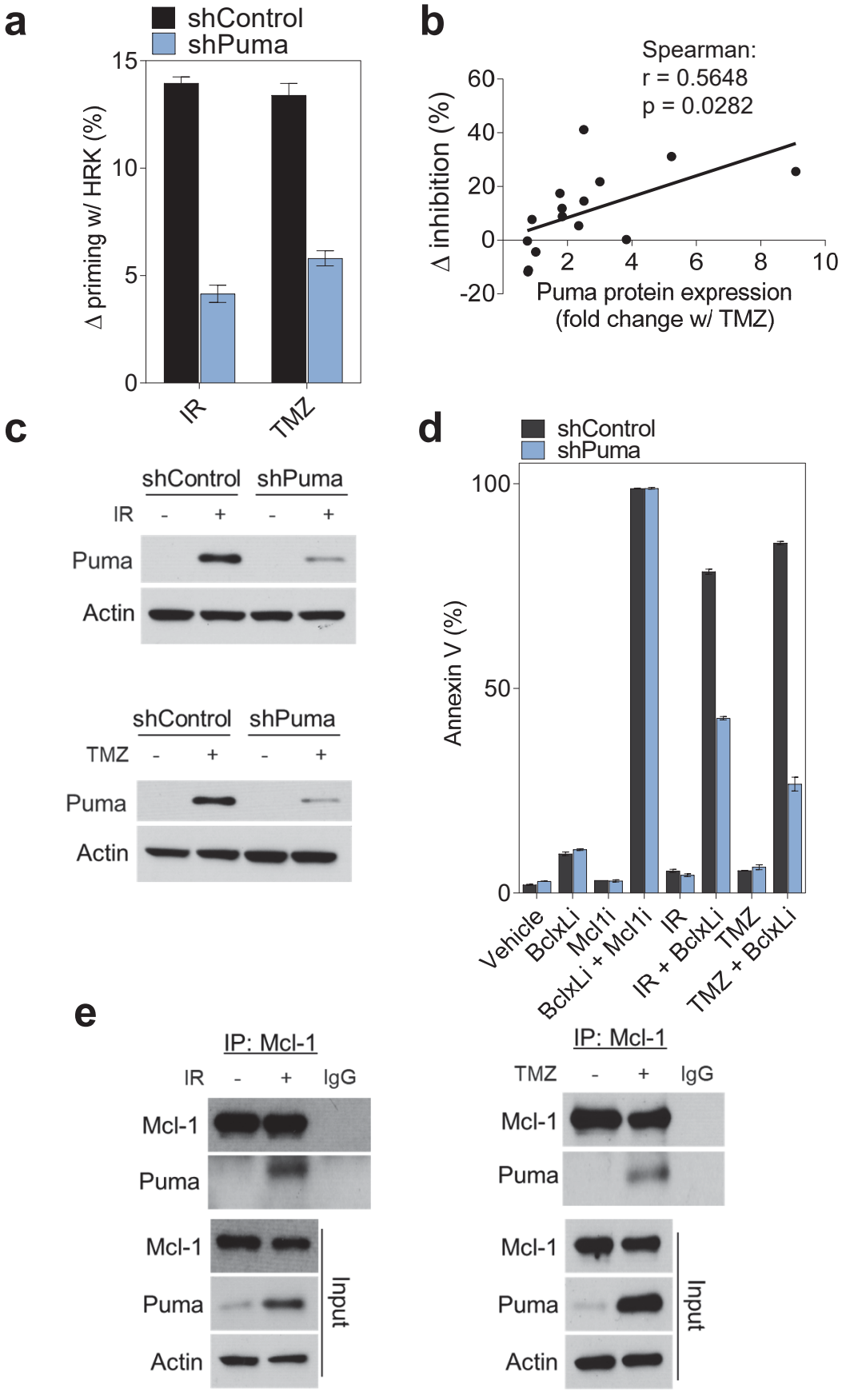

Figure 3. Puma is essential for the apoptotic effects of IR/TMZ. (a) The % change, relative to vehicle control, in apoptotic priming as determined by cytochrome *c* release following BH3 profiling using HRK in GS025 shControl and shPuma following IR or TMZ treatment for 24 hours. **(b)** Correlation between enhanced therapeutic efficacy with TMZ +/- Bcl-xL inhibition (as described in **Fig. 2b**) and induction of Puma protein expression with TMZ, relative to vehicle control. Spearman r = 0.5648, p = 0.0282. **(c)** Immunoblot of indicated proteins of GS025 shControl and shPuma following 48 hours of IR (top) or TMZ (bottom) treatment. **(d)** Annexin V staining of GS025 shControl and shPuma following indicated treatments for 72 hours. **(e)** Immunoprecipitation of Mcl-1 in GS025 following 48 hours of IR (left) or TMZ (right) treatment. Immunoprecipitation was performed with immunoglobulin G control antibody or anti-Mcl-1 antibody, and the immunoprecipitate was probed with the indicated antibodies. Below are respective pre-immunoprecipitation lysates (input). For BH3-profiling, the concentration of HRK was 100 μM. Dose of IR was 20 gy. Concentration of TMZ was 300 μM. Concentration of BclxLi and Mcl1i were both 1 μM.

Chapter 1 - Figure 4

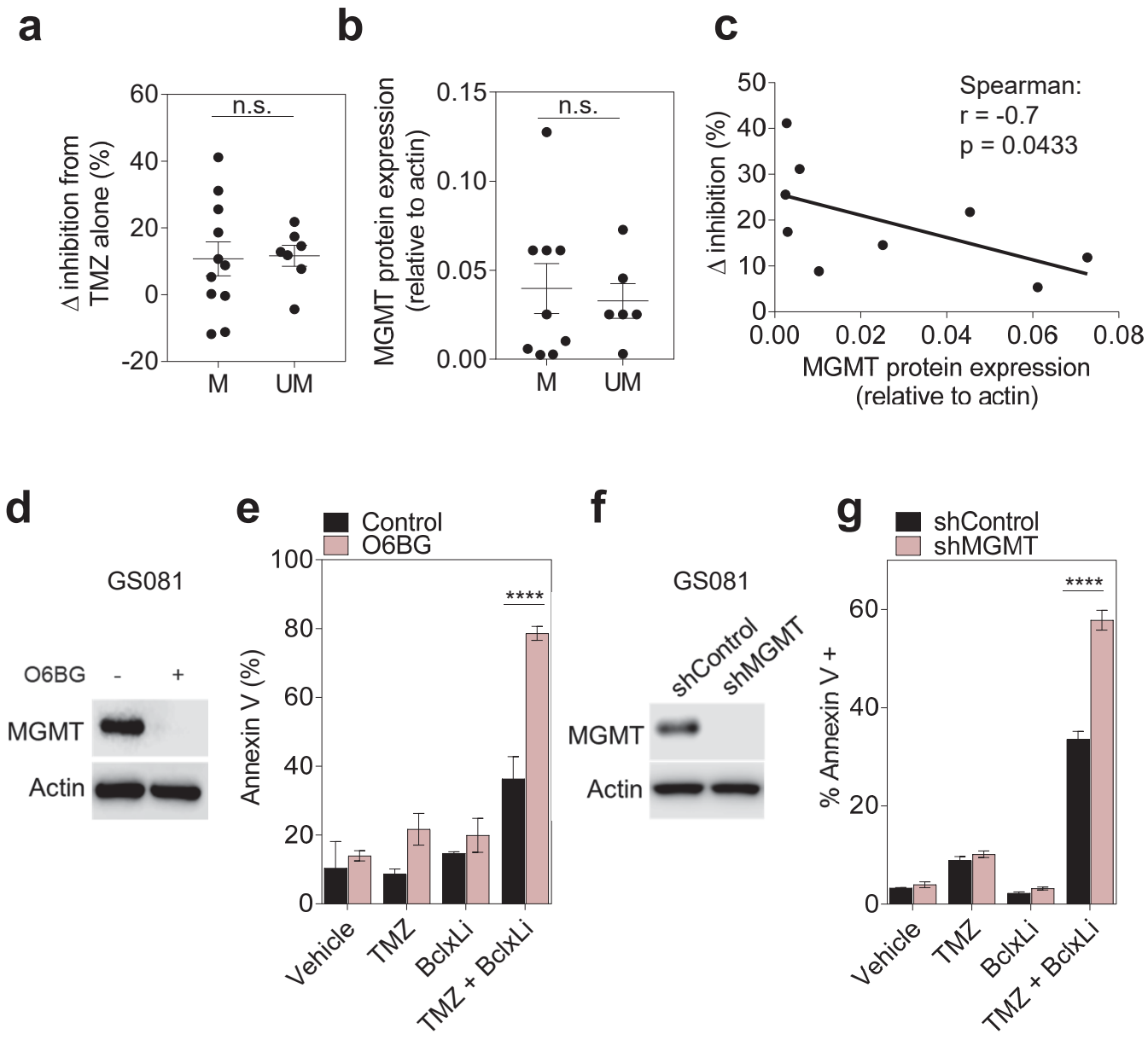

Figure 4. Elevated MGMT protein levels hinder apoptotic response to TMZ + Bcl-xL inhibition. (a) Difference in therapeutic efficacy of TMZ +/- BclxLi in methylated (M) and unmethylated (UM) patient-derived GBM cells. % viability is assessed by Cell Titer Glo and compared to TMZ treatment alone. **(b)** MGMT protein expression, relative to actin, in M and UM patient-derived GBM cells. **(c)** Correlation between enhanced therapeutic efficacy with TMZ +/- Bcl-xL inhibition (as described in **Fig. 2b**) and MGMT protein expression in a panel of patient-derived GBM cells. Spearman r = -0.7, p = 0.0433. **(d)** Immunoblot of indicated proteins of GS025 treated with O6BG for 24 hours. **(e)** Annexin V staining of GS025 following indicated treatments for 72 hours and with our without 24 hours of O6BG pre-treatment. **(f)** Immunoblot of indicated proteins of GS025 shControl and shMGMT. **(g)** Annexin V staining of GS025 following indicated treatments for 72 hours. Dose of IR was 20 gy. Concentration of O6BG, TMZ, and BclxLi were 40 μM, 300 μM, and 1 μM, respectively. Comparisons were made using two-tailed unpaired Student's *t*-test. ****p<0.0001.

Chapter 1 -
Supplementary Figure 1

a

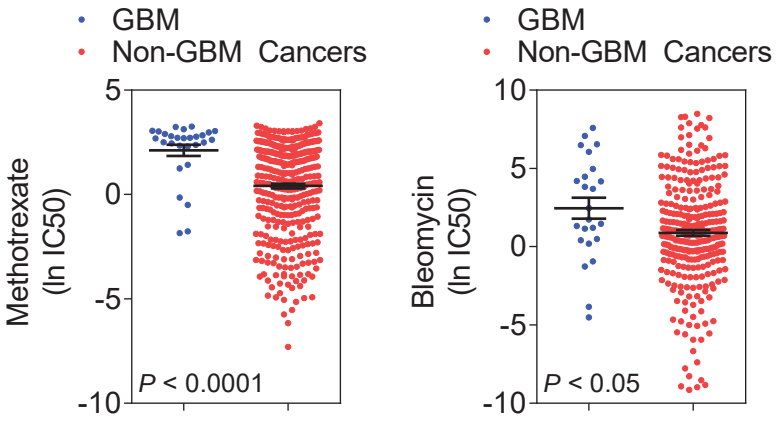

b

Chemotherapy	Mean ln IC50 in GBM	Mean ln IC50 in non-GBM	*P* value
Methotrexate	2.12	0.489	< 0.0001
Bleomycin	2.458	0.881	0.0249
Mitomycin C	-0.516	-1.393	0.0629
Gemcitabine	-1.629	-3.028	0.0912
Etoposide	2.269	1.591	0.1549
Doxorubicin	-1.557	-2.061	0.2195
Cisplatin	3.193	3.443	0.4182
Cytarabine	0.858	0.628	0.5411
Vinorelbine	-3.515	-3.797	0.5020
Camptothecin	-4.744	-4.816	0.8604
Paclitaxel	-2.425	-2.019	0.5920
Vinblastine	-4.165	-4.067	0.7604
Docetaxel	-5.953	-5.156	0.0196

Supplementary Figure 1. GBM have intrinsic resistance to clinically approved therapies *in vitro*. **(a)** Dose response of GBM cell lines compared to non-GBM cancer[5]. Methotrexate and bleomycin are shown as representation. Data is shown as ln IC50. **(b)** Table of all 13 clinically approved therapies tested comparing responses from GBM cell lines and non-GBM cancers. Comparisons were made using two-tailed unpaired Student's *t*-test.

Chapter 1 -
Supplementary Figure 2

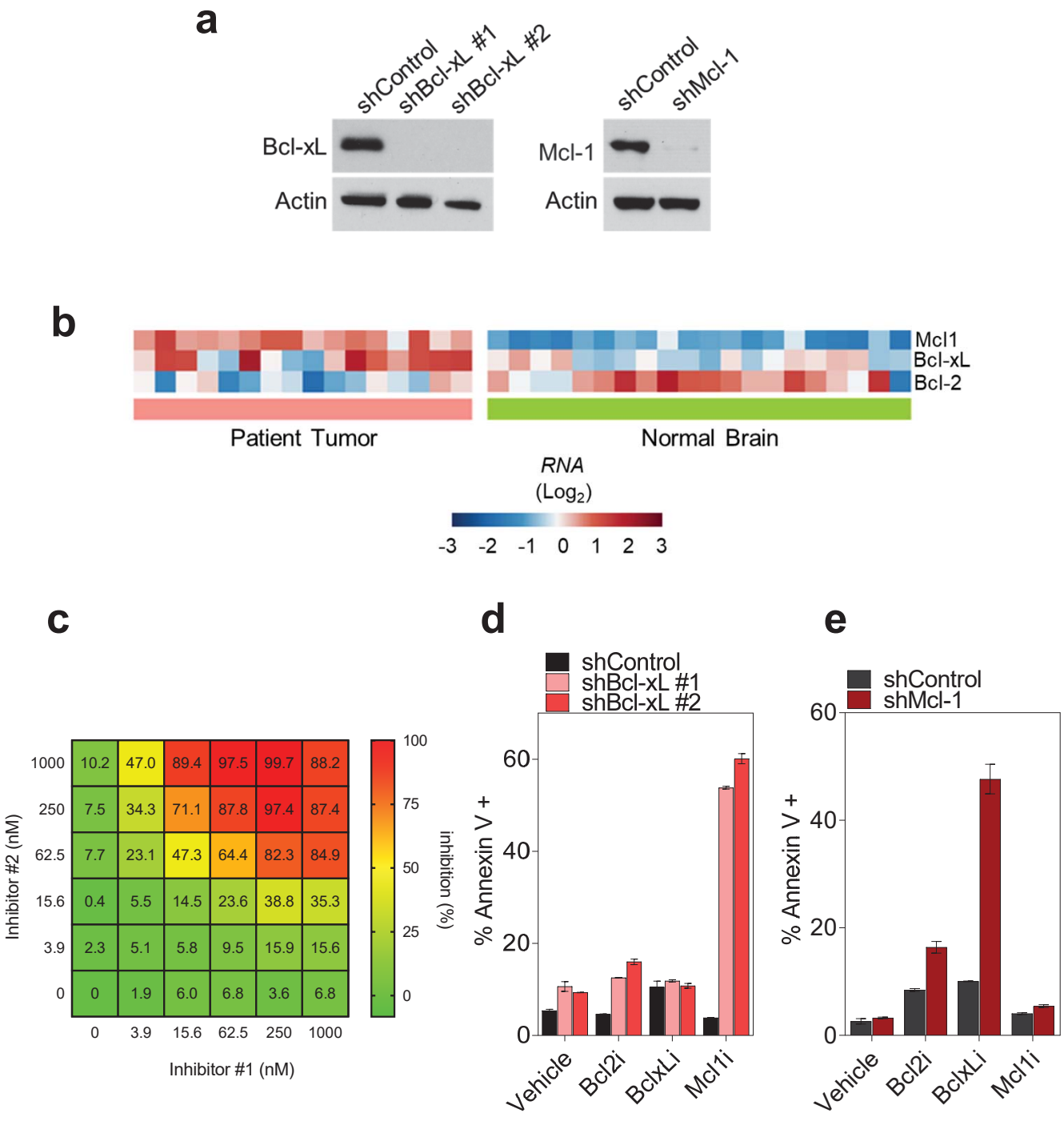

Supplementary Figure 2. GBM rely on Bcl-xL and Mcl-1 for survival. **(a)** Immunoblot of indicated proteins of GS025 shControl, shBcl-xL #1, shBcl-xL #2, and shMcl-1 #1. **(b)** Gene expression analysis comparing GBM patient tumor cells and normal brain tissue for expression of Mcl-1, Bcl-xL, and Bcl-2. Data is displayed as a heat map with a scale of $\log_2$. **(c)** Representative dose-titration matrix (6x6 concentrations) displaying cellular viability in GBM cells treated with varying concentrations of Bcl2i, BclxLi, Mcl1i, and in combination. **(d)** Annexin V staining of GS025 shControl, shBcl-xL #1, and shBcl-xL #2 following indicated treatments for 48 hours. **(e)** Same as **(d)** but in GS025 shControl and shMcl-1 cells. For annexin V measurements, concentrateon of Bcl2i, BclxLi, and Mcl1i were all 1 μM.

Chapter 1 -
Supplementary Figure 3

a

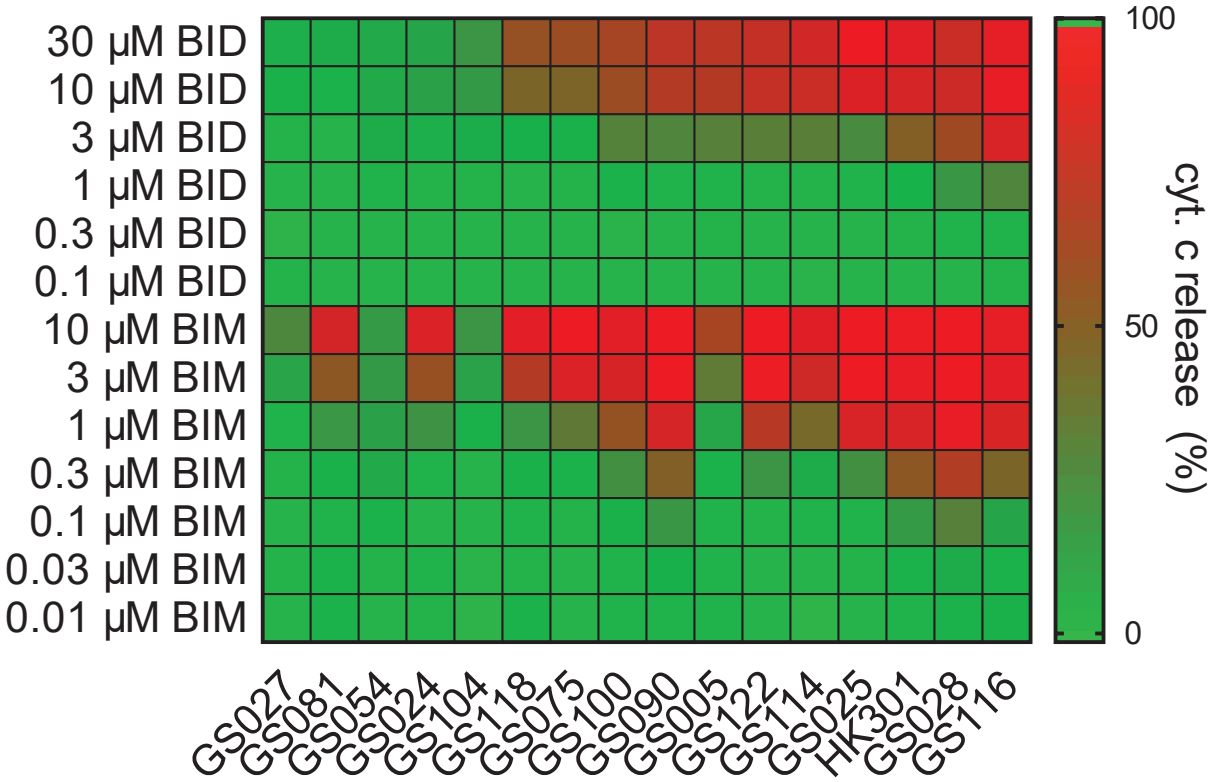

b

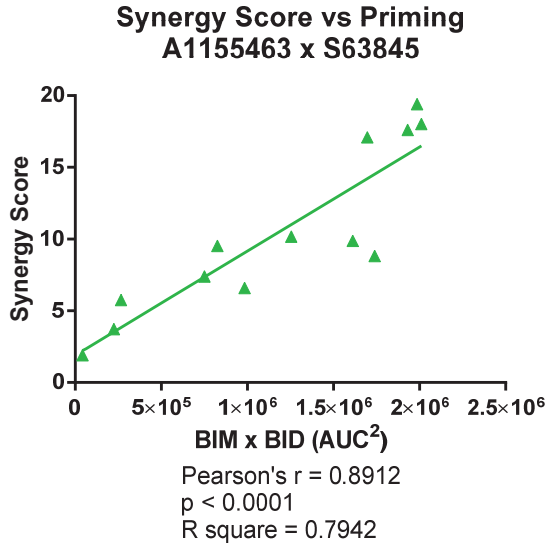

Supplementary Figure 3. Basal primed states of GBM correlate with response. (a) Cytochrome *c* release (%) following BH3 profiling using a dose titration of universal activators BIM and BID peptides in a panel of patient-derived GBM cells. **(b)** Correlation between synergy score of BclxLi + Mcl1i (see **Fig. 1c**) and response to BIM x BID peptides from **(a)**. Pearson's r = 0.08912, $p < 0.0001$.

Chapter 1 -
Supplementary Figure 4

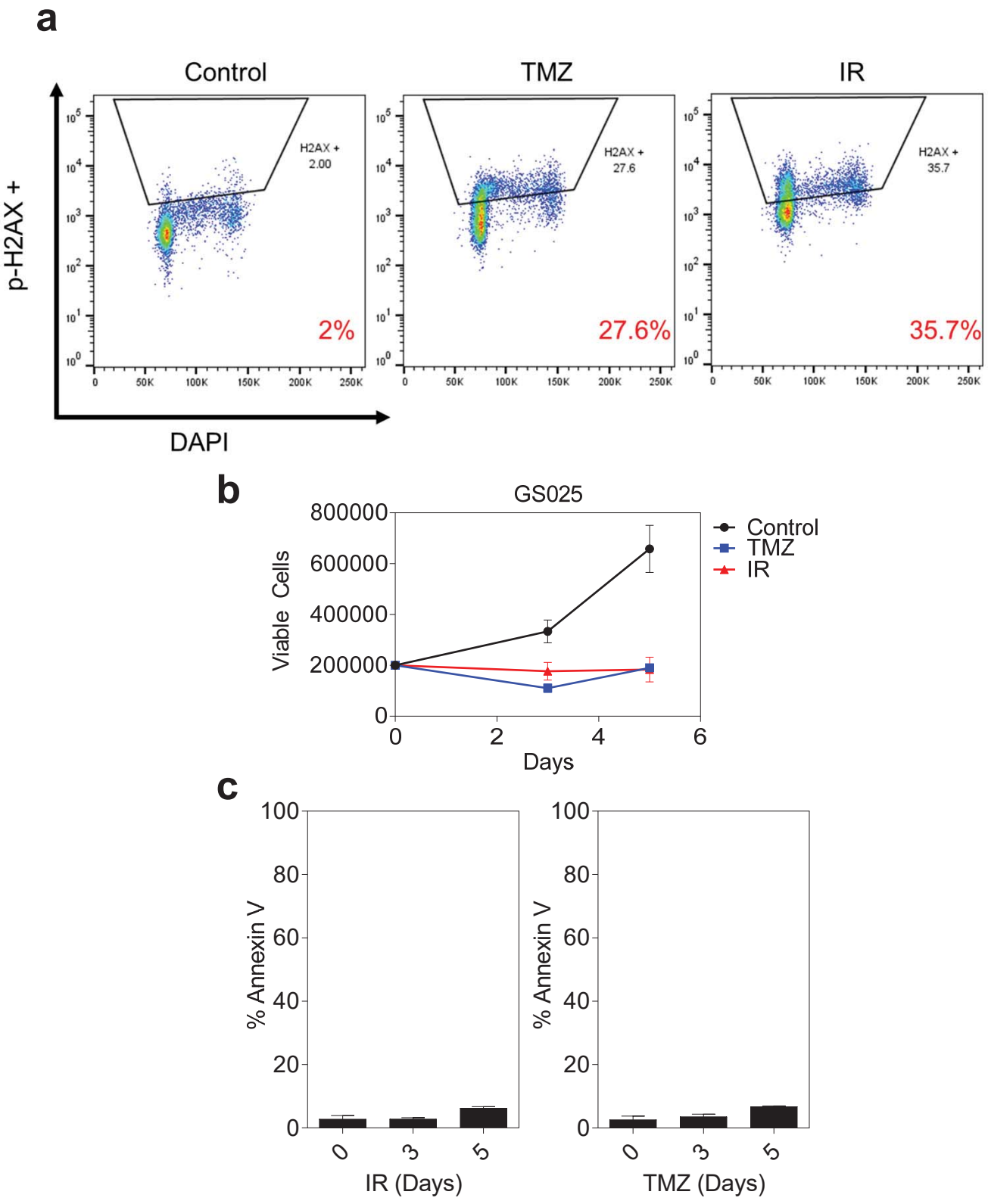

Supplementary Figure 4. Effects of IR and TMZ on GBM. (a) Induction of DNA damage in GS025 following 24 hours of IR and TMZ treatment, as measured by pH2A.X staining. DAPI is used to stain for cell cycle. **(b)** Growth curve of GS025 cells treated with IR and TMZ over 5 days. **(c)** Annexin V staining of GS025 following IR or TMZ treatment for 3 days or 5 days. Dose of IR was 20 gy. Concentration of TMZ was 300 μM.

Chapter 1 -
Supplementary Figure 5

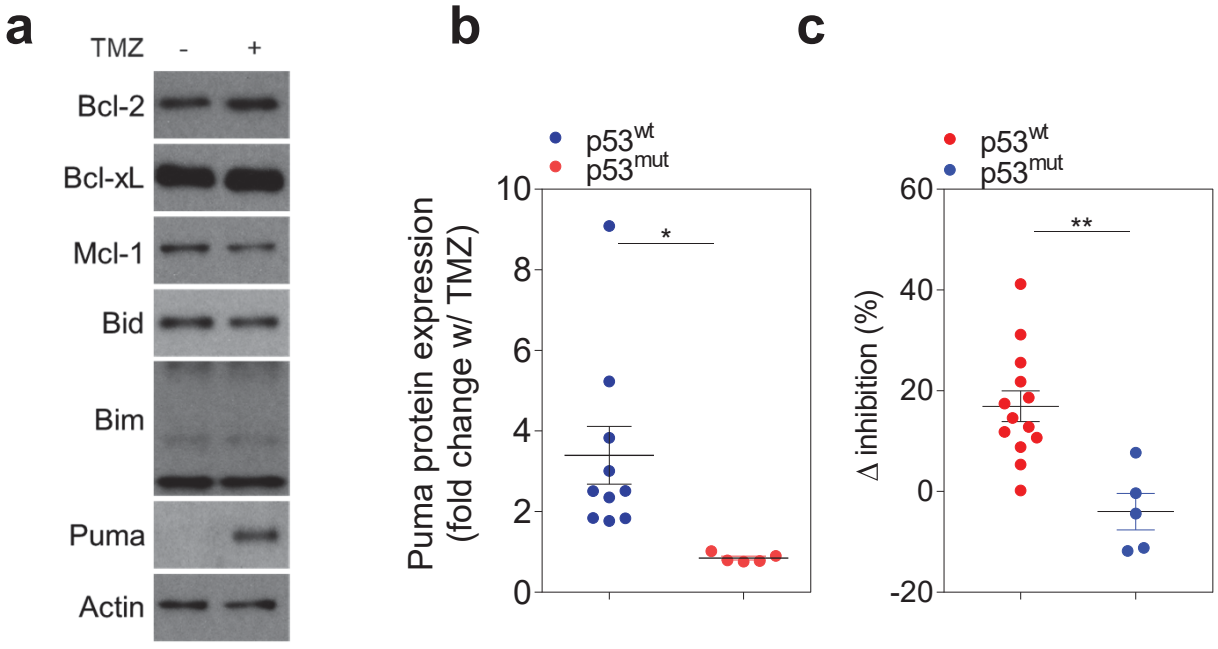

Supplementary Figure 5. Changes in Bcl-2 family proteins. (a) Immunoblot of indicated proteins of GS025 cells treated with TMZ for 48 hours. **(b)** Induced Puma protein expression, relative to vehicle control, in $p53^{wt}$ and $p53^{mut}$ cells. **(c)** Difference in therapeutic efficacy of TMZ +/- BclxLi in $p53^{wt}$ and $p53^{mut}$ cells. % viability is assessed by Cell Titer Glo and compared to TMZ treatment alone.

Chapter 1 -
Supplementary Figure 6

a

Cell Line	Methylation Status	Cell Line	Methylation Status
GS001	Methylated	GS028	Unmethylated
GS005	Methylated	GS054	Unmethylated
GS013	Methylated	GS081	Unmethylated
GS024	Methylated	GS090	Unmethylated
GS025	Methylated	GS100	Unmethylated
GS075	Methylated	GS104	Unmethylated
GS102	Methylated	GS116	Unmethylated
GS114	Methylated		
GS118	Methylated		
GS122	Methylated		
HK301	Methylated		

b

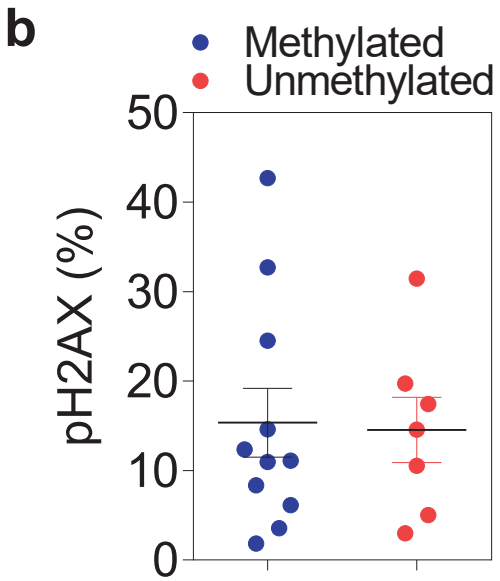

Supplementary Figure 6. Methylation status in panel of patient-derived GBM cells. (a) Table of methylation status across GBM samples, as determined by PCR. **(b)** Induction of DNA damage in methylated and unmethylated GBM cells following 24 hours of TMZ treatment, as measured by pH2A.X staining.

REFERENCES

1 Hanahan, D. & Weinberg, Robert A. Hallmarks of Cancer: The Next Generation. *Cell* **144**, 646-674, doi:10.1016/j.cell.2011.02.013.

2 Deng, J. *et al.* BH3 profiling identifies three distinct classes of apoptotic blocks to predict response to ABT-737 and conventional chemotherapeutic agents. *Cancer Cell* **12**, 171-185, doi:10.1016/j.ccr.2007.07.001 (2007).

3 Sarosiek, K. A. *et al.* Developmental Regulation of Mitochondrial Apoptosis by c-Myc Governs Age- and Tissue-Specific Sensitivity to Cancer Therapeutics. *Cancer Cell* **31**, 142-156, doi:10.1016/j.ccell.2016.11.011 (2017).

4 Vivanco, I. *et al.* Differential sensitivity of glioma- versus lung cancer-specific EGFR mutations to EGFR kinase inhibitors. *Cancer Discov* **2**, 458-471, doi:2159-8290.CD-11-0284 [pii] 10.1158/2159-8290.CD-11-0284 (2012).

5 Garnett, M. J. *et al.* Systematic identification of genomic markers of drug sensitivity in cancer cells.

6 Souers, A. J. *et al.* ABT-199, a potent and selective BCL-2 inhibitor, achieves antitumor activity while sparing platelets. *Nat Med* **19**, 202-208, doi:10.1038/nm.3048 (2013).

7 Simões-Wüst, A. P. *et al.* bcl-xl antisense treatment induces apoptosis in breast carcinoma cells. *International Journal of Cancer* **87**, 582-590, doi:doi:10.1002/1097-0215(20000815)87:4<582::AID-IJC19>3.0.CO;2-P (2000).

8 Kotschy, A. *et al.* The MCL1 inhibitor S63845 is tolerable and effective in diverse cancer models. *Nature* **538**, 477-482, doi:10.1038/nature19830 http://www.nature.com/nature/journal/v538/n7626/abs/nature19830.html#supplementary-information (2016).

9 Lehar, J. *et al.* Synergistic drug combinations tend to improve therapeutically relevant selectivity. *Nat Biotechnol* **27**, 659-666, doi:10.1038/nbt.1549 (2009).

10 Ni Chonghaile, T. *et al.* Pretreatment mitochondrial priming correlates with clinical response to cytotoxic chemotherapy. *Science* **334**, 1129-1133, doi:10.1126/science.1206727 (2011).

11 Hata, A. N., Engelman, J. A. & Faber, A. C. The BCL2 Family: Key Mediators of the Apoptotic Response to Targeted Anticancer Therapeutics. *Cancer Discovery* **5**, 475-487, doi:10.1158/2159-8290.cd-15-0011 (2015).

12 Ham, J. *et al.* Exploitation of the Apoptosis-Primed State of MYCN-Amplified Neuroblastoma to Develop a Potent and Specific Targeted Therapy Combination. *Cancer Cell* **29**, 159-172, doi:10.1016/j.ccell.2016.01.002.

13 Deng, J. *et al.* Bruton's tyrosine kinase inhibition increases BCL-2 dependence and enhances sensitivity to venetoclax in chronic lymphocytic leukemia. *Leukemia* **31**, 2075, doi:10.1038/leu.2017.32 https://www.nature.com/articles/leu201732#supplementary-information (2017).

14 Hegi, M. E. *et al.* MGMT Gene Silencing and Benefit from Temozolomide in Glioblastoma. *New England Journal of Medicine* **352**, 997-1003, doi:10.1056/NEJMoa043331 (2005).

15 Kitange, G. J. *et al.* Evaluation of MGMT Promoter Methylation Status and Correlation with Temozolomide Response in Orthotopic Glioblastoma Xenograft Model. *Journal of neuro-oncology* **92**, 23-31, doi:10.1007/s11060-008-9737-8 (2009).

16 Quinn, J. A. *et al.* Phase II Trial of Temozolomide Plus O(6)-Benzylguanine in Adults With Recurrent, Temozolomide-Resistant Malignant Glioma. *Journal of Clinical Oncology* **27**, 1262-1267, doi:10.1200/JCO.2008.18.8417 (2009).

17 Chahal, M. *et al.* O(6)-Methylguanine-DNA Methyltransferase Is a Novel Negative Effector of Invasion in Glioblastoma Multiforme. *Molecular Cancer Therapeutics* **11**, 2440 (2012).

18 Enting, R. H. *et al.* Radiotherapy plus concomitant and adjuvant temozolomide for leptomeningeal pilomyxoid astrocytoma: a case study. *J Neurooncol* **80**, 107-108, doi:10.1007/s11060-006-9151-z (2006).

19 Roberts, A. W. *et al.* Targeting BCL2 with Venetoclax in Relapsed Chronic Lymphocytic Leukemia. *New England Journal of Medicine* **374**, 311-322, doi:doi:10.1056/NEJMoa1513257 (2016).

20 Konopleva, M. *et al.* Efficacy and Biological Correlates of Response in a Phase II Study of Venetoclax Monotherapy in Patients with Acute Myelogenous Leukemia. *Cancer Discovery* **6**, 1106 (2016).

21 Cang, S., Iragavarapu, C., Savooji, J., Song, Y. & Liu, D. ABT-199 (venetoclax) and BCL-2 inhibitors in clinical development. *Journal of Hematology & Oncology* **8**, 129, doi:10.1186/s13045-015-0224-3 (2015).

22 Jones, J. A. *et al.* Venetoclax for chronic lymphocytic leukaemia progressing after ibrutinib: an interim analysis of a multicentre, open-label, phase 2 trial. *The Lancet Oncology* **19**, 65-75, doi:10.1016/S1470-2045(17)30909-9.

23 Venetoclax Data Prompt Rethink of CLL Therapy. *Cancer Discovery* (2018).

24 Mai, W. X. *et al.* Cytoplasmic p53 couples oncogene-driven glucose metabolism to apoptosis and is a therapeutic target in glioblastoma. *Nature Medicine* **23**, 1342, doi:10.1038/nm.4418 https://www.nature.com/articles/nm.4418#supplementary-information (2017).

25 Corcoran, Ryan B. *et al.* Synthetic Lethal Interaction of Combined BCL-XL and MEK Inhibition Promotes Tumor Regressions in KRAS Mutant Cancer Models. *Cancer Cell* **23**, 121-128, doi:10.1016/j.ccr.2012.11.007.

26 Nakajima, W., Hicks, M. A., Tanaka, N., Krystal, G. W. & Harada, H. Noxa determines localization and stability of MCL-1 and consequently ABT-737 sensitivity in small cell lung cancer. *Cell Death &Amp; Disease* **5**, e1052, doi:10.1038/cddis.2014.6 https://www.nature.com/articles/cddis20146#supplementary-information (2014).

27 Chipuk, J. E., Bouchier-Hayes, L., Kuwana, T., Newmeyer, D. D. & Green, D. R. PUMA couples the nuclear and cytoplasmic proapoptotic function of p53. *Science* **309**, 1732-1735, doi:10.1126/science.1114297 (2005).

CHAPTER 2:

Cytoplasmic p53 Couples Oncogene-driven Glucose Metabolism to Apoptosis and is a Therapeutic Target in Glioblastoma

ABSTRACT

Cross-talk among oncogenic signaling and metabolic pathways may create opportunities for novel therapeutic strategies in cancer. Here we show that acute inhibition of EGFR-driven glucose metabolism induces minimal cell death, yet lowers the apoptotic threshold in a subset of patient-derived glioblastoma (GBM) cells. Mechanistic studies revealed that, following attenuated glucose consumption, Bcl-xL blocks cytoplasmic p53 from triggering intrinsic apoptosis. Consequently, pharmacological stabilization of p53 with the brain-penetrant small molecule, Idasanutlin, in combination with targeting EGFR-driven glucose metabolism promoted synthetic lethality in orthotopic xenograft models. Notably, neither inhibition of EGFR signaling, nor genetic analysis of EGFR, was sufficient to predict sensitivity to this new therapeutic combination. Conversely, rapid changes in ^{18}F-fluorodeoxyglucose (^{18}F-FDG) uptake using non-invasive positron emission tomography was an effective predictive biomarker of response in vivo. Together, these studies identify a critical link between oncogene signaling, glucose metabolism, and cytoplasmic p53, which could be exploited for combination therapy in GBM and potentially, other malignancies.

INTRODUCTION

Molecularly targeted therapies have revolutionized cancer treatment and paved the path for modern precision medicine. However, despite well-defined actionable genetic alterations[1], targeted drugs have failed in glioblastoma (GBM) patients. This is in large part due to insufficient brain penetration of most targeted agents to levels necessary for tumor kill[2]; this insufficient abundance in the target tissue may induce the development of adaptive mechanisms that drive drug resistance[3]. While therapeutic combinations that target both the primary genetic lesion and the compensatory signaling pathway(s) that promote resistance are appealing, these combination therapy strategies have been hampered by toxicities, requiring subthreshold dosing of each drug[4,5]. Owing to the dismal prognosis for GBM patients, and the poor efficacy of conventional approaches, new therapeutic strategies are critically needed.

An alternative therapeutic approach—synthetic lethality—targets an oncogenic driver to modify an important functional property for tumorigenesis, rendering cells vulnerable to an orthogonal second hit[6]. This strategy may be particularly attractive when the oncogene-regulated functional network(s) modulate tumor cell death pathways. In a notable example, oncogenic signaling drives glucose metabolism to suppress the intrinsic (or mitochondria-dependent) apoptotic pathway and prevent cell death[7,8]. Consequently, inhibition of oncogenic drivers with targeted therapies can trigger the intrinsic apoptotic machinery as a direct consequence of attenuated glucose consumption[7]. The intertwined nature of these tumorigenic pathways may present therapeutic opportunities for rational combination treatments, but this has yet to be investigated.

Previous work demonstrated that the epidermal growth factor receptor (EGFR) – mutated and/or amplified in ~60% of GBM patients [9] – regulates glucose metabolism[10]. Whether targeting EGFR-driven glucose utilization alters the dynamics of the intrinsic apoptotic machinery in cancer is unknown. Here we hypothesized that a deeper understanding of this relationship will reveal pharmacological vulnerabilities for enhanced tumor killing in GBM.

RESULTS

EGFR inhibitor metabolic responders and non-responders

We first characterized the changes in glucose uptake induced by acute EGFR inhibition across 19 patient-derived GBM cell lines. The cells were cultured in supplemented serum-free medium as gliomaspheres which, in contrast to serum-based culture conditions, preserve many of the molecular features of patient tumors[11,12]. Treatment with the EGFR tyrosine kinase inhibitor erlotinib revealed a subset of GBMs whose radio-labeled glucose uptake (^{18}F-FDG) was significantly attenuated, hereafter termed “metabolic responders” (**Fig. 1a and Supplementary Fig. 1a**). Silencing of *EGFR* using siRNA confirmed that the reduction in glucose uptake was not due to off-target effects of erlotinib (**Supplementary Fig. 1b, c**). Reduced ^{18}F-FDG uptake was associated with, as determined from a randomly selected cohort of metabolic responders, decreased lactate secretion, glucose consumption, and extracellular acidification rate (ECAR), yet glutamine levels remained unchanged (**Fig. 1b and Supplementary Fig. 1d-g**). Suppressed glucose utilization also correlated with a decrease in RAS-MAPK and PI3K-AKT-mTOR signaling – each of which can regulate glucose metabolism in GBM and other cancers [10,13,14] (**Supplementary Fig. 2a**).

In contrast, no “non-responder” GBMs (**Fig. 1a and Supplementary Fig. 1b, c**), showed reduced glucose consumption, lactate secretion, or ECAR despite robust inhibition of EGFR activity (**Fig. 1b and Supplementary Fig. 1d-g**) (**Supplementary Fig. 2b**). Moreover, RAS-MAPK and PI3K-AKT-mTOR signaling were unchanged in nearly all metabolic non-responders (**Supplementary Fig. 2b**). Notably, while all metabolic responders had alterations in *EGFR* (mutation and/or amplification, polysomy), 6 GBM lines without a metabolic response also contained *EGFR* mutations and/or copy number gains (**Supplementary Fig. 3a, b**). Taken together, these data illustrate two key points. First, acute inhibition of EGFR rapidly attenuates glucose utilization in a

subset of primary GBM cells, and second, genetic alterations in *EGFR* could not alone predict which GBMs have a metabolic response to EGFR inhibition.

Metabolic responders are primed for apoptosis

Perturbations in glucose metabolism can induce the expression of pro-apoptotic factors and promote intrinsic apoptosis[15], leading us to posit that reduced glucose uptake in response to EGFR inhibition would stimulate the intrinsic apoptotic pathway. Indeed, acute erlotinib treatment enhanced the expression of the pro-apoptotic BH3-only proteins, BIM and PUMA, only in the metabolic responder cultures (**Supplementary Fig. 4a**). However, annexin V staining revealed that the metabolic responders had only modest (~17% cells annexin V positive), albeit significantly higher, apoptosis compared with non-responders (~3% cells annexin V positive), following 72 hours of erlotinib exposure (**Fig. 1c**).

The relatively low level of apoptosis in metabolic responder GBMs, despite pronounced induction of pro-apoptotic factors, led us to ask if perturbing glucose uptake with erlotinib simply "primes" GBM cells for apoptosis; thus increasing the propensity for apoptosis without inducing considerable cell death[16]. The induction of a primed apoptotic state, or a shift in the death threshold, can be measured by BH3 profiling; which, is conducted via exposing the mitochondria of drug-treated cells to synthetic pro-apoptotic BH3 peptides (e.g., BIM, BID, and/or PUMA) and then quantifying the changes in mitochondria potential – via cytochrome *c* release – to precisely determine the proximity of cells to intrinsic apoptosis[17]. Accordingly, we treated both metabolic responders and non-responders for 24 hours and performed BH3 profiling using multiple BH3 peptides across various concentrations (**Supplementary Fig. 4b**). We observed heightened apoptotic priming - as determined by the change in cytochrome *c* release relative to vehicle - in the metabolic responders with erlotinib treatment (**Fig. 1d**). Importantly, priming in the metabolic

responders was significantly higher than priming in the non-responders (**Fig. 1d**), supporting the premise that attenuated glucose uptake with EGFR inhibition triggers apoptotic priming in GBM.

We reasoned that if reduced glucose uptake is required for apoptotic priming with targeting EGFR, rescuing glucose consumption should mitigate these effects. Given that EGFR inhibition can abrogate the expression/localization of glucose transporters 1 (GLUT1) and 3 (GLUT3) (**Supplemental Fig. 5a**)[10], we ectopically expressed both GLUT1 and GLUT3 in two metabolic responder GBMs (HK301 and GBM39) to sustain glucose flux under erlotinib treatment. Enforced expression of GLUT1 and GLUT3 (GLUT1/3) rescued erlotinib-mediated attenuation of glucose consumption and lactate secretion in both cell lines (**Fig. 1e and Supplementary Fig. 5b - d**) and, importantly, markedly suppressed apoptotic priming in response to EGFR inhibition (**Fig. 1f**). Collectively, these data demonstrate that erlotinib-mediated inhibition of glucose metabolism, although insufficient to induce meaningful cell death, lowers the apoptotic threshold potentially rendering GBM cells vulnerable to agents that exploit this primed state.

Cytoplasmic p53 is required for apoptotic priming

Next, we investigated the mechanism by which GBMs become primed for apoptosis after treatment with erlotinib. In cells that are primed, the anti-apoptotic Bcl-2 family proteins (e.g. Bcl-2, Bcl-xL, Mcl-1) are largely loaded with pro-apoptotic BH3 proteins (e.g., BIM, BID, PUMA, BAD, NOXA, HRK); consequently, cells are dependent on these interactions for survival[16]. The tumor suppressor protein, p53, upregulates expression of pro-apoptotic proteins that subsequently need to be sequestered by anti-apoptotic Bcl-2 proteins to prevent cell death[18]. To examine whether p53 is required for erlotinib-induced priming, we abrogated p53 expression in two metabolic responders (HK301 and HK336) using CRISPR-Cas9 targeting *TP53*; the resulting cells are hereafter referred to as p53KO (**Fig. 2a**). While the change in glucose uptake with erlotinib was

unaffected in p53KO cells (**Supplementary Fig. 6a**), BH3 profiling revealed p53KO nearly abolished erlotinib-induced apoptotic priming (**Fig. 2b**)

As transcription of p53 target genes has been shown to be enhanced under glucose limitation[15,19,20], we tested whether p53-mediated transcription was induced by EGFR inhibition. However, erlotinib neither increased the expression of p53-regulated genes (e.g., *p21*, *MDM2*, *PIG3*, *TIGAR*) (**Supplementary Fig. 6b**), nor induced p53-luciferase reporter activity in HK301 metabolic responder cells (**Supplementary Fig. 6c**). These data indicate that while p53 is required for priming with EGFR inhibition, its transcriptional activity may not be necessary.

In addition to p53's well-described nuclear functions, p53 can localize in the cytoplasm where it can directly engage the intrinsic apoptotic machinery via interactions with pro-apoptotic and/or anti-apoptotic Bcl-2 family members[21,22]. To evaluate whether cytoplasmic p53 is important for apoptotic priming with erlotinib, we stably introduced a p53 mutant with a defective nuclear localization signal ($p53^{cyto}$)[23] into HK301 and HK336 p53KO gliomaspheres. As expected, $p53^{cyto}$ was expressed (**Fig. 2c and Supplemental Fig. 6d**), restricted to the cytoplasm (**Fig. 2d and Supplemental Fig. 6e**) and had no transcriptional activity (**Fig. 2e and Supplemental Fig. 2f**). Conversely, reconstitution of wild-type p53 ($p53^{wt}$) in HK301 and HK336 p53KO cells displayed similar localization as parental cells and rescued transcription of p53-regulated genes (**Fig. 2c - e and Supplemental Fig. 6e - g**). Stable introduction of $p53^{cyto}$ significantly restored priming with erlotinib in both HK301 and HK336 p53KO cells to levels comparable to $p53^{wt}$ (**Fig. 2f and Supplemental Fig. 6g**), indicating that the cytoplasmic function of p53 is required for erlotinib-mediated priming. In support of this conclusion, introduction of a transcriptionally active (**Fig. 2g**), yet nuclear-confined p53 mutant ($p53^{NES}$) into HK301 p53KO cells failed to induce erlotinib-mediated apoptotic priming (**Fig. 2g, h and Supplemental Fig. 6h**). Finally, pharmacological inhibition of cytoplasmic p53 activity with pifithrin-μ (PFTμ)[24] markedly reduced priming with

erlotinib (**Supplementary Fig. 6i**). Collectively, these results show that cytoplasmic p53 engages the intrinsic apoptotic machinery following treatment with erlotinib in GBM metabolic responder samples.

Prior work demonstrated that *TP53* mutations detected in human tumors – specifically those in the DNA binding domain – have diminished cytoplasmic functions in addition to transactivation deficiencies[22,25]. Thus, we asked whether stable expression of two of these "hotspot" p53 mutants, R175H or R273H, in HK301 p53KO would have reduced EGFRi-mediated apoptotic priming (**Supplementary Fig. 6h**). As expected, both mutants lacked transcriptional capabilities (**Fig. 2g**) and, consistent with reduced cytoplasmic activity, were incapable of priming with erlotinib (**Fig. 2h**). Therefore, in line with previous findings, oncogenic mutations in the DNA binding domain of p53 result in "dual hits"[26], whereby both transactivation and cytoplasmic functions are abrogated – the latter having implications for apoptotic priming with EGFR inhibition.

Inhibition of glucose uptake creates therapeutic vulnerability

Bcl-xL can sequester cytoplasmic p53 and prevent p53-mediated apoptosis; thus creating a primed apoptotic state and a dependency on Bcl-xL for survival[27]. Indeed, BH3 profiling revealed a reliance on Bcl-xL to block apoptosis in erlotinib metabolic responders (**Supplementary Fig. 7a**). Therefore, we hypothesized that attenuated glucose consumption with EGFR inhibition may result in the sequestration of cytoplasmic p53 by Bcl-xL. To investigate this, we performed co-immunoprecipitations to examine the dynamics of p53-Bcl-xL interactions in response to erlotinib in both responders (n=2) and non-responders (n=2). Importantly, we observed increased Bcl-xL and p53 complex formation with erlotinib treatment in metabolic responders (**Fig. 3a**) but not in non-responders (**Fig. 3b**). This suggests that inhibition of EGFR-dependent glucose consumption results in sequestration of p53 by Bcl-xL. Consistent with this interpretation, ectopic expression of GLUT1/3, which rescues the erlotinib-mediated reduction in glucose uptake and apoptotic

priming, prevented the association of p53 with Bcl-xL (**Fig. 3c and Supplementary Fig. 7b**). These findings strongly indicate that erlotinib-mediated inhibition of glucose uptake primes GBM cells for apoptosis by promoting an interaction between cytoplasmic p53 and Bcl-xL.

Disruption of the p53 and Bcl-xL complex can "free" cytoplasmic p53 to stimulate intrinsic apoptosis[27]. Once we detected increased binding between Bcl-xL and p53 in metabolic responders in response to erlotinib, we asked whether the liberation of p53 from Bcl-xL elicits apoptosis. To test this, we treated a metabolic responder (HK301) with erlotinib and the specific Bcl-xL inhibitor, WEHI-539[28]. The addition of WEHI-539 released p53 from Bcl-xL under erlotinib treatment (**Fig. 3d**), leading to synthetic lethality in three metabolic responders (HK301, GBM39, HK336) (**Fig. 3e and Supplementary Fig. 7c**). Notably, cytoplasmic p53 was sufficient for caspase-dependent apoptosis elicited by the drug combination (**Supplementary Fig. 7c, e**). However, WEHI-539 did not enhance apoptosis in a non-responder (HK393) treated with erlotinib, suggesting that attenuation of glucose uptake with EGFR inhibition, and subsequent association between p53 and Bcl-xL, is necessary to lower the apoptotic threshold and generate a dependence on Bcl-xL for survival (**Fig. 3e**). In support of this, enforced expression of GLUT1/3 significantly mitigated cell death with the drug combination (**Fig. 3f and Supplementary Fig. 7d**). Together, these observations indicate that Bcl-xL blocks GBM cell death in response to erlotinib-mediated inhibition of glucose metabolism by sequestering cytoplasmic p53 (**Fig. 3g**).

Combination treatment efficacy in metabolic responders

Our mechanistic studies reveal a potential therapeutic opportunity in EGFR-driven GBMs that will be dependent on functional p53. While the p53 signaling axis is one of the three core pathways altered in GBM[1,29], analysis of the TCGA GBM dataset demonstrated that *TP53* mutations are mutually exclusive with alterations in *EGFR* (**Fig. 4a, b**). Conversely, in most patients with *EGFR* mutations or gains, there are co-occurring alterations that can lead to suppressed p53 activity;

this includes amplification of *MDM2* and/or deletions in the negative regulator of MDM2, p14 ARF, at the *CDKN2A* locus [30,31] (**Fig. 4a, b**). Given these relationships, and the requirement of p53 for priming under erlotinib-attenuated glucose uptake, we hypothesized that stabilization of p53 via MDM2 inhibition may have similar therapeutic effects to Bcl-xL antagonism. Using nutlin – an extensively characterized inhibitor of MDM2[32] – we noted synthetic lethality when paired with erlotinib in a metabolic responder gliomasphere. Greater than 90% of HK301 cells underwent apoptosis with combined erlotinib and nutlin (**Fig. 4c**). In contrast, we observed no synergy between these drugs in a metabolic non-responder (HK393, **Fig. 4c**). We then tested this combination across our panel of primary GBM cells (all p53 wild-type) and found synthetic lethality only in GBMs with a metabolic response to erlotinib, albeit less so in HK423 and HK296 metabolic responders (**Fig. 4d and Supplementary Fig. 8a**)[33]. Silencing of *EGFR* in combination with nutlin also showed selective synergy for metabolic responder cells, suggesting that the effects of the drug combination were not due to any off-target effects of erlotinib (**Supplemental Fig. 8b**). Importantly, enforced expression of GLUT1/3 significantly reduced molecular markers of intrinsic apoptosis – including BAX oligomerization, and cytochrome *c* release - as well as cell death with combined erlotinib and nutlin (**Fig. 4e and Supplementary Fig. 8c**), supporting the concept that attenuated glucose metabolism with EGFR inhibition is required for the synthetic lethality of the drug combination.

We next investigated the role of p53 in eliciting cell death to combined erlotinib and nutlin. As expected, p53KO in two erlotinib metabolic responders (HK301 and HK336) abolished sensitivity to the drug combination (**Fig. 4f and Supplementary Fig. 8g**). Likewise, ectopic expression of Bcl-xL markedly suppressed cell death with combined treatment, consistent with a critical function for Bcl-xL in antagonizing p53-mediated apoptosis (**Supplementary Fig. 8d**). Moreover, similar to our results with Bcl-xL inhibition (e.g., WEHI-539), the addition of nutlin liberated p53 from Bcl-xL under erlotinib treatment (**Fig. 4g**). These data are in agreement with prior observations that

p53 stabilization can stimulate cytoplasmic p53-mediated apoptosis[27,34]. In support of the suggestion that cytoplasmic p53 activity is required for the synergy of erlotinib and nutlin in metabolic responders, blocking cytoplasmic p53 activity with PFTμ significantly mitigated apoptosis elicited with the combination (**Supplementary Fig. 8e**), while HK301 cells containing the nuclear-confined p53 mutant, $p53^{NES}$, were incapable of enhanced cell death with the drug combination (**Supplementary Fig. 8f**). Finally, cells expressing the cancer "hotspot" p53 mutants, R175H and R273H, which have both transactivation and cytoplasmic deficiencies, were completely insensitive to the erlotinib and nutlin combination (**Supplementary Fig. 8f**).

It is noteworthy that while cytoplasmic p53 is absolutely required to promote cell death with combined erlotinib and nutlin, we observed in some instances that both the transcription-dependent (i.e. nuclear) and independent functions of p53 (i.e. cytoplasmic) are needed for optimal execution of synergistic apoptosis with nutlin (**Supplementary Fig. 8g**). These results are consistent with reports that the cytoplasmic functions of p53 can alone execute intrinsic apoptosis[34,35], whereas, in other contexts, may also require its nuclear functions to facilitate cytoplasmic p53 mediated cell kill[27]. Collectively, our results show that combined targeting of EGFR-driven glucose metabolism and p53 can induce marked synthetic lethality in primary GBM; which is dependent on the cytoplasmic functions of p53.

Priming metabolic non-responders for apoptosis

Our data has led us to propose a model where inhibition of EGFR-driven glucose metabolism primes the apoptotic machinery, resulting in synergy with pro-apoptotic stimuli such as p53 activation. A logical prediction of this model is that direct targeting of glucose metabolism should phenocopy the effects of EGFR inhibition. Consistent with this, addition of the glucose metabolic inhibitor 2-deoxyglucose (2DG) stimulated apoptotic priming, binding of p53 to Bcl-xL, and synthetic lethality with nutlin in HK301 metabolic responder cells. (**Supplementary Fig. 9a, b, d**).

In contrast, inhibition of oxidative phosphorylation with oligomycin (complex V/ATP synthase) or rotenone (complex I) did not synergize with nutlin treatment in HK301 gliomaspheres (**Supplementary Fig. 9c, d**). Thus, reduced glucose metabolic flux alone, but not oxidative metabolism, appears to be sufficient for synergistic sensitivity to p53 activation.

This prompted us to consider whether modulating glucose consumption in non-responders results in a similar p53-dependent vulnerability. To investigate this, we tested whether direct inhibition of glucose uptake, with 2DG, or through targeting PI3K – a well characterized driver of glucose metabolism[36] - elicits apoptotic priming in two erlotinib metabolic non-responders (**Fig. 5a**). In contrast to erlotinib treatment, acute inhibition of PI3K with pictilisib abrogated PI3K-AKT-mTOR signaling (**Supplementary Fig. 9e**), and significantly reduced ^{18}F-FDG uptake in HK393 and HK254 cells (**Fig. 5b**). The decrease in glucose consumption with pictilisib was associated with significantly higher apoptotic priming; 2DG treatment induced similar effects (**Fig. 5b, c**). Therefore, erlotinib metabolic non-responders can be primed for apoptosis following inhibition of glucose uptake. Importantly, CRISPR/CAS-9 targeting of p53 in HK393 cells significantly suppressed priming mediated by 2DG or pictilisib. (**Fig. 5d**). Moreover, p53-dependent priming was associated with heightened Bcl-xL and p53 binding, indicative of sequestration of p53 by Bcl-xL to block apoptosis (**Fig. 5e and Supplementary Fig. 9f**). In agreement with this interpretation, combining 2DG or pictilisib with nutlin caused significant, p53-dependent synthetic lethality in erlotinib non-responder cells (**Fig. 5f, g**). Taken together, these data demonstrate that acute inhibition of glucose metabolism, either directly or with targeted therapy, promotes p53-dependent apoptotic priming in GBM which creates a targetable vulnerability.

A non-invasive biomarker for combination treatment *in vivo*

Our results in cell culture show that combined targeting of oncogene-driven glucose metabolism and p53 has synergistic activity in primary GBM. This led us to investigate whether this approach

could be effective in orthotopic GBM xenograft models. For these studies, we used the MDM2 inhibitor, Idasanutlin, which is currently in clinical trials for many malignancies[37]. Given the uncertainty of CNS penetration of Idasanutlin, we first demonstrated that Idasanutlin can accumulate in the brains of mice with a completely intact blood-brain-barrier (~35% relative to plasma levels) and stabilizes p53 in orthotopic tumor-bearing mice (**Supplementary Fig. 10a, b**).

Next, as perturbations in glucose metabolism with oncogene inhibition are required for synergistic sensitivity to p53 activation, we hypothesized that rapid attenuation in glucose uptake *in vivo* following erlotinib administration – as measured by ^{18}F-FDG PET – could serve as a non-invasive predictive biomarker for therapeutic efficacy of combined erlotinib and Idasanutlin treatment (**Fig. 6a**). We observed, in orthotopic xenografts of a metabolic responder gliomasphere (GBM39), that acute erlotinib treatment (75 mg/kg) rapidly reduced ^{18}F-FDG uptake (15 hours post erlotinib administration, see Materials and Methods) (**Fig. 6b and Supplementary Fig. 10c**). In separate groups of mice, we tested the individual drugs and the combination of daily erlotinib (75 mg/kg) and Idasanutlin (50 mg/kg) treatment for up to 25 days. The drug combination was tolerable over the treatment period; we noted a ~10% decrease in body weight, which was comparable to erlotinib treatment alone (**Supplementary Fig. 10d**). Relative to single agent controls, combined erlotinib and Idasanutlin demonstrated synergistic growth inhibition – as determined by secreted *gaussia* luciferase[38] - in GBM39 intracranial tumor-bearing mice (**Fig. 6c and**). In contrast, orthotopic xenografts of a non-metabolic responder (HK393) showed no changes in ^{18}F-FDG uptake with acute erlotinib (**Fig. 6d and Supplementary Fig. 10c**), nor synergistic activity with the erlotinib and Idasanutlin combination (**Fig. 6e**). Thus, non-invasive ^{18}F-FDG PET, used to measure rapid changes in glucose uptake with EGFR inhibition, was effective in predicting subsequent synergistic sensitivity to combined erlotinib and Idasanutlin

Finally, we evaluated the effects of the drug combination on overall survival in orthotopic xenografts of either two erlotinib metabolic responders (GBM39 and HK336) or two non-responders (HK393 and GS025). All tumors were p53 wild-type (**Supplemental Fig. 3a**). Following evidence of tumor growth (as determined by *gaussia* luciferase), mice were treated with vehicle, erlotinib, Idasanutlin, or the combination for up to 25 days and then release of therapy; the short-term treatment due to limited quantities of Idasanutlin for these studies. Despite all tumors having genetic alterations in *EGFR* (e.g., mutation and/or amplification, polysomy), the drug combination led to a pronounced increase in survival only in animals bearing erlotinib metabolic responder GBM tumors (**Fig. 6f-i**). Taken together, these data show that combined targeting of EGFR and p53 synergistically inhibits growth and prolongs survival in a subset of p53 wild-type GBM orthotopic xenografts, and that ^{18}F-FDG PET is a non-invasive predictive biomarker of sensitivity to this new combination therapeutic strategy.

DISCUSSION

Here we found that acute EGFR inhibition rapidly reduces glucose utilization in a subset of patient-derived GBMs. As a consequence to this altered metabolic state, unexpectedly, cells become primed for apoptosis via the cytoplasmic functions of p53. Accordingly, pharmacological p53 stabilization – with a novel brain-penetrant small molecule - was synthetically lethal with inhibition of EGFR-driven glucose uptake in primary orthotopic GBM models. While these preclinical systems do not fully recapitulate the features of human GBM - consisting of an active immune system, pseudopalisading necrosis, and microvasculature proliferation - our results provide a proof of concept that deploying targeted agents to perturb and exploit altered tumor metabolism could be an effective therapeutic strategy in GBM.

The majority of studies suggest that the apoptotic functions of p53 are primarily exerted through its transcriptional activity. However, recent work supports the suggestion that the non-

transcriptional functions of p53 can have a critical role in triggering intrinsic apoptosis[26]. Our results provide, to the best of our knowledge, the first demonstration that cytoplasmic p53 couples oncogenic signaling to intrinsic apoptosis; which in this case is dependent on alterations in glucose utilization. However, it is remains unknown the metabolic pathway(s) downstream of glucose uptake that is responsible for this effect. The observation that direct inhibition of oxidative phosphorylation does not synergize with p53 activation suggests that oxidation of glucose or other metabolites (e.g., glutamine) is not required (**Supplementary Fig. 9c, d**). Glucose can feed into many metabolic pathways including those for anabolic processes (e.g., lipids, nucleotides, amino acids), energetics, and enzyme function (e.g., glycosylation, acetylation). Thus, attenuated glucose consumption may affect multiple pathways to induce sufficient metabolic stress[39] and/or reduced donor metabolic substrates[40,41] to stimulate the cytoplasmic functions of p53. Future studies are required to specifically define these metabolic nodes that render GBM cells exquisitely susceptible to cytoplasmic p53-mediated apoptosis. This could reveal analogous therapeutic vulnerabilities to exploit GBM tumors for p53-dependent cell death.

More work is also needed to understand precisely how cytoplasmic p53 triggers intrinsic apoptosis in GBM cells. Considerable evidence indicates that cytoplasmic p53 possesses similar functionality as pro-apoptotic BH3 proteins, where it can activate the pro-apoptotic effectors BAK[22,42] or BAX directly[21] and/or indirectly via neutralizing anti-apoptotic Bcl2 proteins[22]. Our results support this role for cytoplasmic p53 whereby, following attenuated glucose metabolism, p53 engages the intrinsic apoptotic machinery via binding to the anti-apoptotic protein Bcl-xL. Despite minimal cell death, the increased occupancy of Bcl-xL with p53 lowers the apoptotic threshold and creates a dependency on Bcl-xL to block p53-mediated cell death. Targeting this interaction (e.g., BCL-xL inhibition or MDM2 antagonism) liberated p53 from Bcl-xL which coincided with BAX activation and cytoplasmic p53-dependent intrinsic apoptosis. This raises the possibility that “free” cytoplasmic p53 is directly activating BAX to promote apoptosis in response

to this therapeutic combination. Finally, it is important to note that while cytoplasmic p53 was necessary for the execution of synergistic apoptosis with either Bcl-xL or MDM2 inhibition, it was universally sufficient only in the context of Bcl-xL inhibition (**Supplemental Fig. 7c and Supplemental Fig. 8g**). This apparent discrepancy may be explained through observations that, in some instances, the displacement of cytoplasmic p53 from Bcl-xL requires the binding of the p53 transcriptional target gene PUMA[27,43]. As MDM2 antagonists can stimulate nuclear p53 transcriptional activity, including expression of PUMA, it possible that in some contexts the transcription-dependent functions of p53 are required to facilitate cytoplasmic p53-mediated apoptosis in GBM.

It is noteworthy that neither genetic alterations in *EGFR* nor inhibition of EGFR activity were sufficient to predict a metabolic response with EGFR TKI in our GBM samples. Several molecular mechanisms have been described that can enable dynamic compensatory responses to EGFR-directed therapy in GBM[44]. Thus, it is likely that, despite robust inhibition of EGFR, some tumors quickly rewire their molecular circuitry to preserve downstream signaling flux and drive glucose consumption[45]. Given the breadth of potential adaptive mechanisms, coupled with the molecular heterogeneity of GBM, genetic biomarkers may alone be insufficient to predict responses to this approach. Our results emphasize the value of a functional biomarker, in this case changes in glucose uptake[46], as a means to rapidly stratify metabolic responders and non-responders.

Taken together, our findings provide rationale for the clinical evaluation of combined targeting of oncogene-driven glucose metabolism (e.g., EGFRi or PI3Ki) and p53 in GBM patients. Furthermore, we propose a new clinical application of ^{18}F-FDG PET to assess whether targeted drugs have induced a metabolic vulnerability that can be exploited. As we show that changes in ^{18}F-FDG accumulation can be observed within hours of EGFR inhibitor treatment, ^{18}F-FDG PET could serve as a rapid, non-invasive functional biomarker to predict synergistic sensitivity to p53 activation. This non-invasive analysis could be particularly valuable for malignant brain tumors,

where pharmacokinetic/pharmacodynamic assessment is extremely difficult and impractical. While there are concerns that ^{18}F-FDG PET cannot properly delineate tumor glucose uptake versus healthy brain tissue glucose uptake, delayed imaging protocols[47] (used here for the mouse studies) and parametric response maps (PRMs) with MRI fusion can be useful for quantifying the changes in tumor ^{18}F-FDG consumption. Lastly, targeting oncogenes that drive glucose uptake in other cancers may evoke similar p53-dependent vulnerabilities. Future work is required to assess the applicability of this concept to other oncogenic drivers and cancers.

ONLINE METHODS

Mice. Female NOD *scid* gamma (NSG), 6-8 weeks of age, were purchased from the University of California Los Angeles (UCLA) medical center animal breeding facility. Male CD-1 mice, 6-8 weeks of age, were purchased from Charles River. All mice were kept under defined flora pathogen-free conditions at the AAALAC-approved animal facility of the Division of Laboratory Animals (DLAM) at UCLA. All animal experiments were performed with the approval of the UCLA Office of Animal Resource Oversight (OARO).

Patient-derived GBM cells. All patient tissue to derive GBM cell cultures was obtained through explicit informed consent, using the UCLA Institutional Review Board (IRB) protocol: 10-000655. As previously described[12], primary GBM cells were established and maintained in gliomasphere conditions consisting of DMEM/F12 (Gibco), B27 (Invitrogen), Penicillin-Streptomycin (Invitrogen), and Glutamax (Invitrogen) supplemented with Heparin (5 μg/mL, Sigma), EGF (50 ng/mL, Sigma), and FGF (20 ng/mL, Sigma). All cells were grown at 37°C, 20% O_2, and 5% CO_2 and were routinely monitored and tested negative for the presence of mycoplasma using a commercially available kit (MycoAlert, Lonza). At the time of experiments, most HK lines used were between 20-30 passages (exceptions HK385 p8, HK336 p15), while GS and GBM39 lines were less than 10 passages. All cells were authenticated by short-tandem repeat (STR) analysis.

Reagents and antibodies. Chemical inhibitors from the following sources were dissolved in DMSO for *in vitro* studies: Erlotinib (Chemietek), Nutlin-3A (Selleck Chemicals), WEHI-539 (APExBIO), Pictilisib (Selleck Chemicals), Oligomycin (Sigma), Rotenone (Sigma). 2DG (Sigma) was dissolved freshly in media prior to usage. Antibodies used for immunoblotting were obtained from the listed sources: β-actin (8H10D10) Mouse mAb (Cell signaling, 3700), tubulin (DM1A)

Mouse mAb (Cell signaling, 3873), p-EGFR Y1086 (2533287) Rabbit pAb (Thermo Fischer Scientific, 36-9700), t-EGFR Rabbit pAb (Millipore, 06-847), t-AKT (11E7) Rabbit mAb (Cell Signaling, 4685), p-AKT T308 (D25E6) Rabbit mAb (Cell Signaling, 13038), p-AKT S473 (D9E) Rabbit mAb (Cell Signaling, 4060), t-ERK (137F5) Rabbit mAb (Cell Signaling, 4695), p-ERK T202/Y204 (D13.14.4E) Rabbit mAb (Cell Signaling, 4370), t-S6 (5G10) Rabbit mAb (Cell Signaling, 2217), p-S6 S235/236 (D57.2.2E) Rabbit mAb (Cell Signaling, 4858), t-4EBP1 (53H11) Rabbit mAb (Cell Signaling, 9644), p-4EBP1 S65 Rabbit pAb (Cell Signaling 9451), Glut3 Rabbit pAb (Abcam, ab15311), Glut1 Rabbit pAb (Millipore, 07-1401), p53 (DO-1) Mouse mAb (Santa Cruz Biotechnology, SC-126), BAX (D2E11) Rabbit mAb (Cell Signaling, 5023), BIM (C34C5) Rabbit mAb (Cell Signaling, 2933), PUMA (D30C10) Rabbit mAb (Cell Signaling, 12450), Bcl-2 (50E3) Rabbit mAb (Cell Signaling, 2870), Bcl-xL (54H6) Rabbit mAb (Cell Signaling, 2764), Mcl-1 (D35A5) Rabbit mAb (Cell Signaling, 5453), Cytochrome c Rabbit pAb (Cell Signaling, 4272), and Cleaved Caspase-3 Rabbit pAb (Cell Signaling, 9661). Antibodies used for immunoprecipitation were obtained from the listed sources: p53 Rabbit pAb (Cell Signaling, 9282). Secondary antibodies were obtained from the listed sources: Anti-rabbit IgG HRP-linked (Cell Signaling, 7074) and Anti-mouse IgG HRP-linked (Cell Signaling, 7076). All immunoblotting antibodies were used at a dilution of 1:1000, except β-actin and tubulin, which were used at 1:10,000. Immunoprecipitation antibodies were diluted according to manufacturer's instructions (1:200 for p53). Secondary antibodies were used at a dilution of 1:5000.

^{18}F-Fluorodeoxyglucose (^{18}F-FDG) uptake assay. Cells were plated at 5 × 10^4 cells/ml and treated with designated drugs for indicated time points. Following appropriate treatment, cells were collected and resuspended in glucose-free DMEM/F12 (US Biological) containing ^{18}F-FDG (radioactivity 1 μCi/mL). Cells were incubated at 37°C for 1 hr and then washed three times with ice cold PBS. Radioactivity of each sample was then measured using a gamma counter.

Glucose, glutamine, and lactate measurements. Cellular glucose consumption and lactate production were measured using a Nova Biomedical BioProfile Basic Analyzer. Briefly, cells were plated in 1 x 10^5 cells/ml in 2 mL of gliomasphere conditions and appropriate drug conditions. 12 hrs following drug treatment, 1 ml of media was removed from each sample and analyzed in the Nova BioProfile analyzer. Measurements were normalized to cell number.

Annexin V apoptosis assay. Cells were collected and analyzed for Annexin V and PI staining according to manufacturer's protocol (BD Biosciences). Briefly, cells were plated at 5 x 10^4 cells/ml and treated with appropriate drugs. Following indicated time points, cells were collected, trypsinized, washed with PBS, and stained with Annexin V and PI for 15 minutes. Samples were then analyzed using the BD LSRII flow cytometer.

Immunoblotting. Cells were collected and lysed in RIPA buffer (Boston BioProducts) containing Halt Protease and Phosphatase Inhibitor (Thermo Fischer Scientific). Lysates were centrifuged at 14,000xg for 15min at 4°C. Protein samples were then boiled in NuPAGE LDS Sample Buffer (Invitrogen) and NuPAGE Sample Reducing Agent (Invitrogen) and separated using SDS-PAGE on 12% Bis-Tris gels (Invitrogen) and transferred to nitrocellulose membrane (GE Healthcare). Immunoblotting was performed per antibody's manufacturer's specifications and as mentioned previously. Membranes were developed using the SuperSignal system (Thermo Fischer Scientific).

Immunoprecipitation. Cells were collected, washed once with PBS, and incubated in IP lysis buffer (25 mM Tris-HCL pH 7.4, 150 mM NaCl, 1 mM EDTA, 1% NP-40, 5% Glycerol) at 4°C for 15 minutes. 300-500 µg of each sample was then pre-cleared in Protein A/G Plus Agarose Beads (Thermo Fischer Scientific) for one hour. Following pre-clear, samples were then incubated with antibody-bead conjugates overnight according to manufacturer's specifications and as mentioned previously. The samples were then centrifuged at 1000g for 1 min, and the beads were washed with 500 µL of IP lysis buffer for five times. Proteins were eluted from the beads by boiling in 2x LDS Sample Buffer (Invitrogen) at 95°C for 5 min. Samples analyzed by immunoblotting as previously described. Immunoprecipitation antibodies were diluted according to manufacturer's instructions (1:200 for p53 and 1:100 for Bcl-xL).

Dynamic BH3 profiling. GBM gliomaspheres were first disassociated to single-cell suspensions with TrypLE (Gibco) and resuspended in MEB buffer (150 mM Mannitol 10 mM HEPES-KOH, 50 mM KCl, 0.02 mM EGTA, 0.02 mM EDTA, 0.1 % BSA, 5 mM Succinate). 50µl of cell suspension (3×10^4 cells/well) were plated in wells holding 50 µL MEB buffer containing 0.002% digitonin and indicated peptides in 96-well plates. Plates were then incubated at 25°C for 50 min. Cells were then fixed with 4% paraformaldehyde for 10min, followed by neutralization with N2 buffer (1.7M Tris, 1.25M Glycine pH 9.1) for 5min. Samples were stained overnight with 20 µL of staining solution (10% BSA, 2% Tween 20 in PBS) containing DAPI and anti-cytochrome *c* (BioLegend). The following day, cytochrome *c* release was quantified using BD LSRII flow cytometer. Measurements were normalized to appropriate controls that do not promote cytochrome *c* release (DMSO and inactive PUMA2A peptide). Delta priming refers to the difference in amount of cytochrome *c* release between vehicle treated cells and drug treated cells.

Plasma membrane protein extraction: 1 × 10^7 cells were treated with indicated drugs. Following 4hr of treatment, cells were collected, washed once with ice cold PBS, and lysed using a Dounce Homogenizer. Plasma membrane protein extraction proceeded following manufacturer's protocol (BioVision), and isolated proteins were then subject to immunoblotting.

BAX oligomerization. 7.5 x 10^5 cells were treated with indicated drugs. Following 24 hr of treatment, cells were collected, washed once with ice cold PBS, and re-suspended in 1 mM bismaleimidohexane (BMH) in PBS for 30 min. Cells were then pelleted and lysed for immunoblotting, as described above.

Cytochrome *c* detection. 5 million cells were plated at a concentration of 1x10^5 cells/mL and treated with indicated drugs. Following 24 hr of treatment, cells were collected, washed once with ice cold PBS. Subcellular fractionation was then performed using a mitochondrial isolation kit (Thermo Fischer Scientific, 89874). Both cytoplasmic and mitochondrial fractions were subjected to immunoblotting and cytochrome *c* was detected using cytochrome *c* antibody at a dilution of 1:1000 (Cell Signaling, 4272).

Mouse xenograft studies. For intracranial experiments, GBM39, HK336, HK393, and GS025 cells were injected (4 × 10^5 cells per injection) into the right striatum of the brain of female NSG mice (6-8 weeks old). Injection coordinates were 2 mm lateral and 1 mm posterior to bregma, at a depth of 2 mm. Tumor burden was monitored by secreted *gaussia* luciferase and following three consecutive growth measurements, mice were randomized into four treatment arms consisting of appropriate vehicles, 75 mg/kg erlotinib, 50 mg/kg Idasanutlin, or a combination of both drugs. Vehicle consisted of 0.5% methylcellulose in water, which is used to dissolve erlotinib, and a

proprietary formulation obtained from Roche, which is used to dissolve Idasanutlin. Tumor burden was assessed twice per week by secreted *gaussia* luciferase. When possible, mice were treated for 25 days and taken off treatment and monitored for survival. Drugs were administered through oral gavage. Sample sizes were chosen based off estimates from pilot experiments and results from previous literature[12]. Investigators were not blinded to group allocation or assessment of outcome. All studies were in accordance with UCLA OARO protocol guidelines.

Intracranial delayed PET/CT mouse imaging. For baseline ^{18}F-FDG scans, mice were treated with vehicle and 15 hours later were pre-warmed, anesthetized with 2% isoflurane, and intravenously injected with 70 µCi of ^{18}F-FDG. Following 1hr unconscious uptake, mice were taken off anesthesia but kept warm for another 5 hr of uptake. 6 hr after the initial administration of ^{18}F-FDG, mice were imaged using G8 PET/CT scanner (Sofie Biosciences). Following imaging, all mice were then dosed with erlotinib (75 mg/kg) and 15 hours later went through the same imaging procedure. Per above, quantification was performed by drawing 3D regions of interest (ROI) using the AMIDE software as previously described[48]. Note, the 15 hour treatment time point was the earliest time point that fit within the logistical constraints; this includes half-lives required for adequate probe decay for subsequent imaging, ^{18}F-FDG production schedule and imaging center hours.

Immunohistochemistry. Immunohistochemistry was performed on 4 µm sections that were cut from FFPE (formalin-fixed, paraffin-embedded) blocks. Sections were then deparaffinised with xylene and rehydrated through graded ethanol. Antigen retrieval was achieved with a pH 9.5 Nuclear Decloaker (Biocare Medical) in a Decloaking pressure cooker at 95°C for 40 min. Tissue sections were then treated with 3% hydrogen peroxide (LOT 161509; Fisher Chemical) and with

Background Sniper (Biocare Medical, Concord, CA, USA) to reduce nonspecific background staining. Primary antibody for p53 (Cell Signaling, 2527) was applied in a 1:150 dilution for 80 min followed by detection with the MACH 3 Rabbit HRP- Polymer Detection kit (Biocare Medical). Visualization was achieved using VECTOR NovaRED (SK-4800; Vector Laboratories, Inc.) as chromogen. Lastly, sections were counterstained with Tacha's Automated Hematoxylin (Biocare Medical).

Quantitative RT-PCR. RNA was extracted from all cells using Purelink RNA Kit (Invitrogen). cDNA was synthesized with iScript cDNA Synthesis Kit (Bio-Rad) as per manufacturer's instructions. Quantitative PCR (qPCR) was conducted on the Roche LightCycler 480 using SYBRGreen Master Mix (Kapa Biosciences). Relative expression values are normalized to control gene (*GAPDH*). Primer sequences are as listed (5' to 3'): *P21* (forward GACTTTGTCACCGAGACACC, reverse GACAGGTCCACATGGTCTTC), *PUMA (*forward ACGACCTCAACGCACAGTACG, reverse GTAAGGGCAGGAGTCCCATGATG), *GAPDH* (forward TGCCATGTAGACCCCTTGAAG, reverse ATGGTACATGACAAGGTGCGG), *MDM2* (forward CTGTGTTCAGTGGCGATTGG, reverse AGGGTCTCTTGTTCCGAAGC), *TIGAR* (forward GGAAGAGTGCCCTGTGTTTAC, reverse GACTCAAGACTTCGGGAAAGG), *PIG3* (forward GCAGCTGCTGGATTCAATTA, reverse TCCCAGTAGGATCCGCCTAT)

P53 reporter activity. Cells were first infected with lentivirus synthesized from a p53 reporter plasmid which codes for luciferase under the control of a p53 responsive element: TACAGAACATGTCTAAGCATGCTGTGCCTTGCCTGGACTTGCCTGGCCTTGCCTTGGG. Infected cells were then plated into a 96-well plate at 5,000 cells/ 50 µL and treated with indicated

drugs for 24 hr and then incubated with 1 mM D-luciferin for two hours. Bioluminescence was measured using IVIS Lumina II (Perkin Elmer).

Genetic manipulation. In general, lentivirus used for genetic manipulation were produced by transfecting 293-FT cells (Thermo) using Lipofectamine 2000 (Invitrogen). Virus was collected 48 hours after transfection. The lentiviral sgp53 vector and sgControl vector contained the following guide RNA, respectively: CCGGTTCATGCCGCCCATGC and GTAATCCTAGCACTTTTAGG. LentiCRISPR-v2 was used as the backbone. Glut1 and Glut3 cDNA was cloned from commercially available vectors and incorporated into pLenti-GLuc-IRES-EGFP lentiviral backbone containing a CMV promoter (Glut1 was a gift from Wolf Frommer (Addgene #18085[49]), Glut3 was obtained from OriGene #SC115791, and the lentiviral backbone was obtained from Targeting Systems #GL-GFP). pMIG Bcl-xL was a gift from Stanley Korsmeyer (Addgene #8790[50]) and cloned into the lentiviral backbone mentioned above (Targeting Systems). Cytoplasmic (K305A and R306A) and wild-type p53 constructs were a kind gift from R. Agami and G. Lahav. The genes of interest were cloned into a lentiviral vector containing a PGK promoter. Constructs for p53 DNA binding domain mutants (R175H) and (R273H) as well as the nuclear mutant (L348A and L350A) were generated using site-directed mutagenesis (New England Biolabs #E0554S) on the wild-type p53 construct.

For EGFR knockdown experiments, siRNA against EGFR (Thermo Fischer Scientific, s563) was transfected into cells using DharmaFECT 4 (Dharmacon). Following 48 hours, cells were harvested and used for indicated experiments.

Immunofluorescence. For immunofluorescence, gliomaspheres were first disassociated to single cell and adhered to the 96-well plates using Cell-Tak (Corning) according to manufacturer

instructions. Adhered cells were then fixed with ice-cold methanol for 10 min then washed three times with PBS. Cells were then incubated with blocking solution containing 10% FBS and 3% BSA in PBS for 1 hr and subsequently incubated with p53 (Santa Cruz, SC-126, dilution of 1:50) antibody overnight at 4°C. The following day, cells were incubated with secondary antibody (Alexa Fluor 647, dilution 1:2000) for an hour and DAPI staining for 10 min, then imaged using a Nikon TI Eclipse microscope equipped with a Cascade II fluorescent camera (Roper Scientific). Cells were imaged with emissions at 461 nM and 647 nM and then processed using NIS-Elements AR analysis software.

Oxygen consumption rate (OCR) and extracellular acidification rate (ECAR) measurements. For metabolic measurements involving OCR and ECAR, gliomaspheres treated with indicated drugs were first disassociated to single-cell suspensions and adhered to XF24 plates (Seahorse Bioscience) using Cell-Tak (Corning) according to manufacturer instructions. Prior to the assay, cells were supplemented with unbuffered DMEM, and incubated at 37°C for 30 min before starting OCR and ECAR measurements. Basal ECAR measurements between control and erlotinib treated cells are shown.

Mass-spectroscopy sample preparation. Male CD-1 mice (6-8 weeks old) were treated with 50 mg/kg Idasanutlin in duplicate through oral gavage. At 0.5, 1, 2, 4, 6, 8, 12, and 24 hr after administration, mice were sacrificed, blood was harvested by retro-orbital bleeding, and brain tissue was collected. Whole blood from mice was centrifuged to isolate plasma. Idasanutlin was isolated by liquid-liquid extraction from plasma: 50 µL plasma was added to 2 µL internal standard and 100 µL acetonitrile. Mouse brain tissue was washed with 2 mL cold PBS and homogenized using a tissue homogenizer with fresh 2 mL cold PBS. Idasanutlin was then isolated and

reconstituted in a similar manner by liquid-liquid extraction: 100 µL brain homogenate was added to 2 µL internal standard and 200 µL acetonitrile. After vortex mixing, the samples was centrifuged. The supernatant was removed and evaporated by a rotary evaporator and reconstituted in 100 µL 50:50 water: acetonitrile.

Idasanutlin detection by mass-spectrometry. Chromatographic separations were performed on a 100 x 2.1 mm Phenomenex Kinetex C18 column (Kinetex) using the 1290 Infinity LC system (Agilent). The mobile phase was composed of solvent A: 0.1% formic acid in Milli-Q water, and B: 0.1% formic acid in acetonitrile. Analytes were eluted with a gradient of 5% B (0-4 min), 5-99% B (4-32 min), 99% B (32-36 min), and then returned to 5% B for 12 min to re-equilibrate between injections. Injections of 20 µL into the chromatographic system were used with a solvent flow rate of 0.10 mL/min. Mass spectrometry was performed on the 6460 triple quadrupole LC/MS system (Agilent). Ionization was achieved by using electrospray in the positive mode and data acquisition was made in multiple reactions monitoring (MRM) mode. The MRM transition used for Idasanutlin detection was m/z 616.2 → 421.2 with fragmentor voltage of 114V, and collision energy of 20 eV. Analyte signal was normalized to the internal standard and concentrations were determined by comparison to the calibration curve (0.5, 5, 50, 250, 500, 2000 nM). Idasanutlin brain concentrations were adjusted by 1.4% of the mouse brain weight for the residual blood in the brain vasculature as described by Dai et al [51].

Secreted *gaussia* luciferase measurements. Cells were infected with a lentiviral vector containing secreted *gaussia* luciferase (sGluc) reporter gene (Targeting Systems # GL-GFP) and intracranially implanted into the right striatum of mice (4 x 10^5 cells/mouse). To measure the levels of secreted Gaussia luciferase (sGluc), 6 µL of blood was collected from the tail vein of the mice

and immediately mixed with 50 mM EDTA to prevent coagulation. Gluc activity was obtained by measuring chemiluminescence following injection of 100 µL of 100 µM coelentarazine (Nanolight) in a 96 well plate as described before.[38]

Synergy score calculations. 1.0 x 10^5 GBM cells were plated in triplicate and treated with erlotinib, nutlin, or combination at multiple concentrations using a matrix where each drug was added to the cells at six concentrations (0-10 µM). Annexin V staining was measured following 72 hrs of treatment. Using the Chalice software, as described in Lehar et al., the response of the combination was compared to its single agents, and the combinatorial effects were calculated using the synergy score[33].

DNA sequencing. Targeted sequencing was performed for samples HK206, HK217, HK250, HK296 for the following genes *BCL11A, BCL11B, BRAF, CDKN2A, CHEK2, EGFR, ERBB2, IDH1, IDH2, MSH6, NF1, PIK3CA, PIK3R1, PTEN, RB1, TP53* using Illumina Miseq. There were 1 to 2 million reads per sample with average coverage of 230 per gene. Copy number variants were determined for these samples using a whole genome SNP array. The genetic profile of GBM39 has been previously reported[45].

Whole exome sequencing was performed for samples HK157, HK229, HK248, HK250, HK254, HK296, HK301, HK336, HK350, HK390, HK393 and carried out at SeqWright. Samples were grouped into 2 pools with separate capture reactions. Nextera Rapid capture and library preparation were used and sequencing performed on a HiSeq 2500, 2x100 bp with 100x on-target coverage, 2 full rapid runs, each with 1 normal diploid control. Copy number analysis for these samples was carried out using EXCAVATOR software: http://genomebiology.com/content/pdf/gb-2013-14-10-r120.pdf

Data-availability statement. Data presented in this manuscript are available from the corresponding authors upon request.

Annotation of TCGA samples. 273 GBM samples from the TCGA were analyzed for genetic alterations in EGFR, p53 and p53-regulated pathways. Co-occurrences of mutations were examined and only significant interactions are displayed. Data was analyzed using cBioPortal as previously described [52,53].

Fluorescence *in situ* Hybridization (FISH). Fluorescence in situ hybridization (FISH) was performed using commercially available fluorescently labeled dual-color EGFR (red)/CEP 7(green) probe (Abbott-Molecular). FISH hybridization and analyses were performed on cell lines, following the manufacturer's suggested protocols. The cells were counterstained with DAPI and the fluorescent probe signals were imaged under a Zeiss (Axiophot) Fluorescent Microscope equipped with dual- and triple-color filters.

Statistical analysis. Comparisons were made using two-tailed unpaired Student's *t*-tests and *p* values <0.05 were considered statistically significant. All data from multiple independent experiments were assumed to be of normal variance. For each experiment, replicates are as noted in the figure legends. Data represent mean ± s.d. values unless otherwise indicated. All statistical analyses were calculated using Prism 7.0 (GraphPad). For all *in vitro* and *in vivo* experiments, no statistical method was used to predetermine sample size and no samples were

excluded. For *in vivo* tumor measurements, the last data sets were used for comparisons between groups. As described above, all mice were randomized before studies.

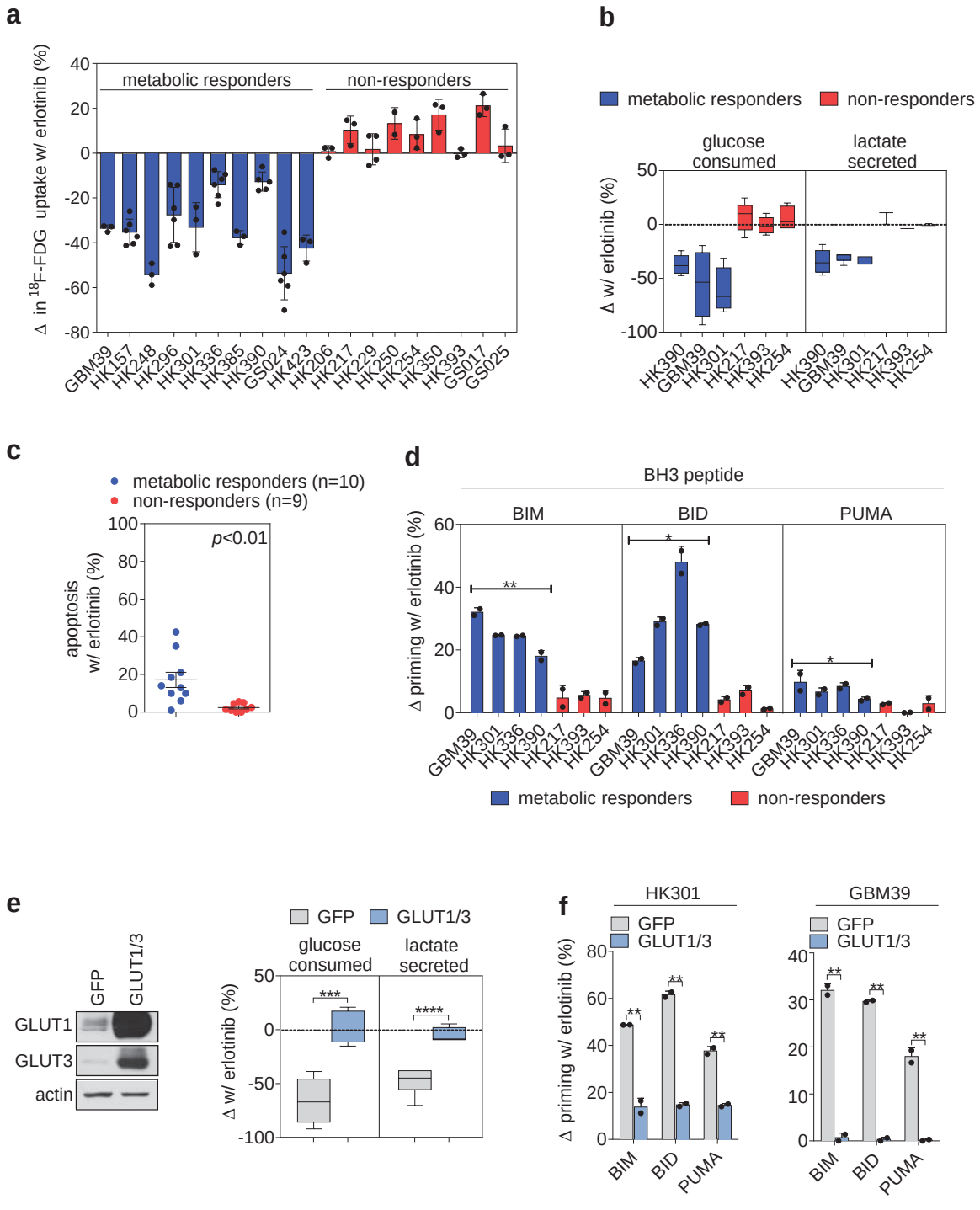
a
Δ in 18F-FDG uptake w/ erlotinib (%)
metabolic responders
non-responders
GBM39 HK157 HK248 HK296 HK301 HK336 HK385 HK390 GS024 HK423 HK206 HK217 HK229 HK250 HK254 HK350 HK393 GS017 GS025
b
metabolic responders
non-responders
glucose consumed
lactate secreted
Δ w/ erlotinib (%)
HK390 GBM39 HK301 HK217 HK393 HK254
c
metabolic responders (n=10)
non-responders (n=9)
apoptosis w/ erlotinib (%)
p<0.01
d
BH3 peptide
BIM
BID
PUMA
Δ priming w/ erlotinib (%)
GBM39 HK301 HK336 HK390 HK217 HK393 HK254
metabolic responders
non-responders
e
GFP
GLUT1/3
GLUT1
GLUT3
actin
glucose consumed
lactate secreted
Δ w/ erlotinib (%)
f
HK301
GBM39
BIM
BID
PUMA

FIGURE LEGENDS

Figure 1. Inhibition of EGFR-driven glucose metabolism induces minimal cell death but primes GBM cells for apoptosis. (a) Percent change in ^{18}F-FDG uptake after 4 hours of 1 μM erlotinib treatment relative to vehicle in 19 patient-derived GBM gliomaspheres. Concentration of erlotinib was selected to achieve robust inhibition of EGFR activity across our panel of primary GBM cells (see Supplemental Fig. 2). “Metabolic responders” (blue) are samples that show a significant decrease in ^{18}F-FDG uptake relative to vehicle, whereas “non-responders” (red) show no significant decrease (mean ± s.d., $n \geq 3$). **(b)** % change in glucose consumption and lactate secretion with 12 hours of 1 μM erlotinib treatment relative to vehicle. Measurements were made using Nova Biomedical BioProfile Analyzer (mean ± s.d., $n \geq 5$). **(c)** Annexin V staining of metabolic responders (blue, $n = 10$ unique gliomaspheres) or non-responders (red, $n = 9$ unique gliomaspheres) after treatment with 1 μM erlotinib for 72 hours. Each point represents the mean apoptosis of two independent experiments conducted for each gliomasphere sample. See Supplementary Fig. 11 for flow cytometry gating strategy. **(d)** The % change, relative to vehicle control, in priming as determined by cytochrome *c* release following exposure to each BH3 peptide (BIM, BID, or PUMA) in metabolic responders or non-responders treated with 1 μM erlotinib for 24 hours (mean ± s.d., $n = 2$). Statistical analysis was performed on the grouped metabolic responders versus non-responders. Results are representative of two independent experiments **(e)** Left: Immunoblot of whole cell lysate of HK301 cells overexpressing GFP control or GLUT1 and GLUT3 (GLUT1/3). Right: Changes in glucose consumption or lactate secretion of HK301-GFP or HK301-GLUT1/3 after 12 hours of 1 μM erlotinib treatment. Values are relative to vehicle control (mean ± s.d., $n \geq 5$). **(f)** Same as (d) using HK301-GFP or HK301-GLUT1/3 cells (left) or GBM39-GFP or GBM39-GLUT1/3 cells (right). In the box plots, the central rectangle spans the first quartile to the third quartile (the interquartile range or IQR), the central line inside the rectangle shows the mean, and whiskers above and below the box show the locations of the

minimum and maximum within 1.5 IQR of the lower quartile and the upper quartile, respectively. Comparisons were made using two-tailed unpaired Student's *t*-test. *p<0.05, **p<0.01, ***p<0.001, ****p<0.0001.

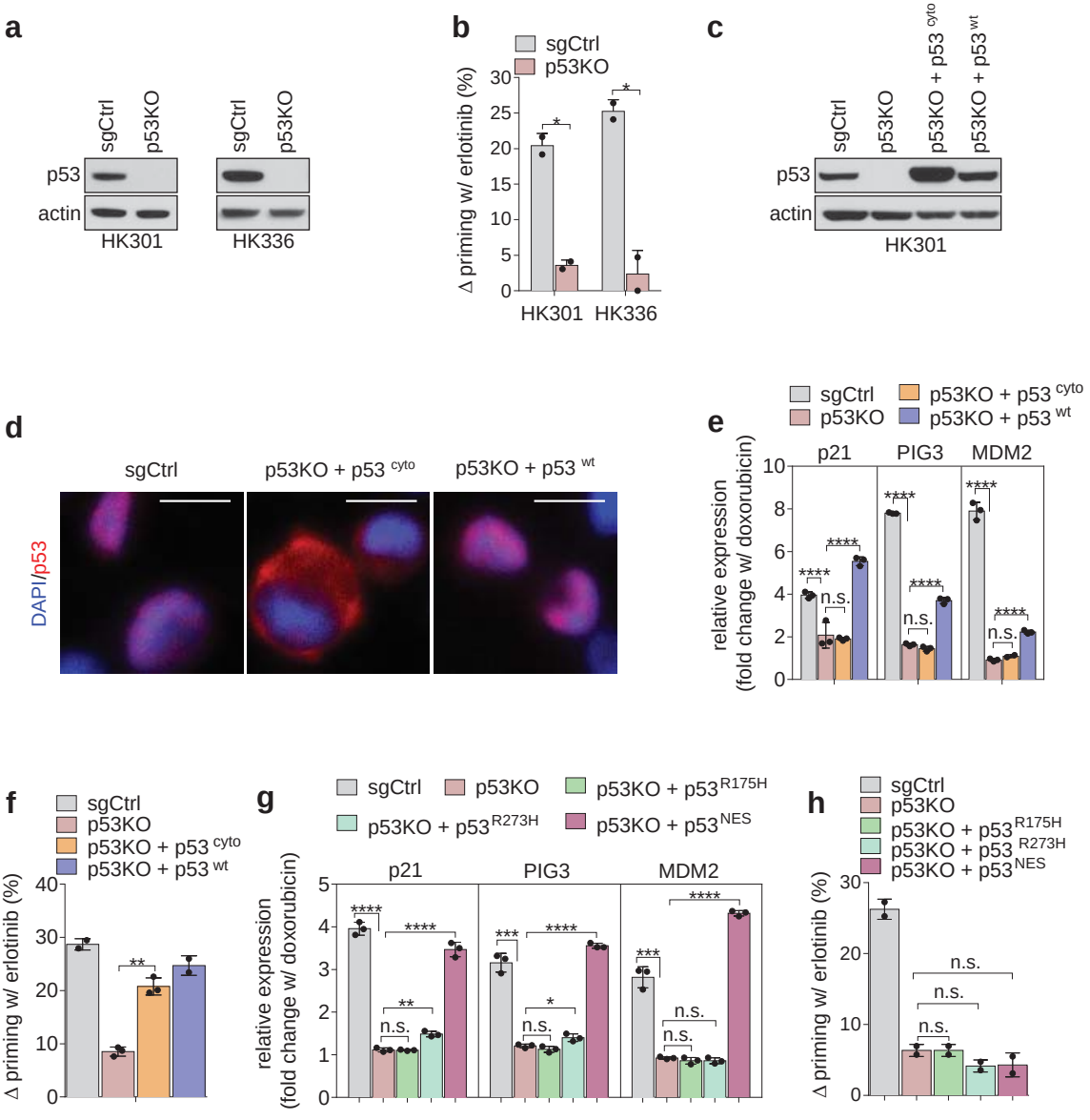
a
sgCtrl
p53KO
p53
actin
HK301
HK336
b
sgCtrl
p53KO
Δ priming w/ erlotinib (%)
HK301
HK336
c
sgCtrl
p53KO
p53KO + p53 cyto
p53KO + p53 wt
p53
actin
HK301
d
sgCtrl
p53KO + p53 cyto
p53KO + p53 wt
DAPI/p53
e
sgCtrl
p53KO
p53KO + p53 cyto
p53KO + p53 wt
p21
PIG3
MDM2
relative expression
(fold change w/ doxorubicin)
n.s.
f
sgCtrl
p53KO
p53KO + p53 cyto
p53KO + p53 wt
Δ priming w/ erlotinib (%)
g
sgCtrl
p53KO
p53KO + p53R175H
p53KO + p53R273H
p53KO + p53NES
p21
PIG3
MDM2
relative expression
(fold change w/ doxorubicin)
n.s.
h
sgCtrl
p53KO
p53KO + p53R175H
p53KO + p53R273H
p53KO + p53NES
Δ priming w/ erlotinib (%)
n.s.

Figure 2. Cytoplasmic p53 links EGFR to intrinsic apoptosis. (a) Immunoblot of indicated proteins in two responders (HK301 and HK336) expressing CRISPR/CAS9 protein with control guide RNA (sgCtrl) or p53 guide RNA (p53KO). **(b)** The % change, relative to vehicle control, in apoptotic priming as determined by cytochrome *c* release following dynamic BH3 profiling with BIM peptides in sgCtrl and p53KO cells treated with 1 μM erlotinib for 24 hours (mean ± s.d., *n* = 2). BIM was selected based on exhibiting the greatest dynamic range from tested synthetic BH3 peptides (Supplemental Fig. 4). Results are representative of two independent experiments. **(c)** Immunoblot of indicated proteins in HK301 sgCtrl, p53KO, p53KO + $p53^{cyto}$, and p53KO + $p53^{wt}$. **(d)** Immunofluorescence of p53 protein combined with DAPI staining to reveal protein localization in HK301 sgCtrl, p53KO + $p53^{cyto}$, and p53KO + $p53^{wt}$ (scale bars = 20 μm). **(e)** Changes in indicated mRNA levels following 100 nM doxorubicin treatment for 24 hours in HK301 sgCtrl, p53KO, p53KO + $p53^{cyto}$, and p53KO + $p53^{wt}$. Levels were normalized to respective DMSO treated cells (mean ± s.d., *n* = 3). **(f)** Same as (b) but in HK301 sgCtrl, p53KO, p53KO + $p53^{cyto}$, and p53KO + $p53^{wt}$ (mean ± s.d., *n* = 2). Results are representative of two independent experiments. **(g)** Same as (e) but in HK301 sgCtrl, p53KO, p53KO + $p53^{R175H}$, p53KO + $p53^{R273H}$, and p53KO + $p53^{NES}$ (mean ± s.d., *n* = 3). **(h)** Same as (b) and (f) but in HK301 sgCtrl, p53KO, p53KO + $p53^{R175H}$, p53KO + $p53^{R273H}$, and p53KO + $p53^{NES}$ (mean ± s.d., *n* = 2). Results are representative of two independent experiments. Comparisons were made using two-tailed unpaired Student's *t*-test. *p<0.05, **p<0.01, ***p<0.001, ****p<0.0001.

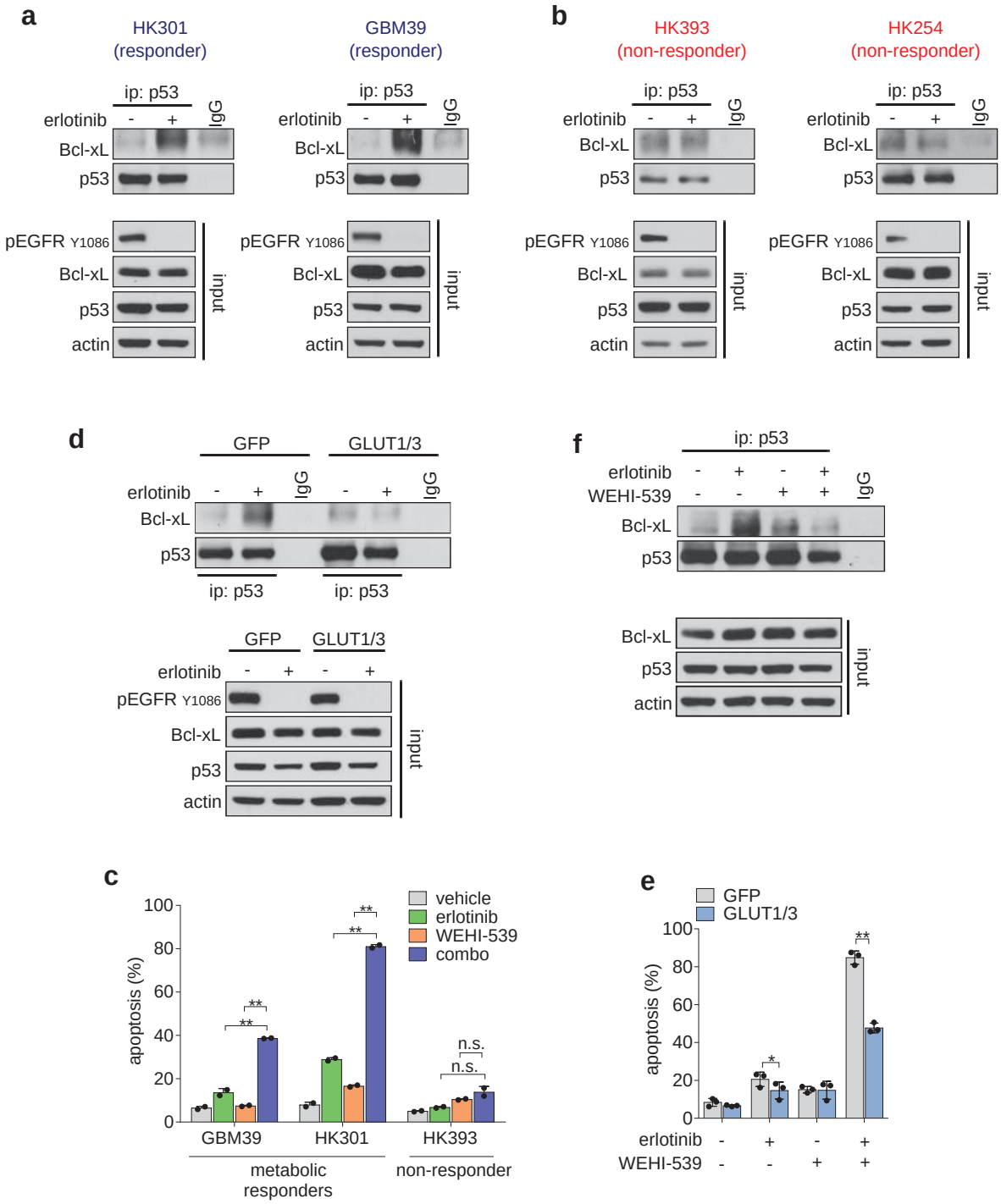
a
HK301
(responder)
GBM39
(responder)
ip: p53
erlotinib
IgG
Bcl-xL
p53
pEGFR Y1086
actin
input
b
HK393
(non-responder)
HK254
(non-responder)
d
GFP
GLUT1/3
c
vehicle
erlotinib
WEHI-539
combo
apoptosis (%)
GBM39
HK301
HK393
metabolic
responders
non-responder
n.s.
e
f
WEHI-539

Figure 3. Bcl-xL prevents GBM cell death by binding to and sequestering cytoplasmic p53. **(a)** Immunoprecipitation of p53 in two metabolic responders (HK301 and GBM39) following 24 hours of 1 μM erlotinib treatment. Immunoprecipitation was performed with immunoglobulin G control antibody or anti-p53 antibody, and the immunoprecipitate was probed with the indicated antibodies. Below are respective pre-immunoprecipitation lysates (input). **(b)** Same as (a) but in two non-responders (HK393 and HK254). **(c)** Same as (a) and (b) but in HK301-GFP and HK301-GLUT1/3. **(d)** HK301 was treated for 24 hours with 1 μM erlotinib, 1 μM WEHI-539, or both and immunoprecipitation and immunoblotting was performed as described previously. **(e)** Annexin V staining of two responders (GBM39 and HK301) and a non-responder (HK393) following 72 hours of treatment with 1 μM erlotinib, 5 μM WEHI-539, or both (mean ± s.d., n = 2). **(f)** Annexin V staining of HK301-GFP and HK301-GLUT1/3 following 72 hours of treatment with 1 μM erlotinib, 5 μM wehi-539, or both (mean ± s.d., n = 2). All results are representative of two individual experiments. Comparisons were made using two-tailed unpaired Student's t-test. *p<0.05, **p<0.01.

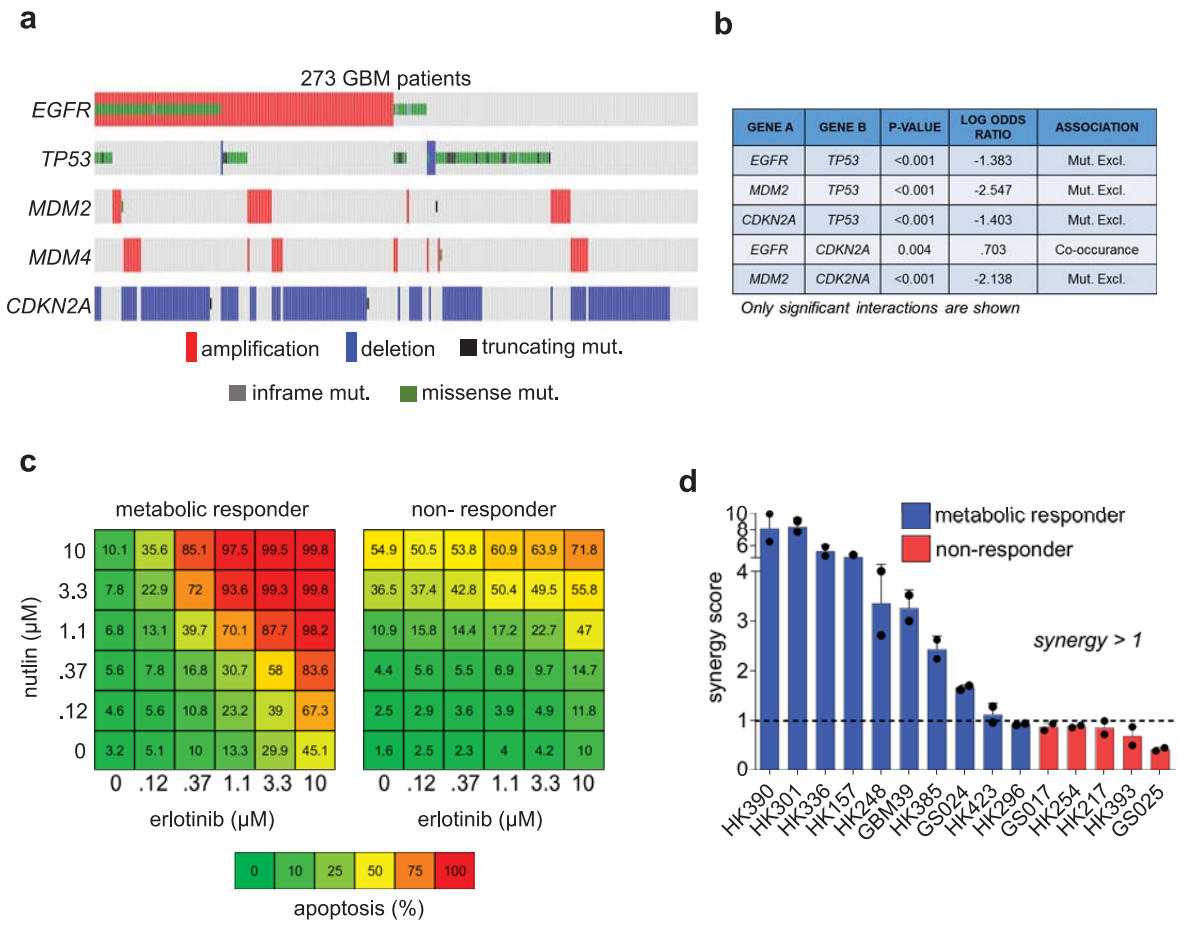
a
273 GBM patients
EGFR
TP53
MDM2
MDM4
CDKN2A
amplification
deletion
truncating mut.
inframe mut.
missense mut.
b
GENE A | GENE B | P-VALUE | LOG ODDS RATIO | ASSOCIATION
EGFR | TP53 | <0.001 | -1.383 | Mut. Excl.
MDM2 | TP53 | <0.001 | -2.547 | Mut. Excl.
CDKN2A | TP53 | <0.001 | -1.403 | Mut. Excl.
EGFR | CDKN2A | 0.004 | .703 | Co-occurance
MDM2 | CDK2NA | <0.001 | -2.138 | Mut. Excl.
Only significant interactions are shown
c
metabolic responder
non- responder
nutlin (μM)
10 3.3 1.1 .37 .12 0
10.1 35.6 85.1 97.5 99.5 99.8
7.8 22.9 72 93.6 99.3 99.8
6.8 13.1 39.7 70.1 87.7 98.2
5.6 7.8 16.8 30.7 58 83.6
4.6 5.6 10.8 23.2 39 67.3
3.2 5.1 10 13.3 29.9 45.1
54.9 50.5 53.8 60.9 63.9 71.8
36.5 37.4 42.8 50.4 49.5 55.8
10.9 15.8 14.4 17.2 22.7 47
4.4 5.6 5.5 6.9 9.7 14.7
2.5 2.9 3.6 3.9 4.9 11.8
1.6 2.5 2.3 4 4.2 10
0 .12 .37 1.1 3.3 10
erlotinib (μM)
0 10 25 50 75 100
apoptosis (%)
d
metabolic responder
non-responder
synergy score
synergy > 1
HK390 HK301 HK336 HK157 HK248 GBM39 HK385 GS024 HK423 HK296 GS017 HK254 HK217 HK393 GS025
e
GFP
GLUT1/3
apoptosis (%)
erlotinib
nutlin
f
HK301
sgCtrl
p53KO
apoptosis (%)
erlotinib
nutlin
g
ip: p53
HK301
erlotinib
nutlin
IgG
Bcl-xL
p53
Bcl-xL
p53
actin
input

Figure 4. Synthetic lethality with combined targeting of EGFR and p53. **(a)** Summary of alterations in *EGFR* and genes involved in p53 regulation across 273 GBM samples. **(b)** Table indicating the significant associations between alterations in *EGFR* and genes involved in the p53 pathway. **(c)** Annexin V staining of a metabolic responder (left: HK301) and non-responder (right: HK393) treated with varying concentrations of erlotinib, nutlin, and in combination represented as a 6 x 6 dose-titration matrix. **(d)** The dose-titration of erlotinib and nutlin as described in (c) was conducted across 10 metabolic responders and 6 non-responders (all p53 wild-type), and the synergy score was calculated (see Materials and Methods) (mean ± s.d., n = 2). Results are representative of two independent experiments. **(e)** Annexin V staining of HK301-GFP and HK301 GLUT1/3 following 72 hours of treatment with 1 μM erlotinib, 2.5 μM nutlin, or both (mean ± s.d., n = 3). Results are representative of two independent experiments. **(f)** Same as (e) but in HK301-sgCtrl and HK301 p53KO (mean ± s.d., n = 3). Results are representative of two independent experiments. **(g)** HK301 was treated for 24 hours with 1 μM erlotinib, 2.5 μM nutlin, or in combination. Immunoprecipitation was performed with immunoglobulin G control antibody or anti-p53 antibody, and the immunoprecipitate was probed with the indicated antibodies. Below are respective pre-immunoprecipitation lysates (input). Comparisons were made using two-tailed unpaired Student's *t*-test. ** p<0.01, *** p<0.001, **** p<0.0001

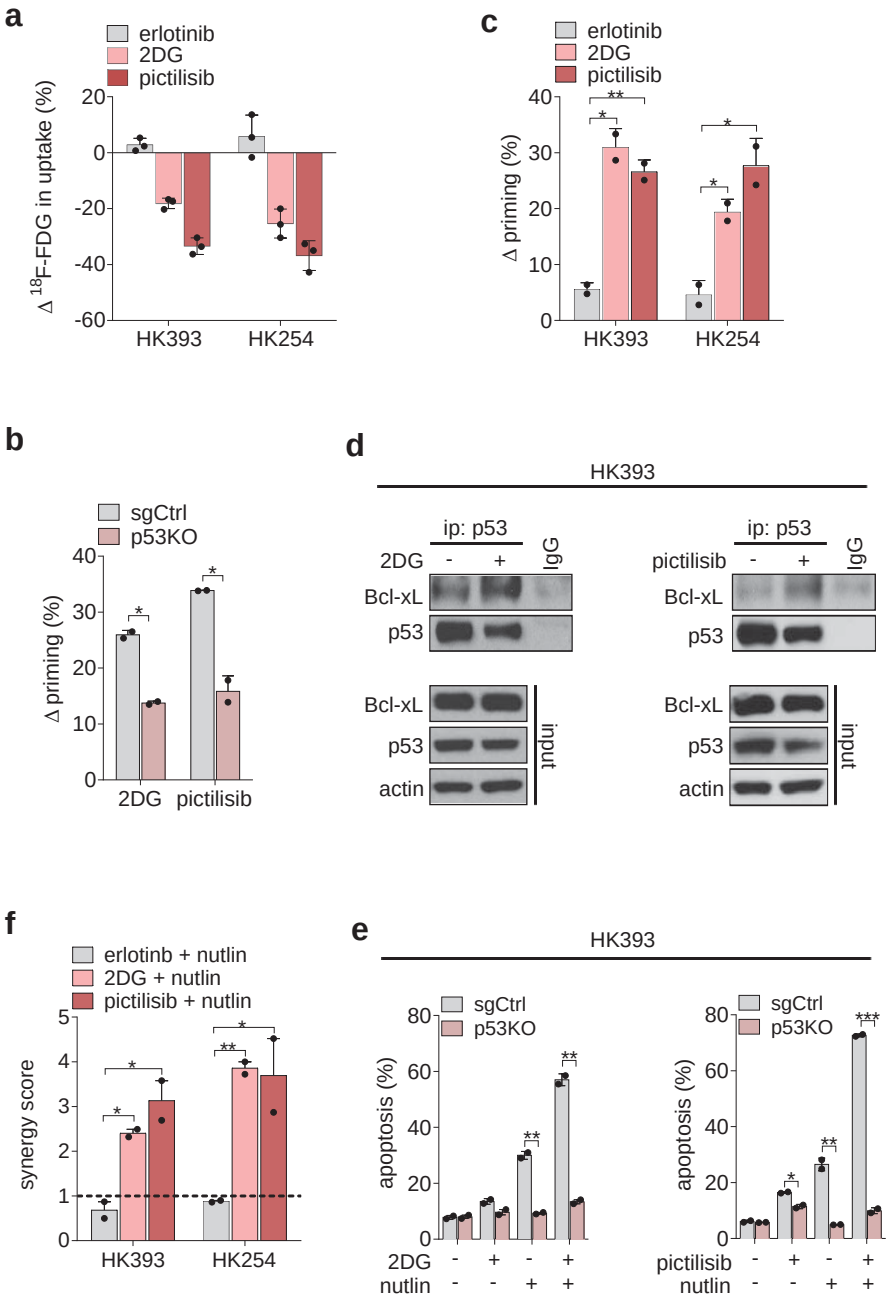
a
erlotinib
2DG
pictilisib
Δ 18F-FDG in uptake (%)
20
0
-20
-40
-60
HK393
HK254
c
erlotinib
2DG
pictilisib
Δ priming (%)
40
30
20
10
0
**
*
*
*
HK393
HK254
b
sgCtrl
p53KO
Δ priming (%)
40
30
20
10
0
*
*
2DG
pictilisib
d
HK393
ip: p53
2DG
-
+
IgG
Bcl-xL
p53
ip: p53
pictilisib
-
+
IgG
Bcl-xL
p53
Bcl-xL
p53
actin
input
Bcl-xL
p53
actin
input
f
erlotinb + nutlin
2DG + nutlin
pictilisib + nutlin
synergy score
5
4
3
2
1
0
*
*
*
**
*
HK393
HK254
e
HK393
sgCtrl
p53KO
apoptosis (%)
80
60
40
20
0
**
**
2DG
nutlin
sgCtrl
p53KO
apoptosis (%)
80
60
40
20
0
***
*
**
pictilisib
nutlin

Figure 5. Modulation of glucose metabolism primes GBM for p53-mediated cell death. (a) % change in ^{18}F-FDG uptake after 4 hours of 1 μM erlotinib, 1 mM 2DG, or 1 μM pictilisib treatment relative to vehicle in HK393 and HK254 (mean ± s.d., *n* = 3). **(b)** The % change, relative to vehicle control, in apoptotic priming as determined by cytochrome *c* release following dynamic BH3 profiling using BIM peptides in HK393 and HK254 following 1 μM erlotinib, 1 mM 2DG, or 1 μM pictilisib for 24 hours (mean ± s.d., *n* = 2). Results are representative of two independent experiments **(c)** Same as (b) but in HK393 sgCtrl and p53KO (mean ± s.d., *n* = 2). **(d)** Immunoprecipitation of p53 in HK393 and HK254 following 24 hours of 1 mM 2DG or 1 μM pictilisib treatment. Immunoprecipitation was performed with immunoglobulin G control antibody or anti-p53 antibody, and the immunoprecipitate was probed with the indicated antibodies. Below are respective pre-immunoprecipitation lysates (input). **(e)** Synergy score of various drugs (erlotinib, 2DG, and pictilisib) in combination with nutlin in HK393 and HK254 (mean ± s.d., *n* = 2). Results are representative of two independent experiments. **(f)** Annexin V staining of HK393 sgCtrl and HK393 p53KO following 72 hours of treatment with 0.5 mM 2DG, 1 μM pictilisib, 1 μM nutlin, 2DG + nutlin, or pictilisib + nutlin. (mean ± s.d., *n* = 2). Results are representative of two nindependent experiments. Comparisons were made using two-tailed unpaired Student's *t*-test. *p<0.05, **p<0.01, ***p<0.001.

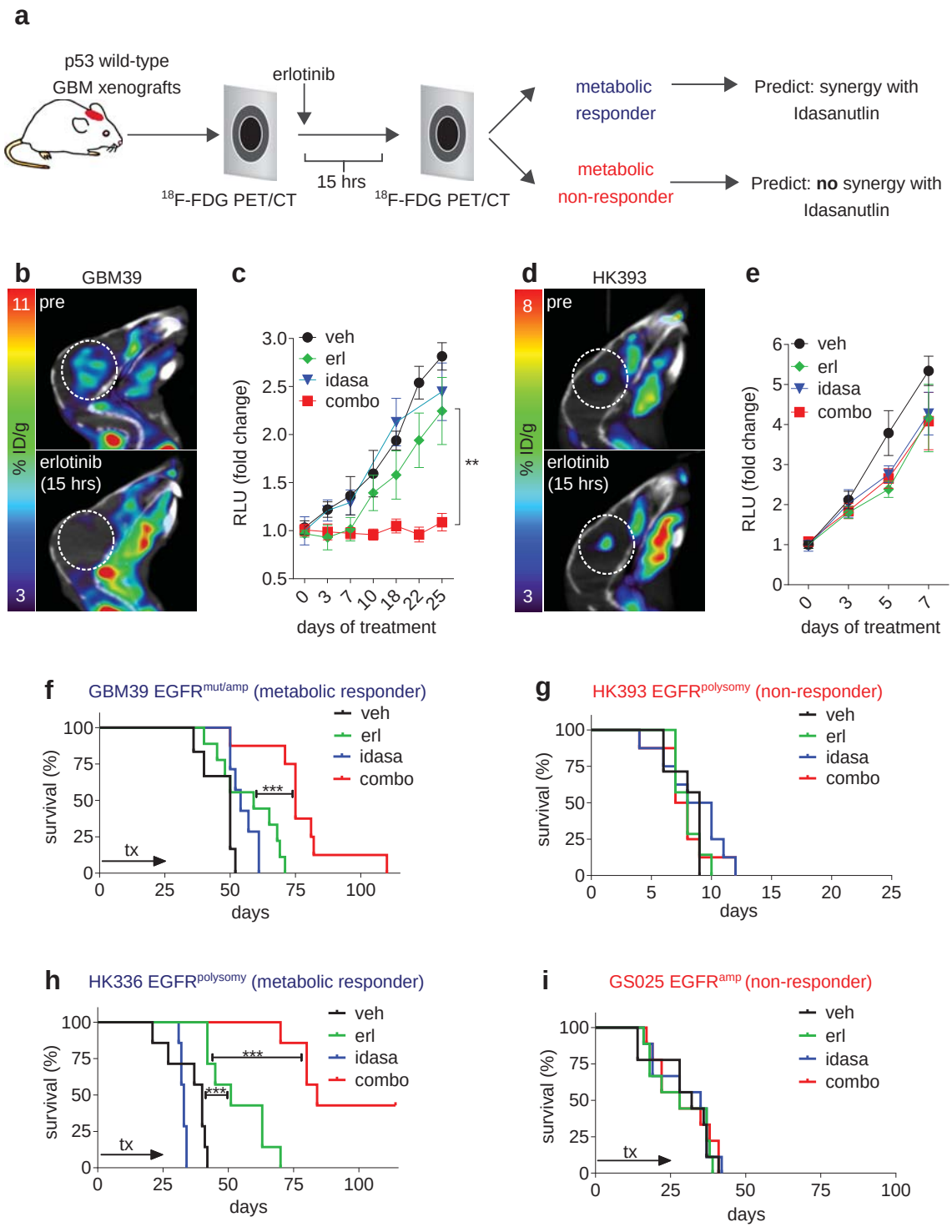
a
p53 wild-type
GBM xenografts
erlotinib
15 hrs
18F-FDG PET/CT
18F-FDG PET/CT
metabolic responder
Predict: synergy with Idasanutlin
metabolic non-responder
Predict: no synergy with Idasanutlin
b
GBM39
pre
erlotinib (15 hrs)
% ID/g
11
3
c
RLU (fold change)
days of treatment
veh
erl
idasa
combo
**
d
HK393
e
f
GBM39 EGFRmut/amp (metabolic responder)
survival (%)
days
tx
***
g
HK393 EGFRpolysomy (non-responder)
h
HK336 EGFRpolysomy (metabolic responder)
i
GS025 EGFRamp (non-responder)

Figure 6. Combined targeting of EGFR-driven glucose uptake and p53 suppresses tumor growth *in vivo*. (a) Schematic of approach to use ^{18}F-FDG PET to rapidly predict changes in glucose uptake with EGFRi and consequently sensitivity to p53 stabilization with Idasanutlin. **(b)** Representative ^{18}F-FDG PET/CT images of GBM39 intracranial xenografts scanned before and after 15 hours of 75 mg/kg erlotinib treatment (*n* = 3 mice). **(c)** GBM39 intracranial xenografts were treated with vehicle (*n* = 6), 75 mg/kg erlotinib (*n* = 9), 50 mg/kg Idasanutlin (*n* = 7), or in combination daily (*n* = 8), and tumor burden was assessed at indicated days using secreted *gaussia* luciferase (mean ± s.d.) (see Materials and Methods for *gaussia* luciferase measurements). **(d)** Same as (b) but in HK393 intracranial xenografts. **(e)** Same as (c) but in HK393 intracranial xenografts (mean ± s.d., *n* = 7 for all groups). **(f)** % survival of (c). **(g)** % survival of (e). **(h)** % survival of metabolic responder HK336 following indicated treatments for 25 days and then released from drug (*n* = 7 for all groups). **(i)** % survival of non-responder GS025 following indicated treatments for 25 days and then released from drug (*n* = 9 for all groups). Comparisons for (c) and (e) used data sets from the last measurements and were made using two-tailed unpaired *t*-test. Kaplan–Meier survival analysis (log-rank) was used for (f) – (i). **p <0.01, ***p<0.001.

Supplementary Figure 1

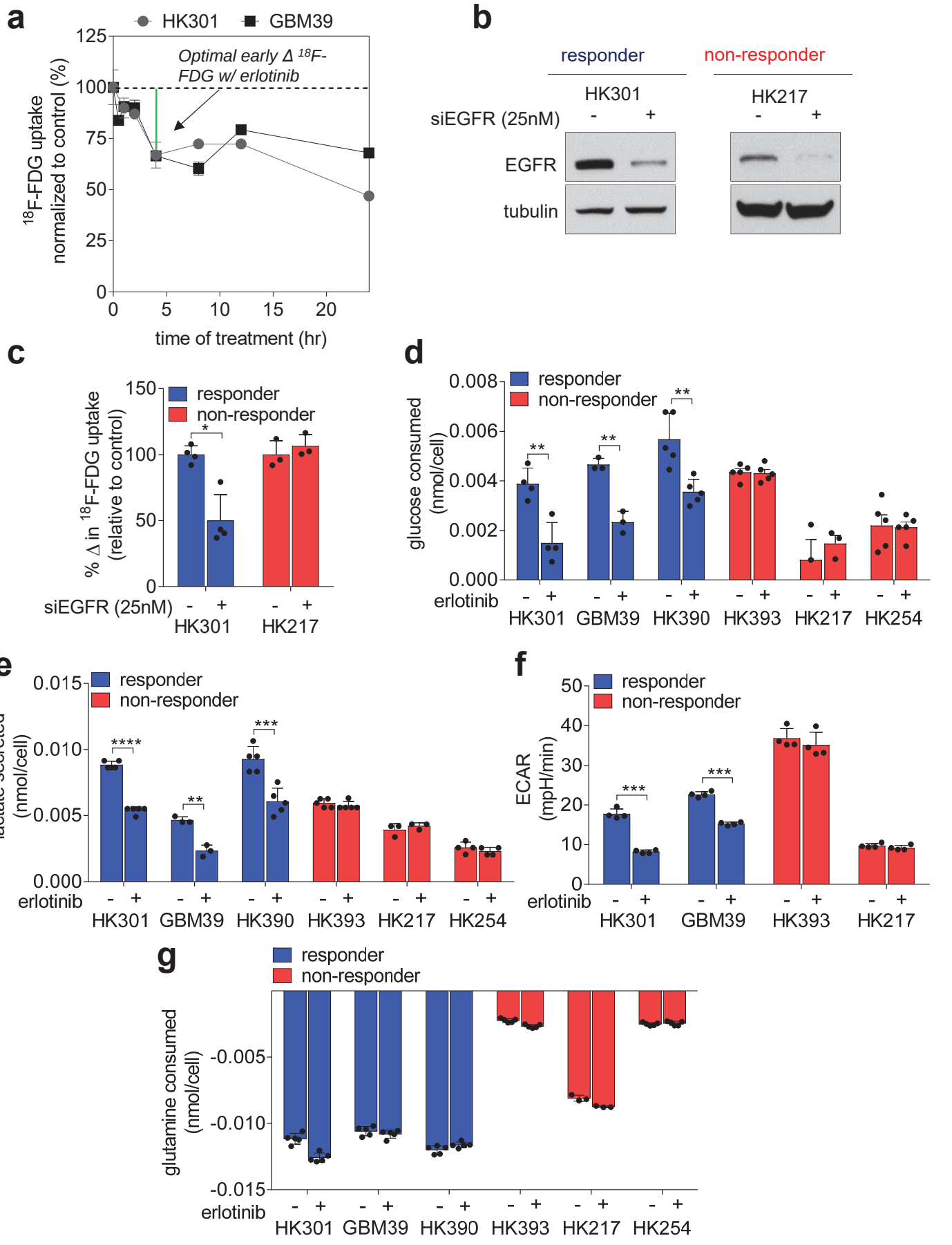

Supplementary Figure 1. Characterization of GBM cell lines following EGFR inhibition. (a) % change in ^{18}F-FDG uptake at indicated times of 1 μM erlotinib treatment relative to vehicle in two metabolic responders (HK301 and GBM39) (mean ± s.d., n = 3) **(b)** Immunoblot of indicated proteins of a metabolic responder (HK301) and non-responder (HK217) following genetic knockdown of EGFR with siRNA (25 nM). **(c)** % change in ^{18}F-FDG uptake in HK301 and HK217 following genetic knockdown of EGFR (mean ± s.d., n = 3). Absolute levels of glucose consumption **(d)** and lactate secretion **(e)** with 12 hours of 1 μM erlotinib treatment in three metabolic responders (HK301, GBM39, HK390) and three non-responders (HK393, HK217, HK254). Measurements were made using Nova Biomedical BioProfile Analyzer (mean ± s.d. For glucose consumption: n = 3 gliomasphere samples for GBM39, HK217. n = 4 gliomasphere samples for HK301. n = 5 gliomasphere samples for HK390, HK393, HK254. For lactate secretion: n = 3 gliomasphere samples for GBM39, HK217. n = 4 gliomasphere samples for HK301, HK254. n = 5 gliomasphere samples for HK390, HK393). **(f)** Basal extracellular acidification rate (ECAR) measurements of two responders (HK301 and GBM39, in blue) and two non-responders (HK217 and HK393, in red) following 12 hours of 1 μM erlotinib treatment (mean ± s.d., n = 4). **(g)** Absolute levels of glutamine consumption following 12 hours of 1 μM erlotinib treatment, as measured by Nova Biomedical BioProfile Analyzer (mean ± s.d., n = 3 gliomasphere samples for HK217. n = 5 gliomasphere samples for GBM39. HK301, HK390, HK393, HK254). Comparisons were made using two-tailed unpaired Student's t-test. *P < 0.05, **P < 0.01, ***P < 0.001.

Supplementary Figure 2

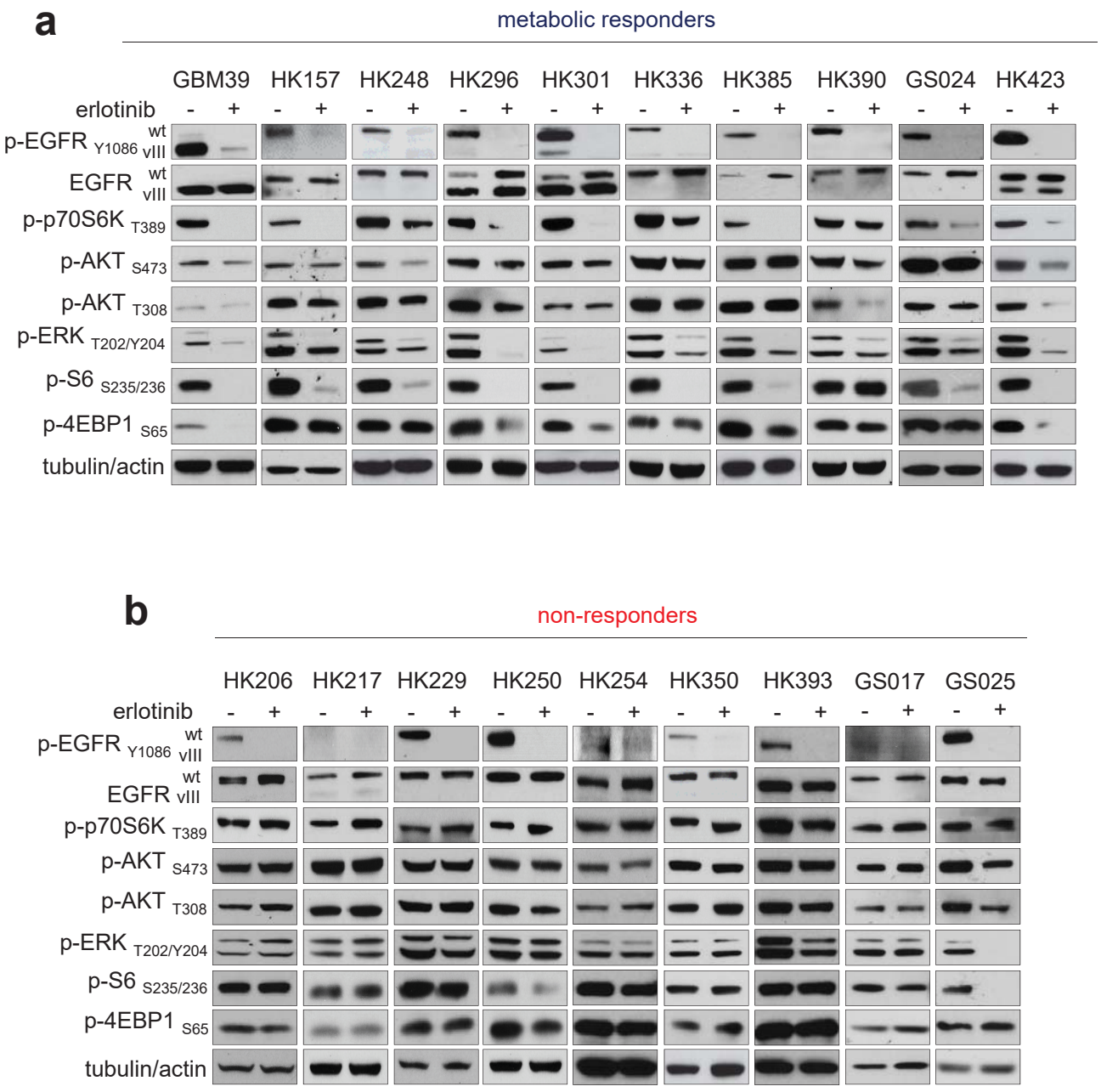

Supplementary Figure 2. Alterations in downstream signaling following EGFR inhibition correlate with metabolic response. (a) Immunoblot of indicated proteins following 4 hours of 1 μM erlotinib treatment in metabolic responders and **(b)** non-responders.

Supplementary Figure 3

a

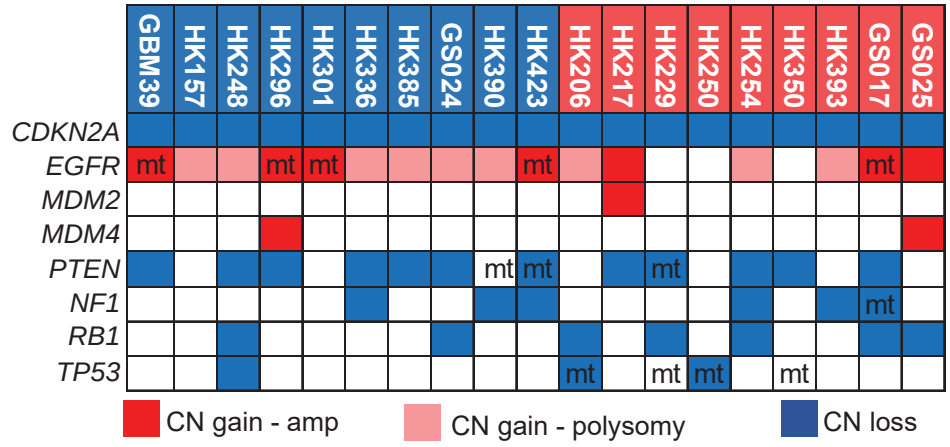

b

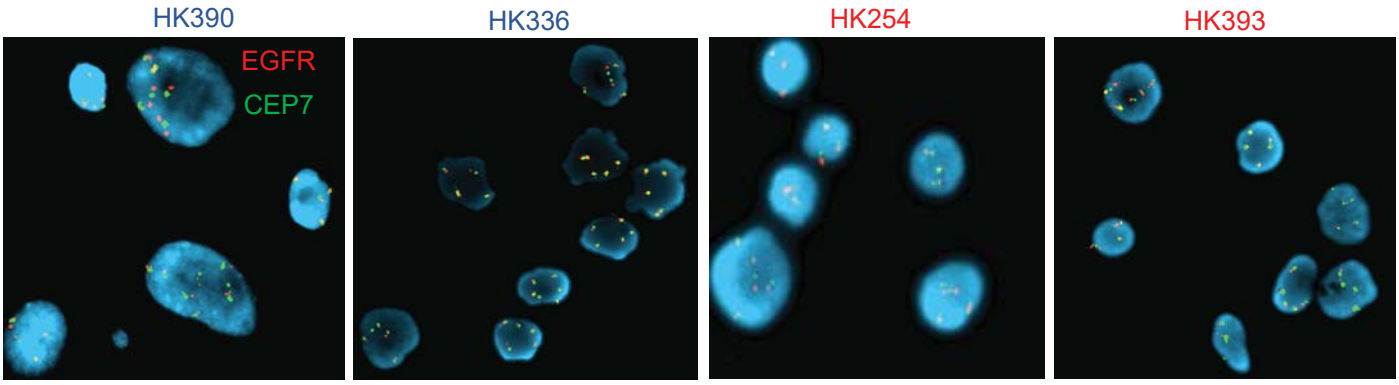

Supplementary Figure 3. Genetic characterization of patient-derived GBM cell lines. **(a)** Genetic background across a panel of GBM lines. **(b)** Fluorescence *in situ* hybridization (FISH) of HK390, HK336, HK254, and HK393 showing polysomy of *EGFR*.

Supplementary Figure 4

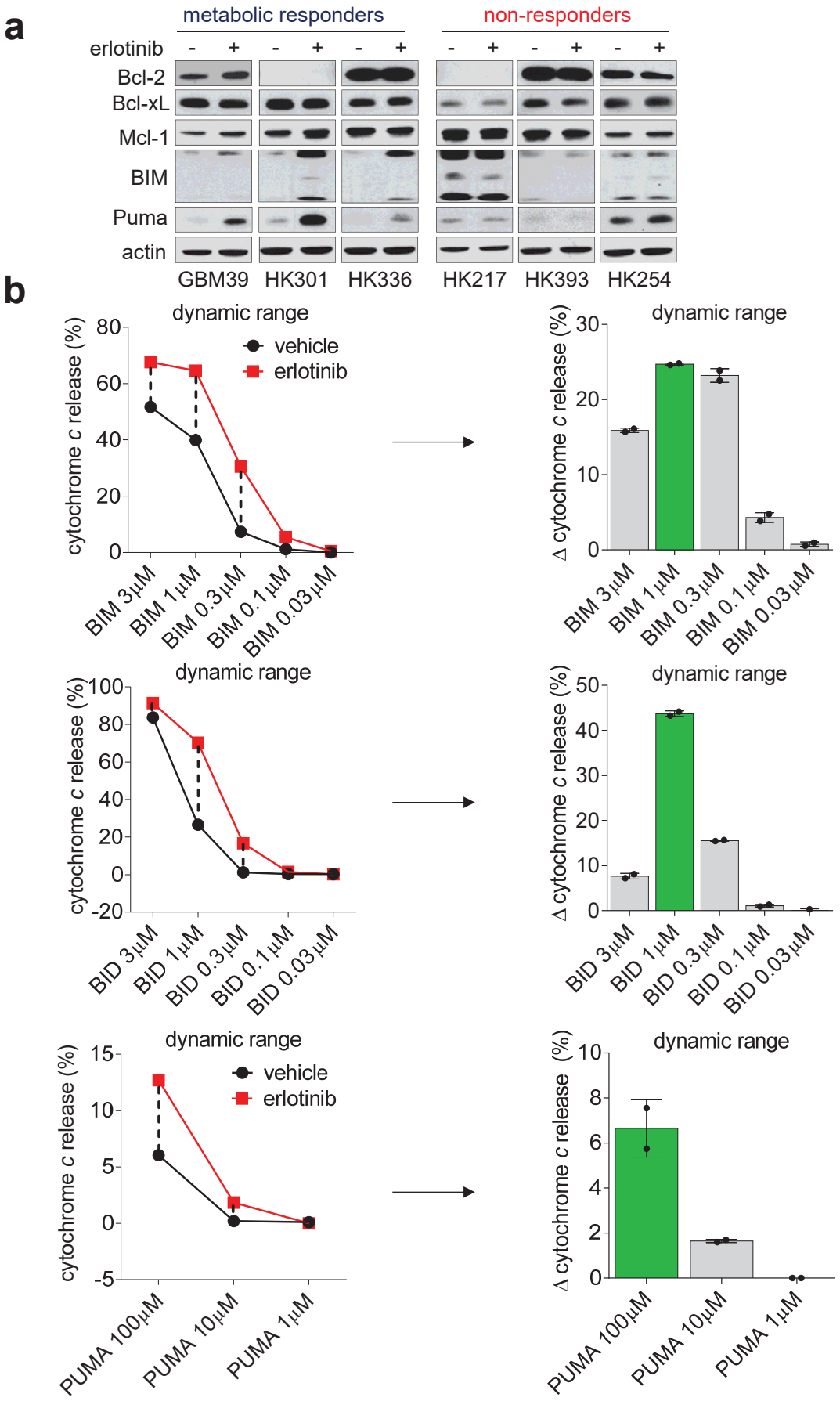

Supplementary Figure 4. EGFR inhibition shifts the apoptotic balance in metabolic responders. (a) Immunoblot of indicated proteins following 24 hour treatment with 1 μM erlotinib in metabolic responders (GBM39, HK301, and HK336) and non-responders (HK217, HK393, and HK254). **(b)** Example of dynamic BH3 profiling analysis in a metabolic responder (HK301). Left: % cytochrome c release is measured following exposure to various peptides at indicated concentrations to obtain the dynamic range. Right: % Δ cytochrome c release (erlotinib – vehicle) for each peptide and concentration is determined and the maximum response (i.e. maximum % Δ cytochrome c release) is the "% Δ apoptotic priming" as indicated by the green bar.

Supplementary Figure 5

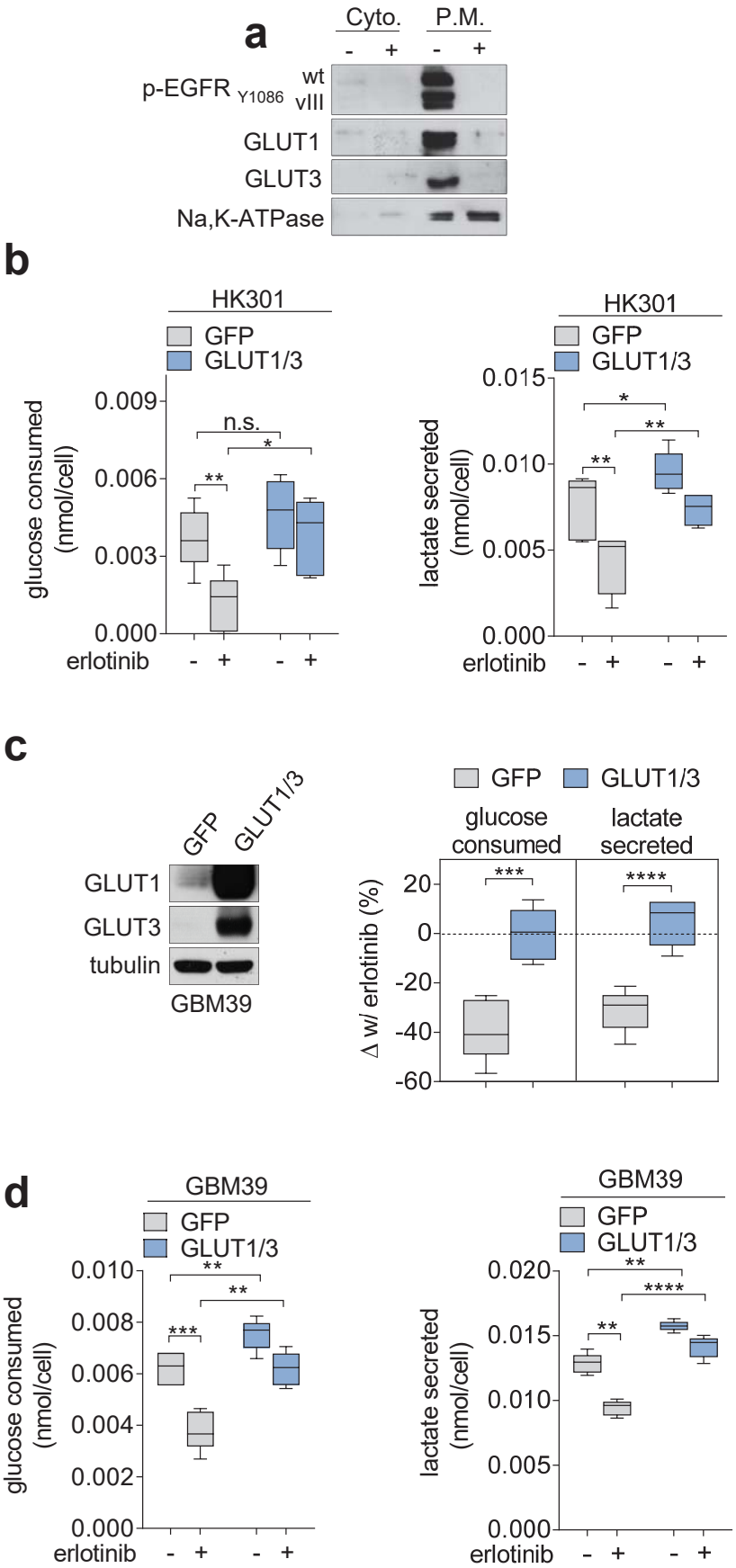

Supplementary Figure 5. GLUT1/3 overexpression rescues attenuated glucose metabolism caused by EGFR inhibition. (a) Immunoblot of cytosolic (Cyto.) and plasma membrane (P.M.) fractionations of HK301 cells 4 hours of 1 μM erlotinib treatment. **(b)** Absolute measurements of glucose consumption and lactate secretion with 12 hours of 1 μM erlotinib treatment in HK301 cells overexpressing GFP control or GLUT1 and GLUT3 (GLUT1/3). Measurements were made using Nova Biomedical BioProfile Analyzer (mean ± s.d. For glucose consumption: HK301-GFP vehicle $n = 8$, HK301-GFP erlotinib $n = 5$, HK301-GLUT1/3 vehicle $n = 8$, HK301-GLUT1/3 erlotinib $n = 5$. For lactate secretion: HK301-GFP vehicle $n = 8$, HK301-GFP erlotinib $n = 8$, HK301-GLUT1/3 vehicle $n = 6$, HK301-GLUT1/3 erlotinib $n = 4$). **(c)** Left: Immunoblot of whole cell lysate of GBM39 cells overexpressing GFP control or GLUT1 and GLUT3 (GLUT1/3). Right: Relative changes in glucose consumption or lactate secretion of GBM39-GFP or GBM39-GLUT1/3 after 12 hours of 1 μM erlotinib treatment. Values are relative to vehicle control (mean ± s.d. For glucose consumption: GBM39-GFP $n = 5$, GBM39-GLUT1/3 $n = 5$. For lactate secretion: GBM39-GFP $n = 7$, GBM39-GLUT1/3 $n = 5$). **(d)** Same as (b) but in GBM39-GFP and GBM39-GLUT1/3 (mean ± s.d., $n = 5$). In the box plots, the central rectangle spans the first quartile to the third quartile (the interquartile range or IQR), the central line inside the rectangle shows the mean, and whiskers above and below the box show the locations of the minimum and maximum within 1.5 IQR of the lower quartile and the upper quartile, respectively. Comparisons were made using two-tailed unpaired Student's *t*-test. $*P < 0.05$, $**P < 0.01$, $***P < 0.001$, $****P < 0.0001$.

Supplementary Figure 6

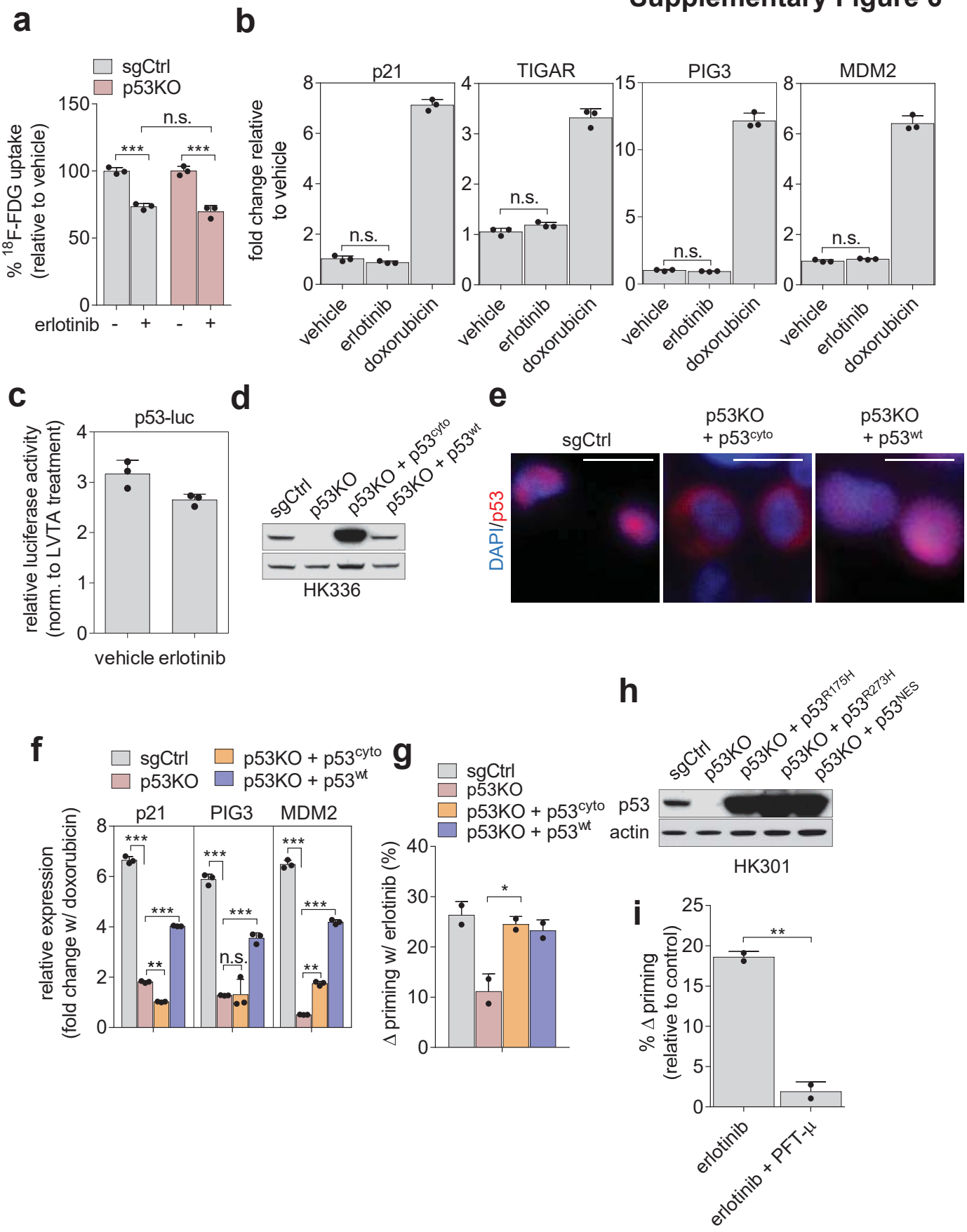

Supplementary Figure 6. Cytoplasmic p53 is required for erlotinib-mediated apoptotic priming. (a) % change in ^{18}F-FDG uptake following 4 hours of 1 μM erlotinib treatment in HK301 sgCtrl and p53 KO cells (mean ± s.d., *n* = 3). **(b)** Relative mRNA levels of p53-regulated genes following 24 hours 1 μM erlotinib or 100 nM doxorubicin treatment in HK301 (metabolic responder). **(c)** HK301 cells infected with a p53-luciferase reporter system and p53 activity was measured following 24 hours of 1 μM erlotinib treatment (mean ± s.d., *n* = 3). Results are representative of two independent experiments. **(d)** Immunoblot of indicated proteins in HK336 sgCtrl, p53KO, p53KO + $p53^{cyto}$, and p53KO + $p53^{wt}$. **(e)** Immunofluorescence of p53 protein combined with DAPI staining to reveal protein localization in HK336 sgCtrl, p53KO + $p53^{cyto}$, and p53KO + $p53^{wt}$ (scale bars = 20 μm). **(f)** Changes in indicated mRNA levels following 100 nM doxorubicin treatment for 24 hours in HK336 sgCtrl, p53KO, p53KO + $p53^{cyto}$, and p53KO + $p53^{wt}$ (mean ± s.d., *n* = 3). Levels were normalized to respective DMSO treated cells. **(g)** The % change, relative to vehicle control, in apoptotic priming - as determined by cytochrome c release following exposure to BIM peptide - in HK336 sgCtrl, p53KO, p53KO + $p53^{cyto}$, and p53KO + $p53^{wt}$ cells treated with erlotinib for 24 hours (mean ± s.d., *n* = 2). Results are representative of two independent experiments. **(h)** Immunoblot of indicated proteins in HK301 sgCtrl, p53KO, p53KO + $p53^{R175H}$, p53KO + $p53^{R273H}$, and p53KO + $p53^{NES}$. **(i)** The % change in priming in HK301 following 24 hours 1 μM of erlotinib treatment with or without PFTμ pre-treatment (10μM for 2 hours) (mean ± s.d., *n* = 2). Results are representative of two independent experiments. All comparisons were made using two-tailed unpaired Student's *t*-test. * $P < 0.05$, ** $P < 0.01$, *** $P < 0.001$.

Supplementary Figure 7

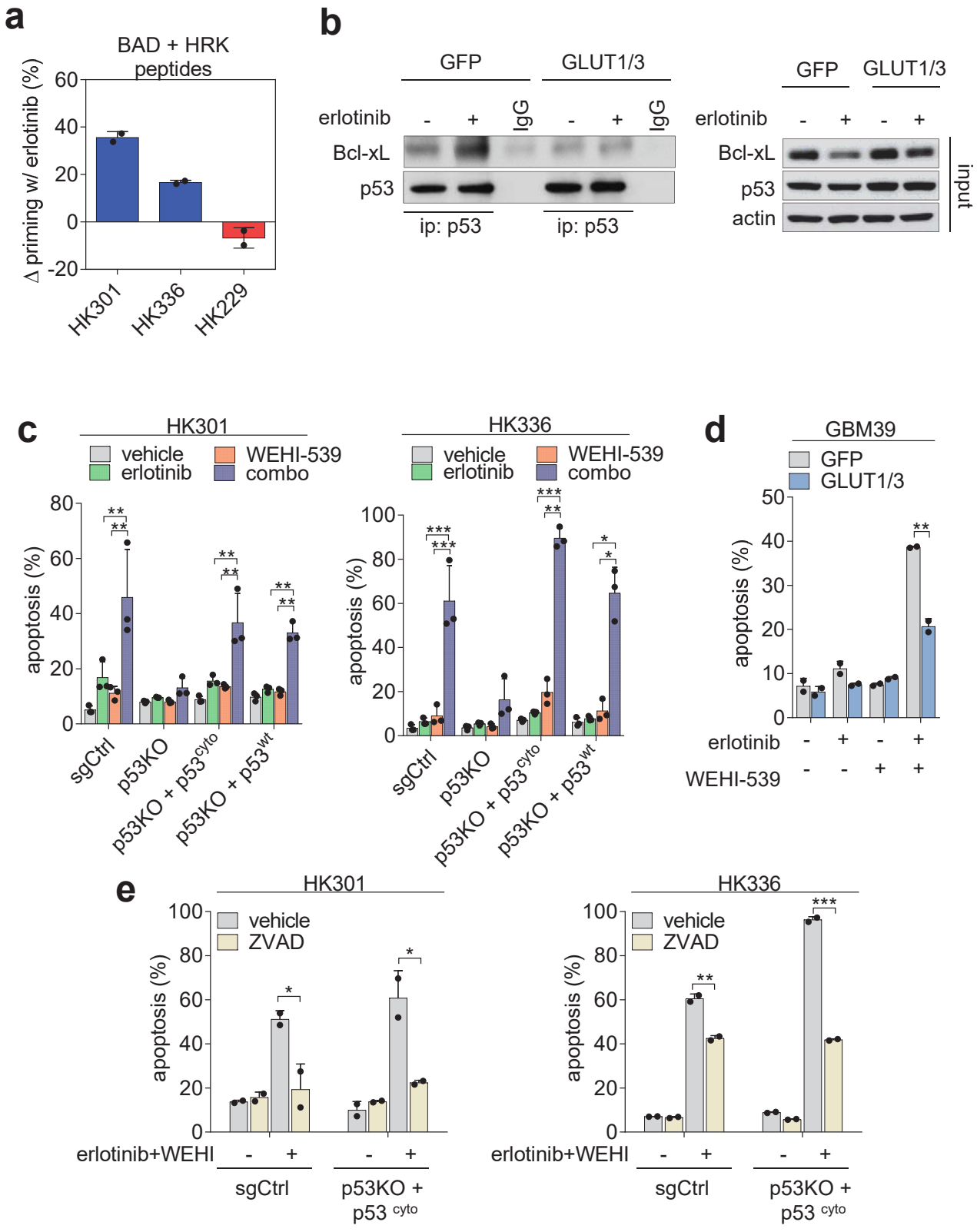

Supplementary Figure 7. Inhibition of EGFR-driven glucose metabolism induces a Bcl-xL dependency through cytoplasmic p53 functions. (a) The % change, relative to vehicle control, in priming as determined by cytochrome *c* release following exposure to BAD and HRK peptides (100 μM) in metabolic responders (HK301 and HK336) or non-responder (HK229) treated with 1 μM erlotinib for 24 hours (mean ± s.d., $n = 2$). **(b)** Left: Immunoprecipitation of p53 in GBM39 GFP and GBM39 GLUT1/3 following 24 hours of 1 μM erlotinib treatment. The immunoprecipitate was probed with the indicated antibodies. Right: respective pre-immunoprecipitation lysates (input). Results are representative of two independent experiments. **(c)** Annexin V staining of HK301 (left) and HK336 (right) sgCtrl, p53KO, p53 KO + $p53^{cyto}$, and p53KO + $p53^{wt}$ following 72 hours of treatment with 1 μM erlotinib, WEHI-539 (1 μM for HK301 and GBM39, 5 μM for HK336), or combination (mean ± s.d., $n = 3$). Results are representative of two independent experiments. **(d)** Same as (c) but in GBM39-GFP and GBM39-GLUT1/3 (mean ± s.d., $n = 2$). Results are representative of two independent experiments. **(e)** Annexin V staining of HK301 (left) and HK336 (right) sgCtrl and p53 KO + $p53^{cyto}$ following 72 hours of treatment with 1 μM erlotinib + WEHI-539 (1 μM for HK301, 5 μM for HK336) with or without ZVAD (50 μM) (mean ± s.d., $n = 2$). Results are representative of two independent experiments. Comparisons were made using two-tailed unpaired Student's *t*-test. $*P < 0.05$, $**P < 0.01$, $***P < 0.001$.

Supplementary Figure 8

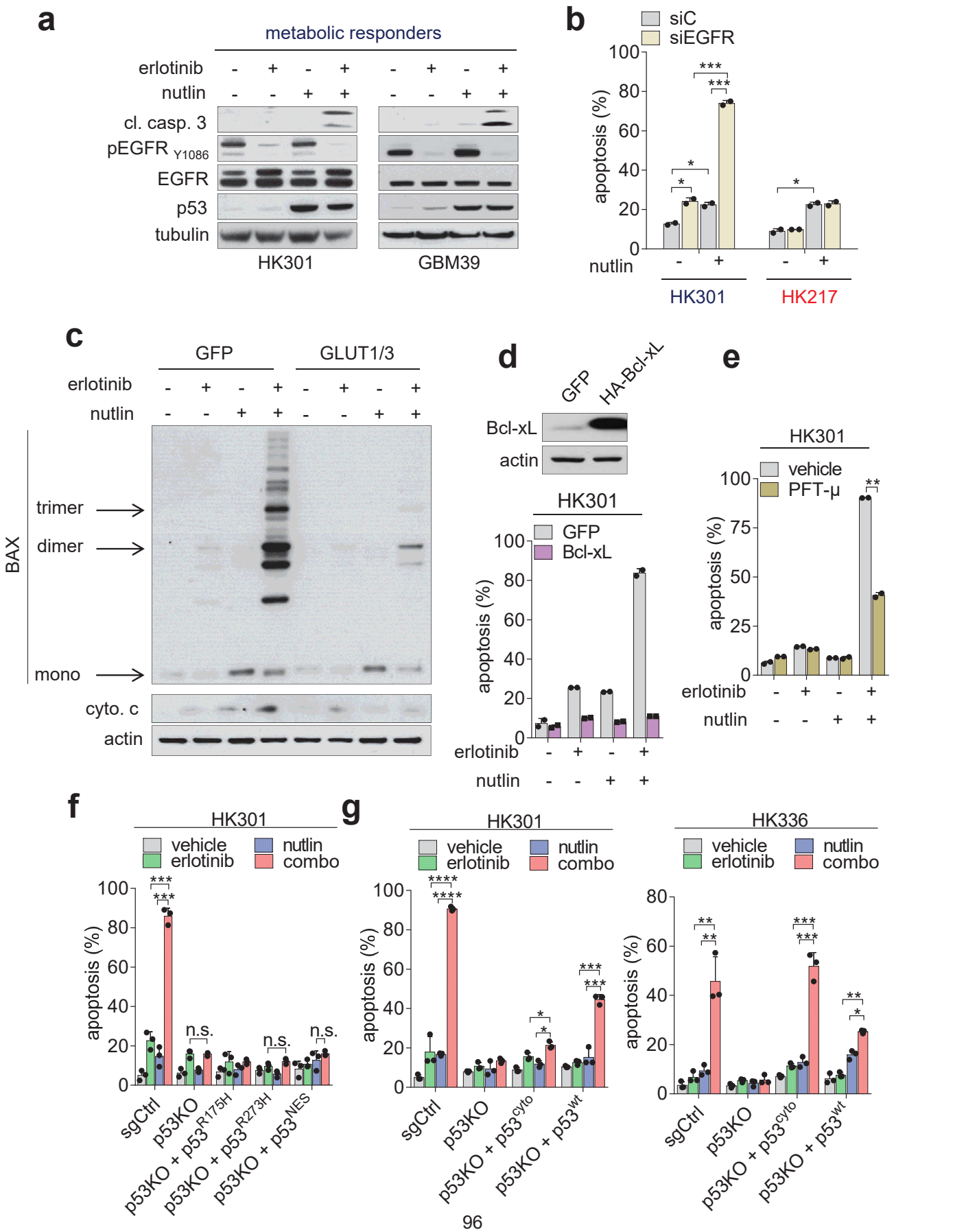

Supplementary Figure 8. Combined targeting of EGFR-driven glucose metabolism and p53 promote intrinsic apoptosis in GBM. (a) Immunoblot of indicated proteins following 24 hours of 1 μM erlotinib, 2.5 μM nutlin or in combination in two metabolic responders (HK301 and GBM39). **(b)** Annexin V staining in HK301 and HK217 following genetic knockdown of EGFR (25 nM) and subsequent 2.5 μM nutlin treatment for 72 hours (mean ± s.d., *n* = 2). Results are representative of two independent experiments. **(c)** Detection of BAX oligomerization in HK301-GFP and HK301-GLUT1/3. Following 24 hours of indicated treatment, cells were harvested and incubated in 1 mM BMH to promote protein cross-linking and immunoblotted with indicated antibodies. Below BAX is immunoblot for cytosolic cytochrome *c* following cellular fractionation. Results are representative of two independent experiments. **(d)** Top: Immunoblot of indicated proteins in HK301-GFP and HK301-HA-BclxL. Bottom: Annexin V staining in HK301-GFP and HK301-HA-BclxL following 72 hours of treatment with 1 μM erlotinib, 2.5 μM nutlin, or combination (mean ± s.d., *n* = 2). Results are representative of two independent experiments. **(e)** Annexin V staining of HK301 following 72 hours of 1 μM erlotinib, 2.5 μM nutlin or the combination +/- PFTμ pretreatment (10μM for 2 hours) (mean ± s.d., *n* = 3). Results are representative of two independent experiments. **(f)** Annexin V staining of HK301 sgCtrl, p53KO, p53KO + $p53^{R175H}$, p53KO + $p53^{R273H}$, and p53KO + $p53^{NES}$ following 72 hours of treatment with 1 μM erlotinib, 2.5 μM nutlin, or combination (mean ± s.d., n = 2). Results are representative of two independent experiments. **(g)** Same as (f) but in HK301 (left) and HK336 (right) sgCtrl, p53KO, p53KO + $p53^{cyto}$, and p53KO + $p53^{wt}$ (mean ± s.d., *n* = 3). Results are representative of two independent experiments. Comparisons were made using two-tailed unpaired Student's t-test. **P* < 0.05, ***P* < 0.01, ****P* < 0.001, *****P* < 0.0001.

Supplementary Figure 9

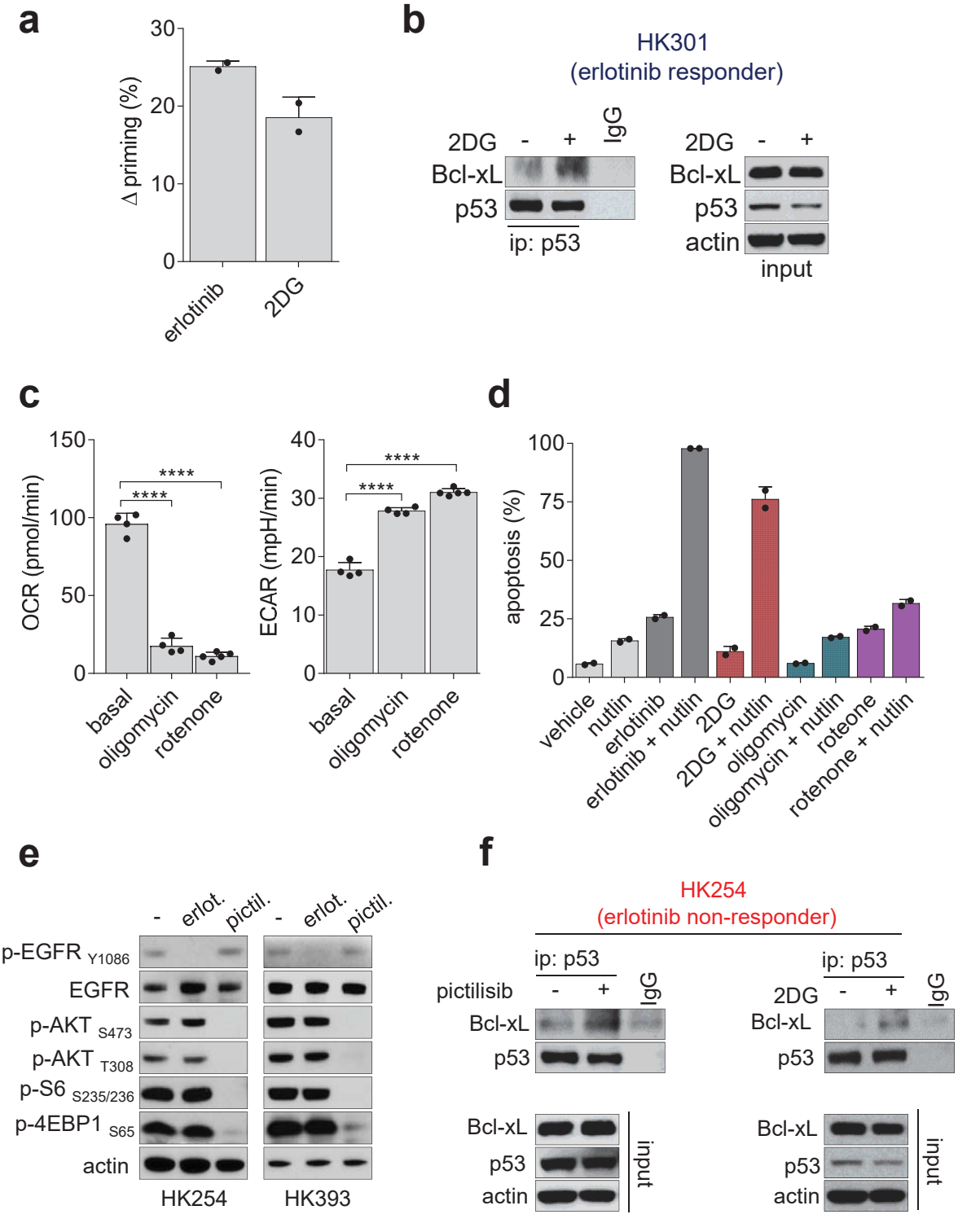

Supplementary Figure 9. Inhibition of glucose metabolism in metabolic responders and non-responders promotes intrinsic apoptosis. (a) The % change, relative to vehicle control, in priming as determined by cytochrome *c* release following exposure to BIM peptides in metabolic responder HK301 following 24 hours of 1 μM erlotinib or 3 mM 2DG treatment (mean ± s.d., $n = 2$). Results are representative of two independent experiments. **(b)** Left: Immunoprecipitation of p53 in HK301 following 24 hours of 3 mM 2DG treatment. The immunoprecipitate was probed with the indicated antibodies. Right: respective pre-immunoprecipitation lysates (input). **(c)** Oxygen consumption rate (OCR) and extracellular acidification rate (ECAR) measurements of HK301 cells following exposure to 1 μM oligomycin and 1 μM rotenone (mean ± s.d., $n = 2$). Results are representative of two independent experiments. **(d)** Annexin V staining in HK301 following 72 hours of treatment with 2.5 μM nutlin, 1 μM erlotinib, 3 mM 2DG, 1 μM oligomycin, 1 μM rotenone as individual agents or in combination with 2.5 μM nutlin (mean ± s.d., $n = 2$). Results are representative of two independent experiments. **(e)** Immunoblot of indicated proteins following 4 hours of 1 μM erlotinib or 1 μM pictilisib treatment in two non-responders (HK254 and HK393). **(f)** Immunoprecipitation of p53 in HK254 following 24 hours of 1 μM pictilisib or 1 mM 2DG treatment. The immunoprecipitate was probed with the indicated antibodies. Below are respective pre-immunoprecipitation lysates (input). Results are representative of two independent experiments. Comparisons were made using two-tailed unpaired Student's t-test. ****$P < 0.0001$.

Supplementary Figure 10

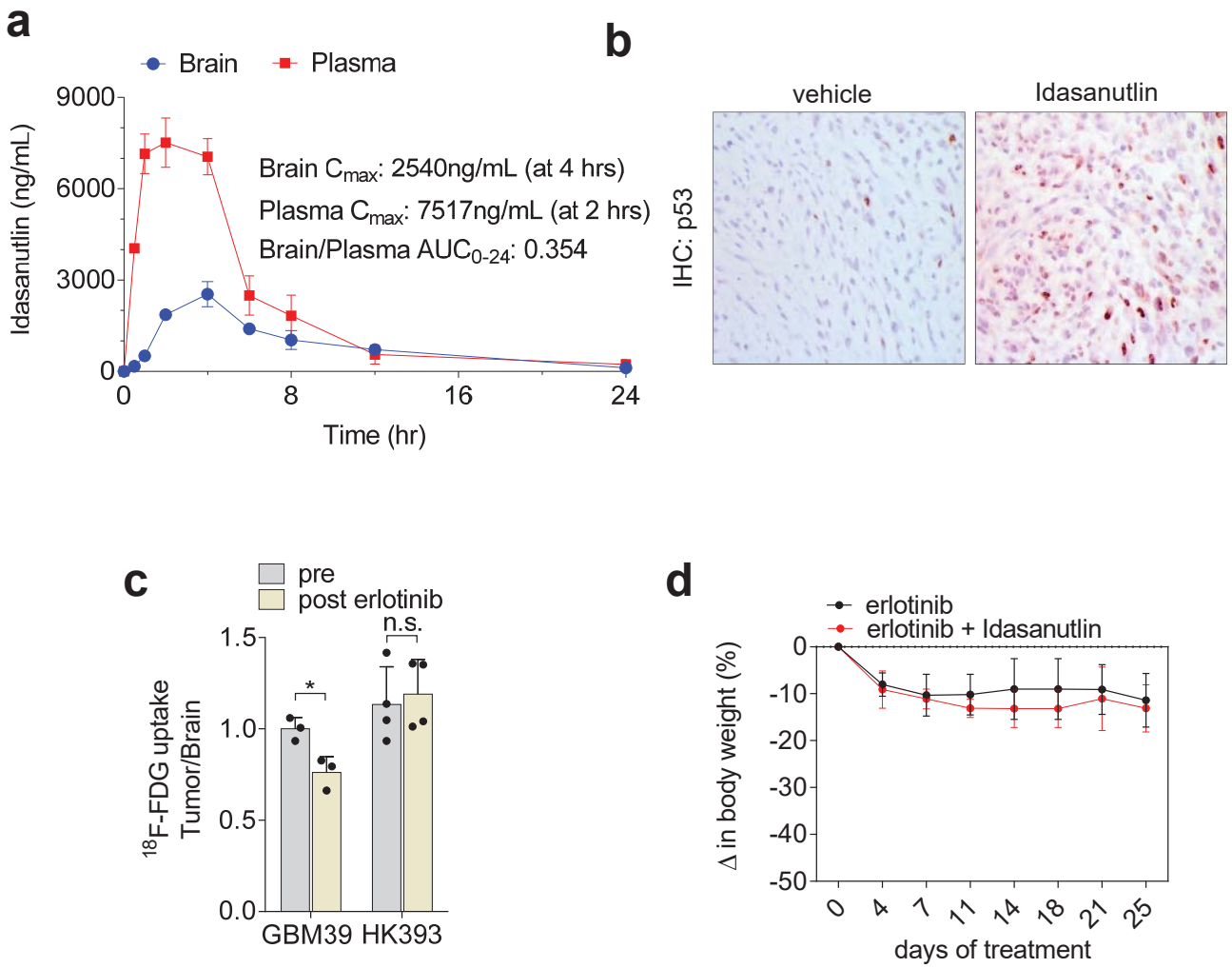

Supplementary Figure 10. *In vivo* efficacy of combined targeting of EGFR inhibition and p53 in GBM. (a) Brain and plasma concentrations of Idasanutlin at indicated time points in non-tumor bearing mice (mean ± s.d., n = 2 mice/time point). Results are representative of two independent experiments. **(b)** Immunohistochemistry (IHC) analysis of p53 expression in intracranial tumor-bearing xenografts following 36 hours of 50 mg/kg Idasanutlin treatment. **(c)** % change in ^{18}F-FDG uptake following 15 hours of 75 mg/kg erlotinib treatment in GBM39 (n = 3) and HK393 (n = 4) intracranial xenografts (mean ± s.d.). **(d)** Change in mice body weight following daily treatment with 75 mg/kg erlotinib or combined 75 mg/kg erlotinib and 50 mg/kg Idasanutlin. All treatments were done orally. *$P < 0.05$.

Supplementary Figure 11

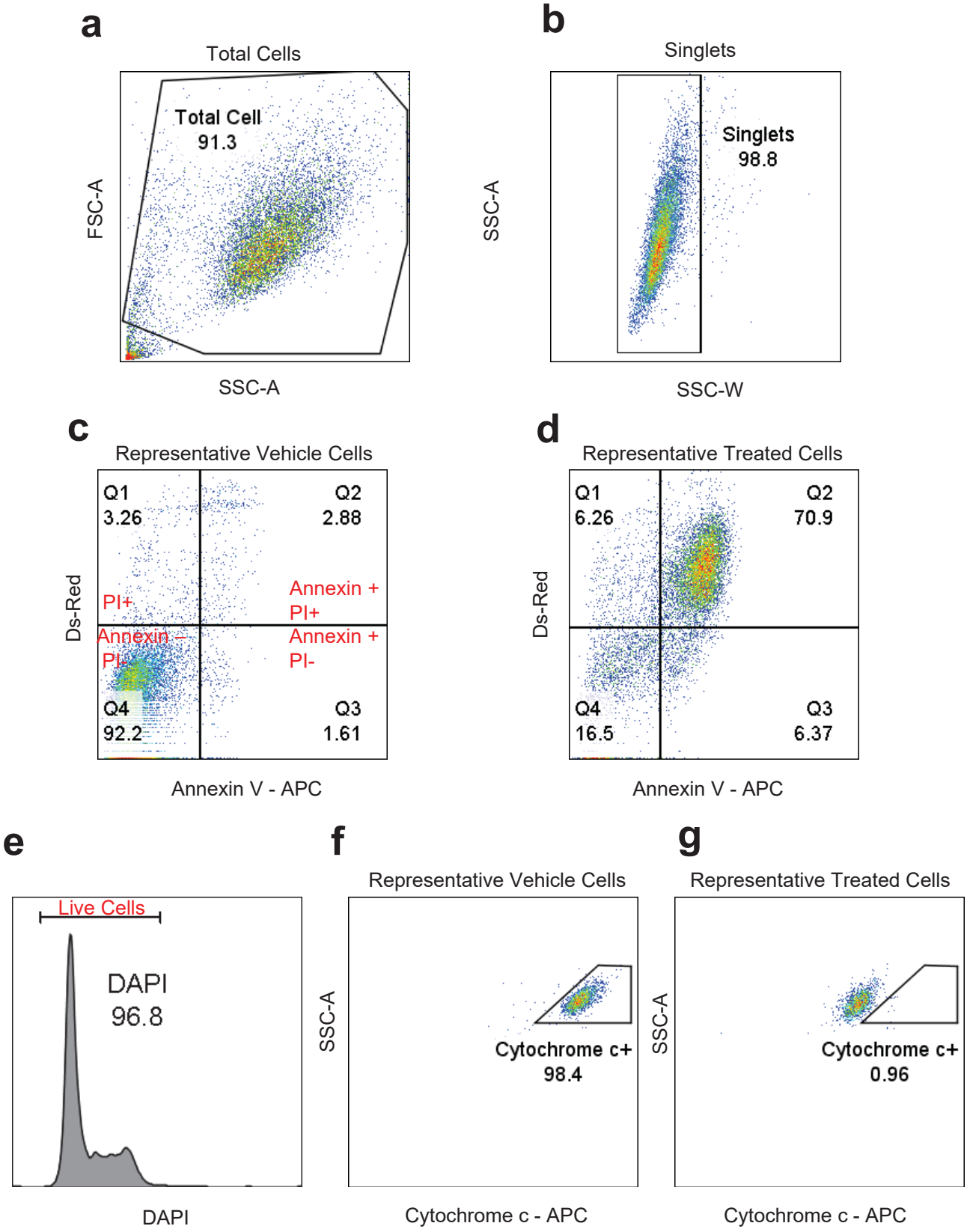

Supplementary Figure 11. Flow cytometry gating strategy. Cells were first disassociated with trypsin into single cell suspensions. **(a)** Total cells were gated for based on forward scatter area (FSC-A) and side scatter area (SSC-A). **(b)** This population was then gated for singlets using side scatter area (SSC-A) and side scatter width (SSC-W). Singlet population was then used to examine Annexin V+ and PI staining. For apoptotic staining, unstained cells were used to set the gates and vehicle treated cells **(c)** were used for comparison to treated cells **(d)** for analysis of apoptosis. For BH3 profiling, singlets were gated for DAPI staining **(e)** to select out sub-G1 (dead) cells. Cytochrome *c* staining was then analyzed as seen in vehicle treated cells **(f)** and peptide treated cells **(g)**. Numbers indicate percentages in each gate.

REFERENCES

1 Brennan, C. W. *et al.* The somatic genomic landscape of glioblastoma. *Cell* **155**, 462-477, doi:10.1016/j.cell.2013.09.034 (2013).

2 Vivanco, I. *et al.* Differential sensitivity of glioma- versus lung cancer-specific EGFR mutations to EGFR kinase inhibitors. *Cancer Discov* **2**, 458-471, doi:2159-8290.CD-11-0284 [pii] 10.1158/2159-8290.CD-11-0284 (2012).

3 Cloughesy, T. F., Cavenee, W. K. & Mischel, P. S. Glioblastoma: from molecular pathology to targeted treatment. *Annu Rev Pathol* **9**, 1-25, doi:10.1146/annurev-pathol-011110-130324 (2014).

4 Lee, E. Q. *et al.* Phase I/II study of sorafenib in combination with temsirolimus for recurrent glioblastoma or gliosarcoma: North American Brain Tumor Consortium study 05-02. *Neuro Oncol* **14**, 1511-1518, doi:10.1093/neuonc/nos264 (2012).

5 Wen, P. Y. *et al.* Phase I/II study of erlotinib and temsirolimus for patients with recurrent malignant gliomas: North American Brain Tumor Consortium trial 04-02. *Neuro Oncol* **16**, 567-578, doi:10.1093/neuonc/not247 (2014).

6 Lee, Michael J. *et al.* Sequential Application of Anticancer Drugs Enhances Cell Death by Rewiring Apoptotic Signaling Networks. *Cell* **149**, 780-794, doi:http://dx.doi.org/10.1016/j.cell.2012.03.031 (2012).

7 Vander Heiden, M. G. *et al.* Growth factors can influence cell growth and survival through effects on glucose metabolism. *Molecular and cellular biology* **21**, 5899-5912 (2001).

8 Altman, B. J. & Rathmell, J. C. Metabolic stress in autophagy and cell death pathways. *Cold Spring Harb Perspect Biol* **4**, a008763, doi:10.1101/cshperspect.a008763 (2012).

9 Verhaak, R. G. W. *et al.* An integrated genomic analysis identifies clinically relevant subtypes of glioblastoma characterized by abnormalities in PDGFRA, IDH1, EGFR and NF1. *Cancer cell* **17**, 98, doi:10.1016/j.ccr.2009.12.020 (2010).

10 Babic, I. *et al.* EGFR mutation-induced alternative splicing of Max contributes to growth of glycolytic tumors in brain cancer. *Cell Metab* **17**, 1000-1008, doi:10.1016/j.cmet.2013.04.013 (2013).

11 Lee, J. *et al.* Tumor stem cells derived from glioblastomas cultured in bFGF and EGF more closely mirror the phenotype and genotype of primary tumors than do serum-cultured cell lines. *Cancer Cell* **9**, 391-403, doi:S1535-6108(06)00117-6 [pii] 10.1016/j.ccr.2006.03.030 (2006).

12 Nathanson, D. A. *et al.* Targeted therapy resistance mediated by dynamic regulation of extrachromosomal mutant EGFR DNA. *Science* **343**, 72-76, doi:10.1126/science.1241328 (2014).

13 Masui, K. *et al.* mTOR complex 2 controls glycolytic metabolism in glioblastoma through FoxO acetylation and upregulation of c-Myc. *Cell Metab* **18**, 726-739, doi:10.1016/j.cmet.2013.09.013 (2013).

14 Haq, R. *et al.* Oncogenic BRAF regulates oxidative metabolism via PGC1alpha and MITF. *Cancer Cell* **23**, 302-315, doi:10.1016/j.ccr.2013.02.003 (2013).

15 Zhao, Y. *et al.* Glucose metabolism attenuates p53 and Puma-dependent cell death upon growth factor deprivation. *J Biol Chem* **283**, 36344-36353, doi:10.1074/jbc.M803580200 (2008).

16 Deng, J. *et al.* BH3 profiling identifies three distinct classes of apoptotic blocks to predict response to ABT-737 and conventional chemotherapeutic agents. *Cancer Cell* **12**, 171-185, doi:10.1016/j.ccr.2007.07.001 (2007).

17 Montero, J. *et al.* Drug-induced death signaling strategy rapidly predicts cancer response to chemotherapy. *Cell* **160**, 977-989, doi:10.1016/j.cell.2015.01.042 (2015).

18 Kruse, J. P. & Gu, W. Modes of p53 regulation. *Cell* **137**, 609-622, doi:10.1016/j.cell.2009.04.050 (2009).

19 Maddocks, O. D. & Vousden, K. H. Metabolic regulation by p53. *J Mol Med (Berl)* **89**, 237-245, doi:10.1007/s00109-011-0735-5 (2011).

20 Jiang, D. *et al.* Analysis of p53 transactivation domain mutants reveals Acad11 as a metabolic target important for p53 pro-survival function. *Cell reports* **10**, 1096-1109, doi:10.1016/j.celrep.2015.01.043 (2015).

21 Chipuk, J. E. *et al.* Direct activation of Bax by p53 mediates mitochondrial membrane permeabilization and apoptosis. *Science* **303**, 1010-1014, doi:10.1126/science.1092734 (2004).

22 Mihara, M. *et al.* p53 Has a Direct Apoptogenic Role at the Mitochondria. *Molecular Cell* **11**, 577-590, doi:http://dx.doi.org/10.1016/S1097-2765(03)00050-9 (2003).

23 Liu, J. C. *et al.* High mitochondrial priming sensitizes hESCs to DNA-damage-induced apoptosis. *Cell Stem Cell* **13**, 483-491, doi:10.1016/j.stem.2013.07.018 (2013).

24 Strom, E. *et al.* Small-molecule inhibitor of p53 binding to mitochondria protects mice from gamma radiation. *Nat Chem Biol* **2**, 474-479, doi:http://www.nature.com/nchembio/journal/v2/n9/suppinfo/nchembio809_S1.html (2006).

25 Tasdemir, E. *et al.* Regulation of autophagy by cytoplasmic p53. *Nature cell biology* **10**, 676-687, doi:10.1038/ncb1730 (2008).

26 Green, D. R. & Kroemer, G. Cytoplasmic functions of the tumour suppressor p53. *Nature* **458**, 1127-1130, doi:10.1038/nature07986 (2009).

27 Chipuk, J. E., Bouchier-Hayes, L., Kuwana, T., Newmeyer, D. D. & Green, D. R. PUMA couples the nuclear and cytoplasmic proapoptotic function of p53. *Science* **309**, 1732-1735, doi:10.1126/science.1114297 (2005).

28 Lessene, G. *et al.* Structure-guided design of a selective BCL-XL inhibitor. *Nat Chem Biol* **9**, 390-397, doi:10.1038/nchembio.1246

http://www.nature.com/nchembio/journal/v9/n6/abs/nchembio.1246.html#supplementary-information (2013).

29 Comprehensive genomic characterization defines human glioblastoma genes and core pathways. *Nature* **455**, 1061-1068, doi:nature07385 [pii] 10.1038/nature07385 (2008).

30 Zhang, Y., Xiong, Y. & Yarbrough, W. G. ARF Promotes MDM2 Degradation and Stabilizes p53: ARF-INK4a Locus Deletion Impairs Both the Rb and p53 Tumor Suppression Pathways. *Cell* **92**, 725-734, doi:http://dx.doi.org/10.1016/S0092-8674(00)81401-4 (1998).

31 Pomerantz, J. *et al.* The Ink4a tumor suppressor gene product, p19Arf, interacts with MDM2 and neutralizes MDM2's inhibition of p53. *Cell* **92**, 713-723 (1998).

32 Tovar, C. *et al.* Small-molecule MDM2 antagonists reveal aberrant p53 signaling in cancer: implications for therapy. *Proc Natl Acad Sci U S A* **103**, 1888-1893, doi:10.1073/pnas.0507493103 (2006).

33 Lehar, J. *et al.* Synergistic drug combinations tend to improve therapeutically relevant selectivity. *Nat Biotechnol* **27**, 659-666, doi:10.1038/nbt.1549 (2009).

34 Vaseva, A. V., Marchenko, N. D. & Moll, U. The transcription-independent mitochondrial p53 program is a major contributor to Nutlin-induced apoptosis in tumor cells. *Cell Cycle* **8**, 1711-1719, doi:10.4161/cc.8.11.8596 (2009).

35 Chipuk, J. E., Maurer, U., Green, D. R. & Schuler, M. Pharmacologic activation of p53 elicits Bax-dependent apoptosis in the absence of transcription. *Cancer cell* **4**, 371-381, doi:http://dx.doi.org/10.1016/S1535-6108(03)00272-1 (2003).

36 DeBerardinis, R. J., Lum, J. J., Hatzivassiliou, G. & Thompson, C. B. The biology of cancer: metabolic reprogramming fuels cell growth and proliferation. *Cell Metab* **7**, 11-20, doi:S1550-4131(07)00295-1 [pii] 10.1016/j.cmet.2007.10.002 (2008).

37 Ding, Q. *et al.* Discovery of RG7388, a potent and selective p53-MDM2 inhibitor in clinical development. *J Med Chem* **56**, 5979-5983, doi:10.1021/jm400487c (2013).

38 Tannous, B. A. Gaussia luciferase reporter assay for monitoring biological processes in culture and in vivo. *Nat Protoc* **4**, 582-591, doi:nprot.2009.28 [pii] 10.1038/nprot.2009.28 (2009).

39 Qu, L. *et al.* Endoplasmic reticulum stress induces p53 cytoplasmic localization and prevents p53-dependent apoptosis by a pathway involving glycogen synthase kinase-3β. *Genes & Development* **18**, 261-277, doi:10.1101/gad.1165804 (2004).

40 Han, M.-K. *et al.* SIRT1 Regulates Apoptosis and Nanog Expression in Mouse Embryonic Stem Cells by Controlling p53 Subcellular Localization. *Cell Stem Cell* **2**, 241-251, doi:10.1016/j.stem.2008.01.002.

41 Yang, W. H. *et al.* Modification of p53 with O-linked N-acetylglucosamine regulates p53 activity and stability. *Nature cell biology* **8**, 1074-1083, doi:http://www.nature.com/ncb/journal/v8/n10/suppinfo/ncb1470_S1.html (2006).

42 Leu, J. I. J., Dumont, P., Hafey, M., Murphy, M. E. & George, D. L. Mitochondrial p53 activates Bak and causes disruption of a Bak-Mcl1 complex. *Nat Cell Biol* **6**, 443-450 (2004).

43 Follis, A. V. *et al.* PUMA binding induces partial unfolding within BCL-xL to disrupt p53 binding and promote apoptosis. *Nat Chem Biol* **9**, 163-168, doi:http://www.nature.com/nchembio/journal/v9/n3/abs/nchembio.1166.html#supplementary-information (2013).

44 Reardon, D. A., Wen, P. Y. & Mellinghoff, I. K. Targeted molecular therapies against epidermal growth factor receptor: past experiences and challenges. *Neuro Oncol* **16 Suppl 8**, viii7-13, doi:10.1093/neuonc/nou232 (2014).

45 Wei, W. *et al.* Single-Cell Phosphoproteomics Resolves Adaptive Signaling Dynamics and Informs Targeted Combination Therapy in Glioblastoma. *Cancer Cell* **29**, 563-573, doi:10.1016/j.ccell.2016.03.012 (2016).

46 Clark, P. M., Ebiana, V. A., Gosa, L., Cloughesy, T. F. & Nathanson, D. A. Harnessing Preclinical Molecular Imaging to Inform Advances in Personalized Cancer Medicine. *Journal of Nuclear Medicine* **58**, 689-696, doi:10.2967/jnumed.116.181693 (2017).

47 Spence, A. M. *et al.* 18F-FDG PET of Gliomas at Delayed Intervals: Improved Distinction Between Tumor and Normal Gray Matter. *Journal of Nuclear Medicine* **45**, 1653-1659 (2004).

48 Nathanson, D. A. *et al.* Co-targeting of convergent nucleotide biosynthetic pathways for leukemia eradication. *The Journal of experimental medicine* **211**, 473-486, doi:10.1084/jem.20131738 (2014).

49 Takanaga, H. & Frommer, W. B. Facilitative plasma membrane transporters function during ER transit. *FASEB J* **24**, 2849-2858, doi:10.1096/fj.09-146472 (2010).

50 Cheng, E. H. *et al.* BCL-2, BCL-X(L) sequester BH3 domain-only molecules preventing BAX- and BAK-mediated mitochondrial apoptosis. *Molecular cell* **8**, 705-711 (2001).

51 Dai, H., Marbach, P., Lemaire, M., Hayes, M. & Elmquist, W. F. Distribution of STI-571 to the Brain Is Limited by P-Glycoprotein-Mediated Efflux. *Journal of Pharmacology and Experimental Therapeutics* **304**, 1085-1092, doi:10.1124/jpet.102.045260 (2003).

52 Gao, J. *et al.* Integrative analysis of complex cancer genomics and clinical profiles using the cBioPortal. *Sci Signal* **6**, pl1, doi:10.1126/scisignal.2004088 (2013).

53 Cerami, E. *et al.* The cBio cancer genomics portal: an open platform for exploring multidimensional cancer genomics data. *Cancer discovery* **2**, 401-404, doi:10.1158/2159-8290.CD-12-0095 (2012).

CHAPTER 3:

Concluding Remarks: Redefining Precision Medicine

The advent of targeted agents – the beginning of precision medicine – bolstered the potential of future cancer therapy. The success rates of Imatinib in leukemic patients held promises of near-future cures for cancer patients[1,2]. Patients with the genetic fusion of BCR-ABL could simply ingest a pill that would prolong their lives drastically. Shortly after the discovery of Imatinib, the world witnessed the developmental blitz of precision medicine. Following in pursuit was the implementation of Vemurafenib for melanoma patients with the BRAF V600E mutation, the utilization of Trastuzumab for HER2-positive breast cancer, and the employment of Gefitinib for non-small-cell lung cancer patients with mutations in EGFR[3-5]. All of these discoveries made significant advancements on conventional cancer therapies, further adding to the prospect of a cancer cure in the foreseeable future.

However, almost two decades after the approval of Imatinib, the field of precision medicine remains somewhat at a standstill. That is not to say there has not been progress since as there has been many slight improvements with combinatorial treatments and tweaks in second and third generation inhibitors. For instance, the addition of a MEK inhibitor with Vemurafenib extended median progression free survival by approximately 4 months in melanoma[6]. In addition, the discovery of AZD9291 was able to combat non-small-cell lung cancer that had become resistant to traditional EGFR inhibitors, leading to a progression-free survival of 9.6 months[7]. Nevertheless, these small victories have not met the expectations the field had set for itself nearly twenty years ago when 89% of patients reached a 5 year survival in response to very first targeted therapy[1].

So why are we so distant from our expectations? Why are we not able to do more with the arsenal of targeted therapies we have at our disposal? Why do some cancers have such dim prognoses, where the majority of patients never reach the 5 year survival mark (e.g. colorectal, glioblastoma, esophageal, liver, pancreatic)[8]? The short answer to this is: we *don't* know. We do not understand

why some cancers with the similar genetic lesions have differential responses to the same treatment.

The field has taken strides in understanding these discrepancies. The central dogma of DNA to protein and therefore function, provided a starting point into understanding cancer drivers. With the rapid advancement of sequencing technology, and the extensive molecular characterizations by the TCGA across multiple cancers, many believed that we would be able to identify all actionable targets in cancers and pinpoint how to best treat them. In some instances this was the case. Such was the identification of chromosomal rearrangements of anaplastic lymphoma kinase (ALK) in a small subset of non–small cell lung cancer (NSCLC) patients, which led to the development of extremely successful ALK inhibitors[9,10].

However, on the other end, genetic alterations seldom correlated with response. For instance, colorectal cancers with BRAF V600E mutations demonstrated about a 5% response rate with Vemurafinib[11], whereas approximately 50% of melanoma patients with the same genetic alteration responded to the monotherapy. Furthermore, glioblastoma, which is predominantly characterized as harboring EGFR amplifications/ mutations, has not experienced any clinical benefit with anti-EGFR therapies, whereas EGFR inhibitors have significantly improved lung cancer prognosis[5,12]. These data may suggest that cancers show differential dependencies to these oncogenic signals. Whereas in cases such as BRC-ABL leukemia, BRAF V600E melanoma, and EGFR altered lung cancers, where the defined oncogene is crucial for survival, in other cancers they may be, in a sense, dispensable.

It is possible that we have yet to identify true genetic drivers of cancer and that further studies are necessary in order to elucidate the best actionable targets for each cancer. However, the concept of non-oncogene drivers (or non-oncogene addiction) is not new[13]. Cancers such as diffuse intrinsic pontine gliomas (DIPG) have been genetically dissected and few profound oncogenic mutations have been discovered; rather the majority of DIPG samples displayed epigenetic

aberrations[14]. This then begs the question: how do we define drivers of cancer? Perhaps in the future, genetic and molecular profiling will advance to a point where DNA equals function. But as of now, when genetic markers are insufficient to inform us of such information, we must consider other approaches that can help us identify the true functional drivers of cancer.

There are many avenues that can lead to a therapeutic response. In particular, a number of hallmarks of cancer have been highlighted (e.g. oncogenic signaling, altered metabolism, immune evasion, ER stress response, resistance to apoptosis, angiogenesis, etc.)[15]. However, inhibition of which function will most likely lead to a clinical response? There appears to be a fixed paradigm for therapeutic strategies where various FDA approved compounds are combined with little mechanistic reasoning besides the fact that they have shown clinical promise in another malignancy. As we highlighted in Chapter 1, although this may be effective in the short-term, it seldom leads to prolonged responses in patients. That is not to be dismissive of this approach, as it serves to expedite new, impactful therapies. However, as we begin to reach the asymptote of clinical advancement with this style of precision medicine, we must take a step back and reexamine our approach.

A first step is to begin assuming that each cancer is unique, and consequently, so are their dependencies on particular functions. Looking back at oncogenic signaling functions in colorectal cancer, a recent clinical trial attempted to completely ablate MAP kinase signaling by combining BRAF, MEK, and EGFR inhibitors. This resulted in a response rate of 20%[16], which is a vast advancement from the initial 5% response with BRAF inhibitor alone, but stands in stark contrast when compared to the 50% response rate with single agent BRAF inhibitor in melanoma, reiterating that oncogenic signaling may not be the most prevalent function to be targeting in this cancer. In another example, Yuneva *et. al.* demonstrated that metabolic reprogramming in cancers, which many assume to be a universal phenomenon that occurs during tumorigenesis, can vary even within the same cancer[17]. In this study, they demonstrate that MYC-driven liver

tumors enhanced their glutamine catabolism as opposed to MET-driven liver tumors[17]. Therefore, inhibition of this metabolic function had a therapeutic effect in only the MYC-driven tumors. As a consequence of these variations, even within the same tumor type, it is crucial that we are able to identify what functions each cancer is most reliant upon when considering a therapeutic strategy.

Due to the rapid evolutionary traits of cancer, the optimal response will most likely require inhibition of multiple critical functions. As such, it is imperative that we are able to detect these functionalities and characterize which drugs can act on these events. As of now, therapies are often judged using the gold standard of growth inhibition. In the clinical setting, this may be suitable, however, in the academic setting, where discoveries are occurring, we must break from that mold, especially if targeting multiple modalities of cancer are necessary for clinical response.

As we begin to further understand cancer and their dependencies, we must also deepen our understanding of the agents we have at our disposal. If metabolism is critical, we must have agents that specifically alter those pathways; if immune evasion is the key component for tumor survival, then we must have therapies well established in that aspect; and so forth. We must be more specific in our approach and have well-characterized therapies, rather than placing them under the umbrella group of “growth inhibitory”.

In the Chapter 2 of this work, we provide a glimpse of such approach. Here, we identify two complimentary functions (metabolism and apoptosis) that are delicately interconnected and vital for glioblastoma survival. By disrupting each component individually, we are not able to achieve any therapeutic effect. However, by first disturbing the metabolic function, we are able to create a vulnerability in the apoptotic machinery that we can then exploit. Furthermore, we were able to measure disruptions in each of the functionalities, allowing us to determine which therapies would be most effective.

Although cancer therapy is not quite what many envisioned some twenty years ago, the field is still moving forward. With a stronger fundamental basis of cancer biology, as well as technological advancements, we are beginning to unravel the complexities of cancer. The notion that cancers could be treated with single therapies is now often disregarded. We must take what we learned from past setbacks to continue redefining our approach. With greater insight into the functionalities of cancer, and with the development of promising new therapies that can disrupt these functions, such as BH3 mimetics and immunotherapy, precision medicine has been reinvigorated.

REFERENCES

1 Druker, B. J. *et al.* Five-Year Follow-up of Patients Receiving Imatinib for Chronic Myeloid Leukemia. *New England Journal of Medicine* **355**, 2408-2417, doi:10.1056/NEJMoa062867 (2006).

2 Druker, B. J. *et al.* Activity of a Specific Inhibitor of the BCR-ABL Tyrosine Kinase in the Blast Crisis of Chronic Myeloid Leukemia and Acute Lymphoblastic Leukemia with the Philadelphia Chromosome. *New England Journal of Medicine* **344**, 1038-1042, doi:10.1056/NEJM200104053441402 (2001).

3 Chapman, P. B. *et al.* Improved Survival with Vemurafenib in Melanoma with BRAF V600E Mutation. *New England Journal of Medicine* **364**, 2507-2516, doi:10.1056/NEJMoa1103782 (2011).

4 Piccart-Gebhart, M. J. *et al.* Trastuzumab after Adjuvant Chemotherapy in HER2-Positive Breast Cancer. *New England Journal of Medicine* **353**, 1659-1672, doi:10.1056/NEJMoa052306 (2005).

5 Maemondo, M. *et al.* Gefitinib or Chemotherapy for Non–Small-Cell Lung Cancer with Mutated EGFR. *New England Journal of Medicine* **362**, 2380-2388, doi:10.1056/NEJMoa0909530 (2010).

6 Larkin, J. *et al.* Combined Vemurafenib and Cobimetinib in BRAF-Mutated Melanoma. *New England Journal of Medicine* **371**, 1867-1876, doi:10.1056/NEJMoa1408868 (2014).

7 Jänne, P. A. *et al.* AZD9291 in EGFR Inhibitor–Resistant Non–Small-Cell Lung Cancer. *New England Journal of Medicine* **372**, 1689-1699, doi:10.1056/NEJMoa1411817 (2015).

8 Siegel Rebecca, L., Miller Kimberly, D. & Jemal, A. Cancer statistics, 2018. *CA: A Cancer Journal for Clinicians* **68**, 7-30, doi:10.3322/caac.21442 (2018).

9 Kwak, E. L. *et al.* Anaplastic Lymphoma Kinase Inhibition in Non–Small-Cell Lung Cancer. *The New England journal of medicine* **363**, 1693-1703, doi:10.1056/NEJMoa1006448 (2010).

10 Awad, M. M. & Shaw, A. T. ALK Inhibitors in Non–Small Cell Lung Cancer: Crizotinib and Beyond. *Clinical advances in hematology & oncology : H&O* **12**, 429-439 (2014).

11 Kopetz, S. *et al.* Phase II Pilot Study of Vemurafenib in Patients With Metastatic BRAF-Mutated Colorectal Cancer. *Journal of Clinical Oncology* **33**, 4032-4038, doi:10.1200/JCO.2015.63.2497 (2015).

12 Westphal, M., Maire, C. L. & Lamszus, K. EGFR as a Target for Glioblastoma Treatment: An Unfulfilled Promise. *CNS Drugs* **31**, 723-735, doi:10.1007/s40263-017-0456-6 (2017).

13 Luo, J., Solimini, N. L. & Elledge, S. J. Principles of cancer therapy: oncogene and non-oncogene addiction. *Cell* **136**, 823-837, doi:10.1016/j.cell.2009.02.024 (2009).

14 Hashizume, R. Epigenetic Targeted Therapy for Diffuse Intrinsic Pontine Glioma. *Neurologia medico-chirurgica* **57**, 331-342, doi:10.2176/nmc.ra.2017-0018 (2017).

15 Hanahan, D. & Weinberg, Robert A. Hallmarks of Cancer: The Next Generation. *Cell* **144**, 646-674, doi:10.1016/j.cell.2011.02.013.

16 Corcoran, R. B. *et al.* Combined BRAF, EGFR, and MEK Inhibition in Patients with BRAF^{V600E}-Mutant Colorectal Cancer. *Cancer Discovery* **8**, 428 (2018).

17 Yuneva, M. O. *et al.* The Metabolic Profile of Tumors Depends on both the Responsible Genetic Lesion and Tissue Type. *Cell Metabolism* **15**, 157-170, doi:10.1016/j.cmet.2011.12.015 (2012).